Limitations of Superfluid Helium Droplets as Host System Revealed by Electronic Spectroscopy of Embedded Molecules

Dissertation

zur Erlangung des Doktorgrades
der Naturwissenschaften (Dr. rer. nat.) an der
Fakultät für Chemie und Pharmazie
der Universität Regensburg

vorgelegt von

Tobias Premke

aus Passau

Regensburg, den 21. Dezember 2015

Diese Arbeit wurde angeleitet von: Prof. Dr. Alkwin Slenczka
Promotionsgesuch eingereicht am: 21.12.2015
Tag der mündlichen Prüfung: 19.02.2016

Prüfungsausschuss: PD Dr. Rainer Müller (Vorsitzender)
Prof. Dr. Alkwin Slenczka
Prof. Dr. Bernhard Dick
Prof. Dr. Alfons Penzkofer

Contents

1 Introduction 1

2 Basic Principles 5

2.1 Physical Properties of Superfluid Helium . . . 5

2.2 Superfluid Helium Nano Droplets . . . 9

2.2.1 Generation of Superfluid Helium Droplets . . . 15

2.2.2 Doping - Pick-up Process . . . 22

2.3 Electronic Spectroscopy inside Helium Droplets . . . 26

2.3.1 Laser-Induced Fluorescence Spectroscopy . . . 26

2.3.2 Zero Phonon Line . . . 28

2.3.3 Phonon Wing . . . 30

2.4 Emission Spectroscopy inside Superfluid Helium Droplets . . . 32

3 Experimental Setup and Methods 35

3.1 Construction of the Helium Droplet Apparatus . . . 35

3.1.1 Continuous Flow Helium Droplet Beam . . . 35

3.1.2 Pulsed Helium Droplet Beam . . . 40

3.2 Laser Setup and Detection Unit / Continuous Wave (cw) . . . 42

3.2.1 cw Laser Setup . . . 42

3.2.2 LIF and Dispersed Emission . . . 43

3.2.3 Bolometer Unit . . . 45

3.2.4 Quadrupol Mass Spectrometer . . . 51

3.3 Methods of Detection 51
3.3.1 Laser-Induced Fluorescence LIF 51
3.3.2 Dispersed Emission 52
3.3.3 Depletion Technique 53
3.3.4 Stoichiometric Analysis 55
3.3.5 Quadrupole Mass Spectrometer 57

4 Phthalocyanine 59
4.1 Introduction 59
4.2 Experimental Results 60
4.2.1 Laser-Induced Fluorescence / ZPL and PW 60
4.2.2 Saturation Behavior of Pc 64
4.2.3 Dependence of ZPL and PW on the Mean Droplet Size 72
4.2.4 Dispersed Emission 77
4.2.5 Van der Waals Complexes of Phthalocyanine Argon 83
4.2.6 Off-resonant Excitation of Phthalocyanine 88
4.2.7 Low Frequent Vibronic Excitation 103
4.3 Conclusions 106

5 Depletion Spectroscopy 110
5.1 Introduction 110
5.2 Experimental Details 111
5.2.1 Bolometer - Basic Experiments 111
5.2.2 Pentacene 116
5.3 LIF and Depletion 118

6 Iodine in Superfluid Helium Droplets 120
6.1 Motivation 120
6.2 Introduction 121
6.2.1 Spectroscopic Properties of Iodine 122

6.3 Experimental Details 128
6.3.1 Pick-up Conditions 128
6.3.2 Mean Size of Helium Droplets / Depletion 141
6.4 Results 143

7 Discussion 146

Bibliography 151

1 Introduction

The first spectroscopic measurements of molecules embedded in helium droplets were reported in the early 1990s [1, 2]. These first experiments on SF_6 assumed that the superfluid helium droplets were a uniquely cold nanomatrix for molecules and molecular complexes, combining the benefits of solid matrices as well as of the gas phase and avoiding some of the disadvantages of both techniques at the same time. By the usage of helium droplets it was possible to prepare very cold and isolated molecules inside a liquid "matrix" with negligible viscosity. This led to a considerable scientific interest and the technique became a serious alternative to the well-known methods of isolated atoms in the gas phase or in solid matrices. Thus, the helium droplets became a frequently used cryogenic host system for numerous spectroscopic experiments on the behavior of different atoms, ions, neutral molecules, radicals, clusters as well as reactions in helium [3–10]. Since the first measurements of SF_6 in helium droplets the upcoming experimental observations have shown evidence for the superfluidity of helium droplets. Many of these experiments on molecular spectroscopy within the frequency range from microwave up to the UV region have demonstrated the unique properties of helium droplets as cryogenic host at 0.37 K. Beside various experimental examinations, theoretical simulations have also been published describing the properties and the behavior of the droplets as well as the interactions between helium and the dopant species [11–16].

Despite the superfluidity of the helium droplets and their vanishing viscosity, there are weak interactions between helium and the dopant species. These interactions can cause characteristic spectral features. Such microsolvation effects of superfluid helium can be studied by means of high resolution spectroscopy and, if available, in comparison to corresponding experimental data from the gas phase. The experimentally observed, helium-induced features can be found in the form of multiplet splitting of molecular transitions [17], solvent shifts of electronic transition frequencies (zero phonon line ZPL), increased moment of inertia and phonon wings (PW) [4]. On the basis of the variety of experiments a model was set up which postulates a non-superfluid helium solvation layer around the dopant. By means of this helium dopant solvation complex the experimental observations could be explained only empirically. Pure molecular signals (ZPL) in electronic spectra are accompanied by the phonon wing (PW) which is attributed to the spectroscopic signature of the superfluid helium droplet. Additionally, the PW can also include the spectroscopic signature of the non-superfluid solvation layer around the dopant such as van der Waals modes of the solvation complex. Despite numerous experimental results as well as theoretical improvements, a general quantitative explanation of the helium-induced spectral effects has not been found so far.

Since the quantitative understanding of helium-induced spectral features is essential to interpret molecular spectra recorded in helium droplets, further experiments are needed. The aim of this study is to contribute further experimental details on microsolvation in superfluid helium droplets by means of high resolution electronic spectroscopy of molecules in helium droplets. Beside a detailed examination of the ZPL as well as of the PW of phthalocyanine (Pc) by means of fluorescence excitation and dispersed emission spectroscopy, the microsolvation of helium droplets will be examined over a wide range of the mean droplet size from 10^3 up to 10^7 atoms. For this purpose two major aspects shall receive attention; the chromophore shall be of simple molecular structure and it has to be chosen in a manner that the mean droplet size can be manipulated from small up to huge helium droplets. In this regard, iodine was selected for the purpose of this study. Its structure possibly avoids the presence of numerous variants of the solvation complex, its detailed spectroscopic data in the gas phase is very well documented to a high standard in the literature [18–20] and theoreticians have provided a high level helium to iodine interaction potential [21]. Moreover, it allows for a rotational resolution of electronic transitions, which is directly related to the moment of inertia and, thus, information about the solvation complex can be extracted from experiments. Finally, this study might be extended by a similar examination of the polar ICl molecule in helium droplets.

The electronic excitation of iodine is accompanied with a significant increase of the equilibrium distance in the excited state. This leads to a broad Franck-Condon distribution and the electronic excitation as well as the radiative decay of iodine end in higher vibrational levels of iodine. These vibrational modes can couple to the helium droplets and the energy dissipates. This leads to a decrease of the mean size of the doped helium droplets. Thus, only a small amount of the absorbed energy decays radiatively and the emission of iodine is shifted to infrared radiation in a frequency range between 745 nm and 762 nm ($\lambda_{\text{gas phase}} \approx 640$ nm). By this process one can profit by the sensitivity of the depletion spectroscopy using a bolometer. For this purpose a commercial bolometer had to be implemented to the experimental setup.

By the analysis of iodine and phthalocyanine two contrary systems are selected. Electronic transitions in both molecules are accessible by the cw dye ring laser system. Phthalocyanine is a planar organic molecule offering a huge and planar surface to the helium atoms and thus, the non-superfluid helium solvation layer can form different structures. In contrast, the diatomic iodine is of simple molecular shape. That means that different complex structures of the non-superfluid helium solvation layer and the dopant can be expected to be avoided. Moreover, the dopant to helium interaction of I_2 should differ significantly from Pc due to a different polarizability of the molecules and the higher electronegativity of iodine compared to carbon. Thus, both molecules should show clear differences in their microsolvation behavior which can be examined by means of electronic spectroscopy. These experiments might end in a comparison of effects due to the non-superfluid helium and the superfluid helium droplets and shall provide a better understanding of the microsolvation in helium droplets.

The work is structured as follows. First, the most important features of superfluid helium and the helium droplets will be summarized. The second chapter describes briefly the experimental setup followed by a description of the measurement techniques. Afterwards, it will be shown that the operation of the bolometer could be tested and verified by excitation measurements of pentacene in helium droplets. Then, the next two chapters include the spectroscopic examination of phthalocyanine and iodine inside superfluid helium droplets. In the end the results are summarized and discussed and a conclusion on the microsolvation in superfluid helium nano droplets is given.

2 Basic Principles

In the first part of this chapter the most important features of superfluid helium will be summarized. Afterwards it will be shown how the invention of different techniques of low temperature spectroscopy in the 20^{th} century opened up a wide field of interdisciplinary research and led to the development of the superfluid helium droplet beam method. After that the main principles of the generation and the handling of this unique method will be discussed. Finally, the description of the special spectroscopic properties of superfluid helium droplets will be presented. This includes its benefits as well as its disadvantages compared to other techniques.

2.1 Physical Properties of Superfluid Helium

Helium is the only known element which remains liquid down to the absolute zero point at standard conditions for pressure. The reason for this phenomenon can be found in a weak polarizibility (α = 0.21 Å^3 [8]), low mass and a high zero point energy of helium [22]. The helium appears in two isotopic variants, namely the dominating bosonic species ^{4}He and a minor fermionic component ^{3}He (0.000137 %). Since all experiments in this work were performed inside ^{4}He droplets, the term "helium" shall refer from now to the bosonic helium isotope and only some phenomena of ^{3}He will be mentioned. At normal pressure the gas to liquid phase transition occurs at 4.21 K for ^{4}He (3.19 K for ^{3}He). A second phase transition indicated by discontinuities of physical quantities such as viscosity [23, 24] ($\eta = 4 \cdot 10^{-9}$ C.G.S. units[1] [25, 26]), heat capacity [27], heat conductivity and speed of sound [22] is observed under normal pressure at 2.17 K for ^{4}He (2.6 mK for ^{3}He) whereby the systems stays liquid. Additionally, a fountain effect [28] as well as the Onnes effect [29] (Rollin-film [22, 30, 31]) can be observed, and quantized vortices can be found [22, 32, 33] in liquid helium below 2.17 K. The change of the physical properties at this so-called lambda point (T_λ = 2.17 K at 1 bar) marks the phase transition between He I and He II. Above T_λ helium is called He I and can be treated like a normal liquid whereas below T_λ helium is called He II. This state has to be described as a quantum fluid and its phenomena are dominated by quantum effects. The low polarizibility of the helium atom leads to attractive, very weak van der Waals forces between the helium atoms manifested in a helium-helium potential with a potential well of only 11.0 K at an equilibrium distance of 2.97 Å. Equation 2.1 allows the calculation of the thermal de Broglie wavelength:

$$\Lambda = \frac{\mathrm{h}}{\sqrt{2\pi \mathrm{m} \mathrm{k_B} \mathrm{T}}} \tag{2.1}$$

In this equation h is the Planck constant ($6.62606957(29) \cdot 10^{-34}$ Js), k_B the Boltzmann constant ($1.38064852(79) \cdot 10^{-23}$ J/K), m the mass of helium (4.002602(2) amu[2]) and T the temperature. At T_λ a value of $\Lambda = 5.923849$ Å can be calculated, which exceeds the equilibrium distance in the interaction potential by a factor of 2. In this situation the wave nature of the atoms has to be taken into account and therefore the helium is defined as a quantum fluid. The system condenses in a single global state which describes the entire ensemble of the helium atoms. A macroscopic amount of helium below 2.17 K can be described by one global quantum state which can be written, equal to the Bose-Einstein condensation, as a single many-body wave function and the absolute square of this function is a measure of the number of helium atoms. The analogy to the Bose-Einstein condensation was already suggested

---

[1] The centimeter–gram–second system of units; kinematic viscosity in $\frac{cm^2}{s}$.

[2] Atomar mass units, 1 amu = $1.660538782 \cdot 10^{-27}$ kg

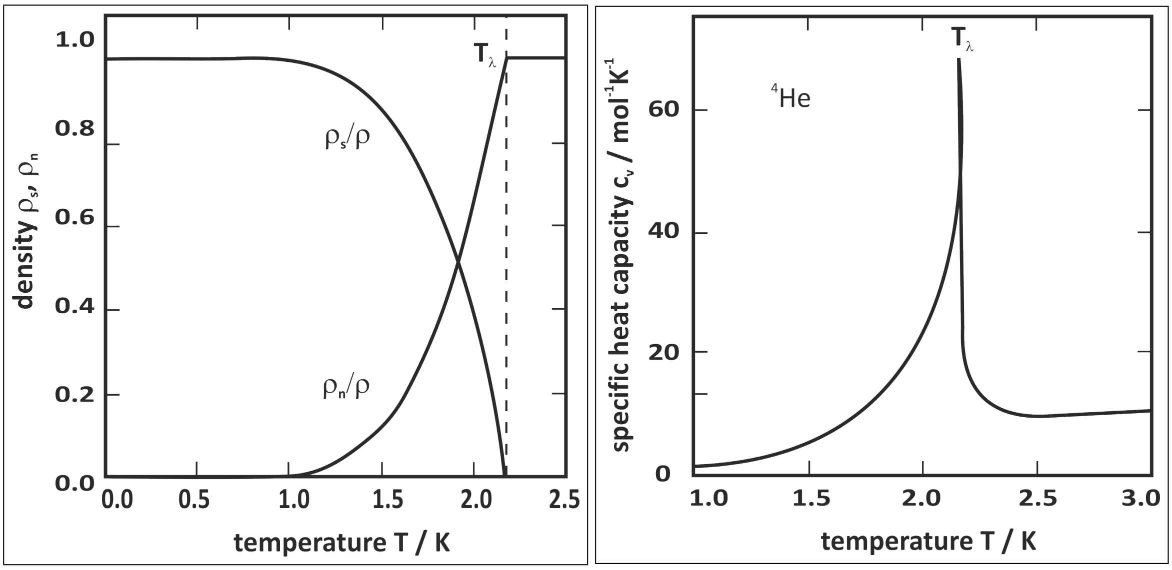

Fig. 2.1: Plot of the ratio of normal fluid and superfluid helium in He II below T_λ (left side) and the specific heat capacity c_V of ^{4}He between 1 K ≤ T ≤ 3 K (right side), both taken from [22].

in 1983 [34]. The energy of the He_2 binding state is found to be close to its dissociation limit and the state is delocalized far beyond the helium-helium distance of the dimer. For the delocalization an expected value of the He-He distance of 52 ± 4 Å could be experimentally determined [35]. The unusual macroscopic phenomena can be described by the Two Fluid Model treating the thermodynamic and hydrodynamic properties of liquid helium, which was suggested by László Tisza in 1938 [36, 37]. The idea of this theory is that He II is a temperature-dependent mixture of two liquids. Thus, He II consists of normal fluid and superfluid He (as shown in Fig. 2.1 left panel). It can be seen that with decreasing temperature the fraction of normal fluid decreases while the superfluid fraction increases. This process starts at 2.17 K and is finished with 100 % superfluid ^{4}He at about 1 K. This system remains fluid down to the absolute zero point of temperature for pressures below 25 bar. The vertical dashed line marks the transition temperature T_λ (at 1 bar). The transition point is called Lambda point which reflects the shape of the the curve progression of the heat capacity c_V (cf. right panel of Fig. 2.1) which

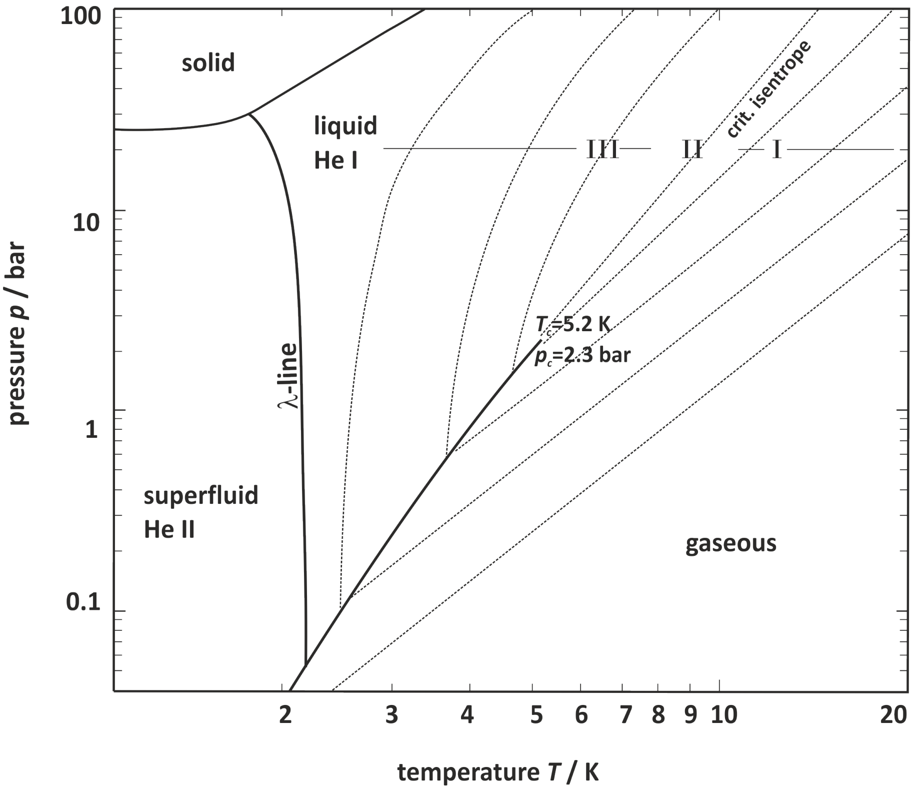

Fig. 2.2: Double logarithmic pressure-temperature phase diagram for ^{4}He according to Buchenau et al. [38]: the bold lines mark phase transitions, the dotted lines show some isentropes for a helium expansion into a vacuum starting at different expansion conditions p_0 and T_0.

reminds of the Greek character lambda. The Two Fluid Model cannot explain the behavior of helium at temperatures near the absolute zero point, it only describes the macroscopic behavior below the Lambda point. The borderline which marks the transformation of the liquid helium in the phase diagram (see figure 2.2) is called λ-line. Below a pressure of 25 bar it is not possible to transform helium into its solid phase [22] by cooling. This unique property allows to keep helium down to temperatures close to the absolute zero point in its liquid form and determines the horizontally boundary curve between the liquid and the solid state in the p-T-phase diagram. A consequence of this missing solid state below a pressure of 25 bar is the

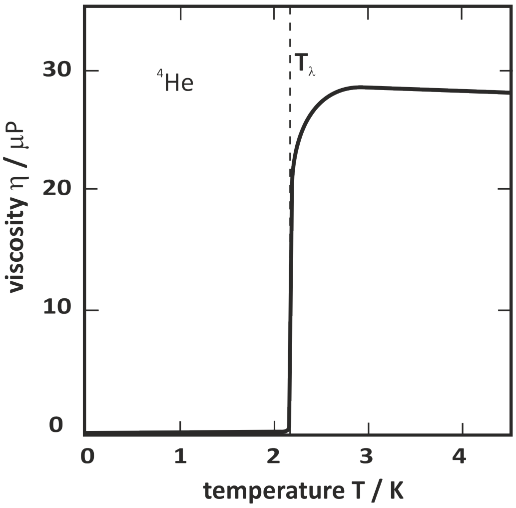

Fig. 2.3: Viscosity of ^{4}He [22].

lack of a triple point in the phase diagram of helium, a point where the three classical phases, namely liquid, solid and gas, are in equilibrium. The superfluid state of helium exhibits some more special physical properties. Figure 2.3 shows the viscosity of liquid helium as a function of temperature near the absolute zero point [22]. At temperatures below T_λ = 2.17 K, the transformation from the normal phase to the superfluid one starts and the viscosity of the liquid vanishes abruptly. Vanishing viscosity means no energy exchange between superfluid helium and within the helium. This feature is warranted as long as the relative velocity is below the Landau velocity. This critical velocity is named after Lew D. Landau [22] and its value is defined as $v_{Landau} = 58\ \frac{\mathrm{m}}{\mathrm{s}}$ ([22, 39]). Below this speed limit He II cannot accept energy via inelastic collisions. Hence, any substance can move frictionless in this quantum fluid as long as its velocity is below the Landau speed. Another extraordinary feature of the superfluid state is its thermal conductivity, which exceeds that of copper by a factor of 30. Combined with the very low temperature of this quantum fluid it constitutes a highly efficient cryo cooler for a large variety of experiments performed at a molecular level. In addition, helium is transparent in a wide range of electromagnetic radiation from the ultraviolet up to the infrared where its refraction index is almost n= 1. 40 years after the discovery of the superfluid phase of ^{4}He Kapitza was awarded the Nobel Prize in 1978.

2.2 Superfluid Helium Nano Droplets

In 1911 Dunnoyer was able to produce the first atomic beam and he showed that atoms can move along a straight line in a vaccum [40]. With these experiments

he laid down the foundations for one of the most important research methods of physics and chemistry in the 20^{th} century. One of the first experiments was the Stern-Gerlach experiment [41]. The technique was further developed and improved and is now used as a powerful method which allows the examination of isolated cold molecules. With this technique it was possible to analyze e.g. isolated molecules, and any kind of intermolecular interaction under single collision conditions.
The beam is generated by an expansion of atoms or molecules under high pressure through an orifice into the vaccum. The pressure has to be set in such a way that the mean free path $\bar{\lambda}$ of the particles is smaller than the diameter d of the orifice which leads to many collisions between the particles and thus, their thermic energy is cooled by this adiabatic expansion (Joule–Thomson effect [42]). Both, velocity and temperature of the beam are dependent on stagnation pressure and the temperature of the nozzle [43]. In case a sample cannot be provided at high pressure, the so-called seeded beam technique can be applied by mixing the sample as minority component to a carrier gas at high pressure. Beside efficient cooling, this technique allows to tune the velocity of the sample to that of the majority component which is large for light particles and small for heavy particles. The cooling efficiency in a molecular beam is dependent on the density of the quantum states within the sample. Thus, the vibrational degree of freedom cannot be cooled as efficiently as the rotational or translation[3] degree of freedom. This leads to very complex spectral data that is difficult to interpret, since hot bands[4] can be observed. Nevertheless, there is no doubt that particle beams are still of high value for fundamental research [44–46] as well as technical applications such as molecular beam epitaxy [47–49].

Another widely used method for the investigation of cold samples is the matrix isolation spectroscopy. This technique was first described by E. Whittle, D.A. Dows und G.C. Pimentel [50] in 1954 and became a standard method in physics and

---

[3] Translation is relative to the molecular beam.

[4] Transitions from higher vibronic states v ≥ 1

chemistry to analyze atoms, molecules, ions as well as reactive intermediates at low temperatures (10 - 20 K). For this purpose the probe molecules are highly diluted (only 0.1 % or less) into an inert gas such as noble gas, nitrogen or other inert species similar in shape to the probe molecule. This mixture condensates on a transparent cold substrate in order to generate a crystal doped with molecules isolated from each other. In this environment the substrate is trapped and stabilized inside a crystal cage, which means that the rotation of the sample is frozen, diffusion is suppressed and reaction kinetics is dramatically lowered [51] - by way of that even highly reactive or metastable species can be analyzed. However, this host system may modify physical and chemical properties of the guest species. The perturbative influence can be minimized by an appropriate choice of the matrix substance. Another disadvantage of matrix isolation spectroscopy is the large variety of the structure of the solid matrix around the dopant species which are addressed as sites. Each of these sites exhibits its own shift of spectroscopic transitions of the dopant species which results in severe line broadening. As a consequence, the vibrational fine structure remains hidden and a reasonable analysis of the dopant species requires sophisticated spectroscopic techniques to discriminate against this inhomogeneous line broadening.
Moreover, it is almost impossible to observe bimolecular reactions inside solid matrices. Thus, the bimolecular chemistry is generally not accessible and only unimolecular processes are observable by means of matrix isolation spectroscopy. Finally, noble gas matrices are notoriously poor heat sinks because only very low energy lattice phonons are available to accept molecular vibrational quanta and hence, thermalization is very slow compared to solution [52]. Nevertheless, by means of appropriate spectroscopic techniques even a homogeneous line width of individual vibronic transitions can be observed [53, 54] (line width of only 0.99 cm^{-1}).

In general, both techniques have different advantages and disadvantages. By the usage of helium as matrix material in combination with the supersonic jet technique the advantages of both methods could be combined by avoiding simultaneously most of the drawbacks. In 1992 the first paper on molecular spectroscopy in combination with a helium cluster beam was reported. However, the laser system, which was a line tunable CO/NO gas laser, did not allow to record a reasonable spectrum. This led to severe misinterpretations of the spectroscopic data [1]. Three years later another group in Göttingen succeeded to record the same spectrum with a continuously tunable diode laser. The IR spectrum of SF_6 revealed rotational resolution [2]. The intensity of the rotational fine structure revealed a temperature of only 0.37(1) K which is far below the lambda point of bosonic helium. This experiment marks the beginning of the molecule spectroscopy combined with the helium droplet beam technique, which provides a lot of benefits. The resolved rotational fine structure with rather sharp resonances revealed two important pieces of information. First, the dopant resides inside the droplet and not on the surface. Secondly, the host system exhibits negligible viscosity and, therefore, is possibly superfluid as it can be expected from the temperature. That allows to observe even rotationally resolved spectra which were only known from the gas phase experiment. Another remarkable physical aspect of the droplets is their thermal behavior. The highly efficient thermal conductivity in combination with evaporative cooling serves for cooling times as short as 10 ns [55] within the droplet beam. Similarly efficient is the thermalization of hot dopant species after the pick-up. The internal and kinetic energy of the dopant dissipates into the helium droplet and is released by evaporation of helium atoms from the droplet surface within ns time scale [2]. Such an energy can be the internal energy of a dopant or the excess energy after electronic excitation of a dopant inside the droplets and even energy released by a molecular reaction inside the droplets. Thus, single molecular species as well as molecular complexes generated by multiple particle doping followed by condensation inside the helium droplet are thermalized to 0.37 K with all degrees of freedom. With respect to the final temperature helium droplets as a host system exceed the supersonic jet technique. A further aspect of the droplets is the possibility to control the stoichiometric composition of molecular complexes generated inside the droplets. As described in chapter 2.2.2, the pick-up process obeys Poisson statistics which allows for a non-destructive analysis of the number of dopant particles of the complex being responsible for an individual signal in an IR or UV/VIS spectrum. By the usage of more than one pick-up unit, different particles can be doped selectively in a given order into the helium droplets, and, thereby, not only the stoichiometry is controlled but in addition the cluster configuration can be influenced. Single atoms, molecules, ions or radicals can be examined as well as weakly bound van der Waals clusters and many metastable complex configurations which are not accessible in the gas phase. Moreover, electron or proton transfer pathways can be analyzed and even chemical reactions can be studied inside the helium droplets. One of the first chemical reactions prepared in helium droplets was the redox reaction of nitrous oxide and barium [56]. Since the vibrational energy of the hot BaO* product molecule dissipates efficiently, the dispersed emission of the electronically excited BaO revealed a very sharp vibrational progression of the electronic ground state. Finally, the helium droplets are optically transparent over a wide range from ultraviolet up to the infrared light. Due to all these unique properties, superfluid helium droplets are an ideal host system with an exceptional cryogenic capability for spectroscopic investigations of cold molecular systems. Since the particle density of the helium droplet beam is considerably smaller than that of a supersonic jet, highly intensive light sources (e.g. lasers, FEL, synchrotron radiation) are used for such examinations. In some cases this can cause saturation of individual transitions leading to line broadening. Such dominant saturation line broadening can be avoided by the attenuation of the intensity of the laser beam to reach high spectral resolution.

Spectroscopy of molecules in superfluid helium droplets has two different aspects. On the one hand, atoms, molecules, ions, radicals, clusters or van der Waals complexes are investigated spectroscopically at very low temperatures. On the other hand, the spectroscopic data of a dopant species is examined in order to extract information about the helium environment or, more precisely, about microsolvation in superfluid helium. These experiments help to understand different effects (cf.

chapter 2.3) occurring inside the helium droplets. In both cases it is often useful to compare the results with the outcome of experiments conducted in a supersonic jet or other rare gas matrixes.

Various experimental observations provide strong evidence for the superfluidity of helium nanodroplets. The first one was the rotationally resolved infrared spectrum of the SF_6 [2], showing a fine structure which is usually only detectable in gas phase experiments. It was clear evidence for the free rotation of the molecule inside the droplets without any friction. By fitting the experimental data a temperature of only 0.38 ± 0.01 K [2] could be determined. This temperature is far below the λ-point. All rotationally resolved spectra taken for molecules in helium droplets confirmed the temperature of 0.38 K and are consistent with theoretical predictions [11]. Additionally, for SF_6 a red shift of the ν_3 vibrational frequency could be found. This shift is in the order of 1 % of the value observed in the gas phase and the moment of inertia obtained from the spectrum in helium droplets is nearly increased by the factor 3 compared to the gas phase. This increase could be explained by 8 helium atoms being attached to each of the eight faces of SF_6 octahedron [2] even though the first solvation layer of SF_6 takes more than only 8 helium atoms [3].
Another rotationally resolved infrared spectrum recorded for OCS in helium droplets also revealed a temperature of 0.37 ± 0.02 K as well as an increase of the moment of inertia by the factor 2.8. A simple model predicted a ring of six helium atoms located around the waist of the OCS molecule [57]. It was experimentally determined that this equatorial helium "donut" around the OCS molecule consists of only five ^{4}He atoms [58]. By the examination of the IR spectrum of OCS in ^{3}He droplets it was found that the rotational fine structure had vanished. This is not astounding for a normal fluid since the temperature of ^{3}He droplets of 0.15 K [11, 59] is too warm for ^{3}He to be superfluid. By adding a small amount of ^{4}He to the expanding helium gas it could be shown that about 60 ^{4}He atoms suffice to recover rotational resolution in the IR spectrum of OCS [60]. The experimental observation strongly indicates that

60 helium atoms is the minimum number needed for superfluidity. This microscopic Andronikashvili experiment proposed that the appearance of sharp rotational spectra of a single molecule is a microscopic indication of superfluidity [60]. The number of 60 is consistent with path integral Monte Carlo calculations which provided evidence for superfluid behavior of pure ^{4}He clusters with only 64 atoms [61].

Furthermore, an important experimental observation could be found in the electronic spectrum of glyoxal in helium droplets. Apart from the sharp zero phonon line (ZPL cf. chapter 2.3.2) glyoxal also shows a broad signal called phonon wing (PW cf. chapter 2.3.3) [62]. The phonon wing exhibits a very characteristic spectral shape which resembles the spectrum of elementary excitations of superfluid helium. This was extracted from neutron scattering on bulk superfluid helium [63, 64]. The matching of the experimental data of glyoxal and the simulation provide experimental evidence for superfluidity of ^{4}He droplets.

2.2.1 Generation of Superfluid Helium Droplets

The helium droplet technique is based on an adiabatic expansion of highly purified (99.99990 % helium), precooled helium under high stagnation pressure (5 bar $< p_0 <$ 80 bar) through a small (5 μm $\leq d_{\text{nozzle}} \leq$ 10 μm) cold (5 K $< T_0 <$ 25 K) orifice into a vaccum chamber. Under these conditions the helium expands either from the gas phase or from the liquid phase. In the first case adiabatic expansion and many-body collisions cause condensation of droplets. In the second case a liquid expands into the vacuum chamber which defragments into droplets due to the surface tension. This expansion proceeds isentropically [65]. A series of isentropes are shown in the phase diagram in Fig. 2.2 as dotted lines. The isentropes differ in the starting conditions given by the nozzle temperature T_0 and the stagnation pressure p_0. These are divided into three sections addressed as I, II, and III. Those in section I start from the gas phase, while those in section III expand from the liquid phase. The section II addresses the singularity of an expansion which directly approaches the critical point (T_c, p_c) and proceeds along the critical isentrope. Accordingly, expansion from section I is called sub-critical whereas expansion from section III is called super-critical [38]. The droplets generated under super-critical conditions are profoundly bigger than the droplets generated under sub-critical conditions. The isentrope, which contains the critical point ($T_c = 5.2$ K and $p_c = 2.26$ bar) and hence separates area I from III, is called critical isentrope. As referred in [38], this isentrope and the isentropes located nearby the critical one form area II. At the critical point it is not possible to distinguish between the gaseous state and the liquid state. They are coupled with each other. Above T_c the helium can be found in its gaseous state. In contrast to the equation existing for area I, analytical equations for the isentropes in area II and III cannot be derived [38]. The resulting mean droplet size and its distribution as well as the speed distribution and the mean velocity $\bar{v}$ depend on the stagnation pressure p_0 and the nozzle temperature T_0 and thus, on the expansion mechanism (sub-critical / super-critical) [38, 66–71]. Experiments revealed that the mean velocity $\bar{v}$ of the helium droplets ranges from 200 $\frac{\mathrm{m}}{\mathrm{s}}$ up to 400 $\frac{\mathrm{m}}{\mathrm{s}}$ at higher nozzle temperatures. The velocity distribution is found to be very sharp ($\frac{\delta v}{v} \approx 0.01 - 0.03$) [4, 38]. For sub-critical expansion the droplet size distribution could be determined by deflection experiments of the droplet beam by a secondary beam of heavy molecules such as SF_6, crypton or argon [67, 68] as well as by attenuating the droplets by the electrons of a mass spectrometer ionizer [72]. It was shown that this droplet size distribution follows a log-normal distribution [68]:

$$f(N) = \frac{1}{N\sigma\sqrt{2\pi}} \cdot \exp\left(-\frac{(\ln N - \mu)^2}{2\sigma^2}\right). \tag{2.2}$$

This function corresponds to a Gaussian function, however, with the square of the logarithm of the variable in the exponent. It is the probability distribution for the droplet size given by the number N of helium atoms in a droplet. The parameters μ and σ are dependent on the source conditions and can be calculated by the equations 2.9 and 2.10 [65]. In figure 2.4 the log-normal function is plotted for different

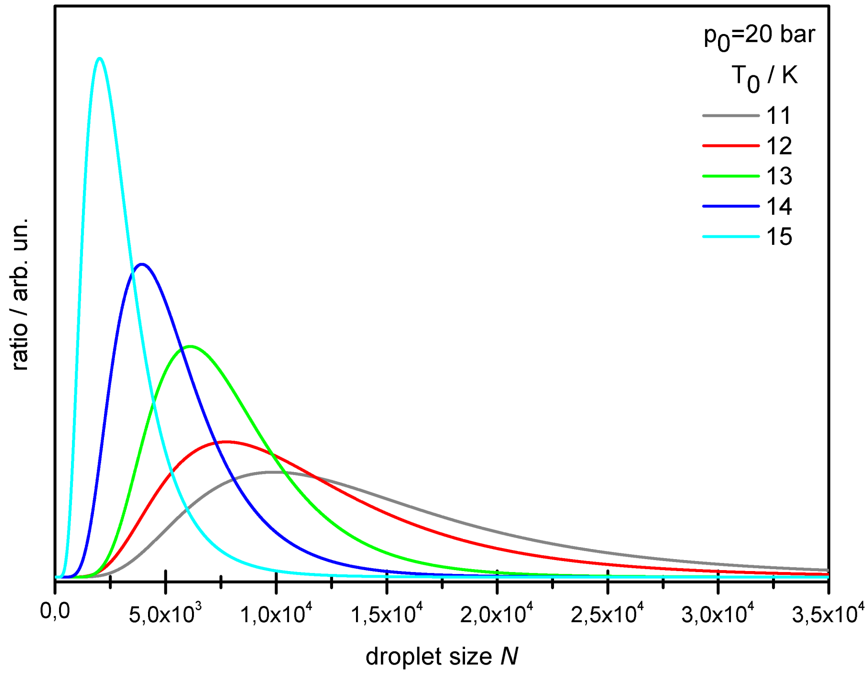

Fig. 2.4: Plot of the size distribution of the helium droplets (sub-critical) for different nozzle temperatures T_0 and a stagnation pressure p_0 of 20 bar. The curves were calculated with data obtained by Schilling [65] and the equation 2.2. The higher T_0, the more pointed the distribution. Its mean value also shifts to smaller droplet sizes simultaneously.

nozzle temperatures T_0 and at a stagnation pressure of $p_0 = 20$ bar. An increase of the width of this distribution can be recognized for a decreasing temperature T_0 of the nozzle. The full width at half maximum (FWHM) $\Delta N_{\frac{1}{2}}$ was determined experimentally and it was found that helium clusters between $1 \cdot 10^3$ and $1.5 \cdot 10^4$ follow the equation $\Delta N_{\frac{1}{2}} = (0.88 \pm 0.06) \cdot \bar{N}$ [65]. The theoretical equation 2.3 of $\Delta N_{\frac{1}{2}}$ depends on μ and σ:

$$\Delta N_{\frac{1}{2}} = \exp\left(\mu - \sigma^2 + \sigma\sqrt{2\mathbf{ln}2}\right) - \exp\left(\mu - \sigma^2 - \sigma\sqrt{2\mathbf{ln}2}\right). \tag{2.3}$$

The maximum of the droplet size distribution can be calculated with the equation

2.5

$$\frac{df}{dN} = 0! \tag{2.4}$$

$$N_m = \exp\left(\mu - \sigma^2\right). \tag{2.5}$$

In this equation N_m represents the most probable droplet size with its probability

$$f_{max} = \frac{1}{\sigma\sqrt{2\pi}}\exp\left(\frac{\sigma^2}{2-\mu}\right). \tag{2.6}$$

The mean droplet size $\bar{N}$ can be calculated by the expectation value of the log-normal distribution following equation 2.7

$$\bar{N} = \exp\left(\mu + \frac{1}{2}\sigma^2\right) \tag{2.7}$$

with a standard deviation $s_{\bar{N}}$

$$s_{\bar{N}} = \bar{N}\sqrt{e^{\sigma^2} - 1}. \tag{2.8}$$

By means of $\bar{N}$ and $s_{\bar{N}}$ the parameters μ and σ can be calculated by following equations [65]:

$$\mu = \mathbf{ln}\left(\frac{\bar{N}^2}{\sqrt{s_{\bar{N}}^2 + \bar{N}^2}}\right) \tag{2.9}$$

$$\sigma^2 = \mathbf{ln}\left(\frac{s_{\bar{N}}^2}{\bar{N}^2} + 1\right). \tag{2.10}$$

The parameters $\bar{N}$ and $s_{\bar{N}}$ were determined experimentally [65] under different source conditions. For a given stagnation pressure p_0 the mean droplet size $\bar{N}$ can be calculated in relation to the nozzle temperature T_0. In Fig. 2.5 the mean droplet size (left ordinate) and the corresponding droplet radius (right ordinate) are plotted as function of the nozzle temperature for a stagnation pressure of $p_0 = 20$ bar. The radius was computed by the equation $r = r_0 \cdot \sqrt[3]{\bar{N}}$ under the assumption of spherical droplets consisting of $\bar{N}$ helium atoms [11]. The van der Waals radius $r_{\mathrm{vdW}} = 220$ pm of a free helium atom was suggested for r_0. It shows that the mean droplet size of

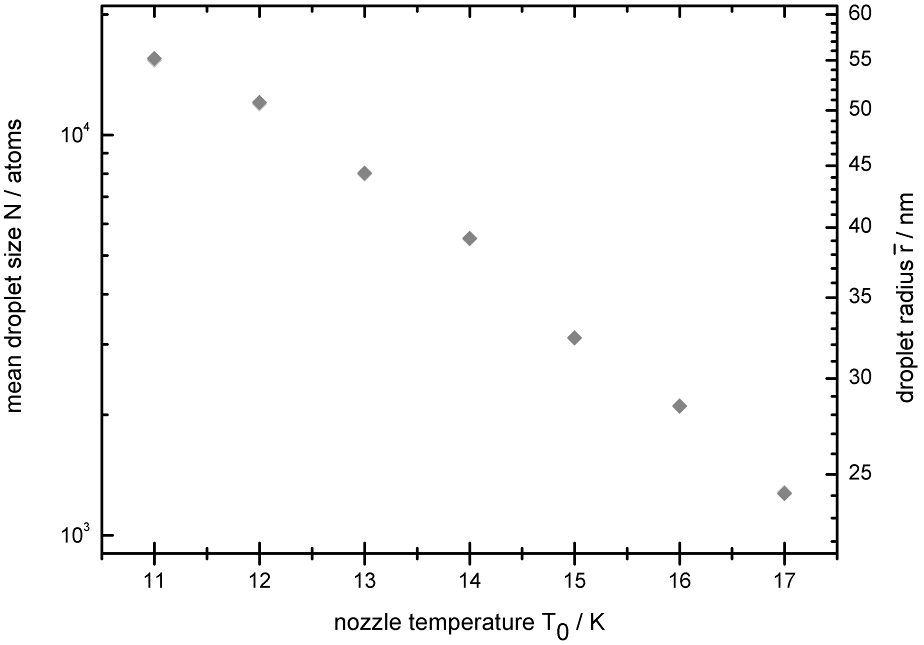

Fig. 2.5: Mean number $\bar{N}$ helium atoms and the calculated mean radius $\bar{r}$ of a droplet dependent on the source temperature T_0 for a stagnation pressure p_0 of 20 bar, based on the experimental data obtained by B. Schilling [65].

the helium beam can be varied between 10^3 and 10^4 atoms by choosing the nozzle temperature accordingly. For super-critical expansion the huge droplet size does not allow for measurable deflection by momentum transfer from a secondary molecular beam. Instead a deflection of charged helium droplets by an external electric field could be analyzed in various scattering experiments [69, 70]. In these experiments an exponential function with negative exponent was found for the size distribution [70]:

$$P_N = \frac{1}{\bar{N}} \cdot \exp\left(-\frac{N}{\bar{N}}\right). \qquad (2.11)$$

With this equation it was possible to determine the mean droplet size for the super-critical helium expansion. The nozzle temperature dependence of the average droplet size as determined experimentally for various stagnation pressures is plotted in Fig.

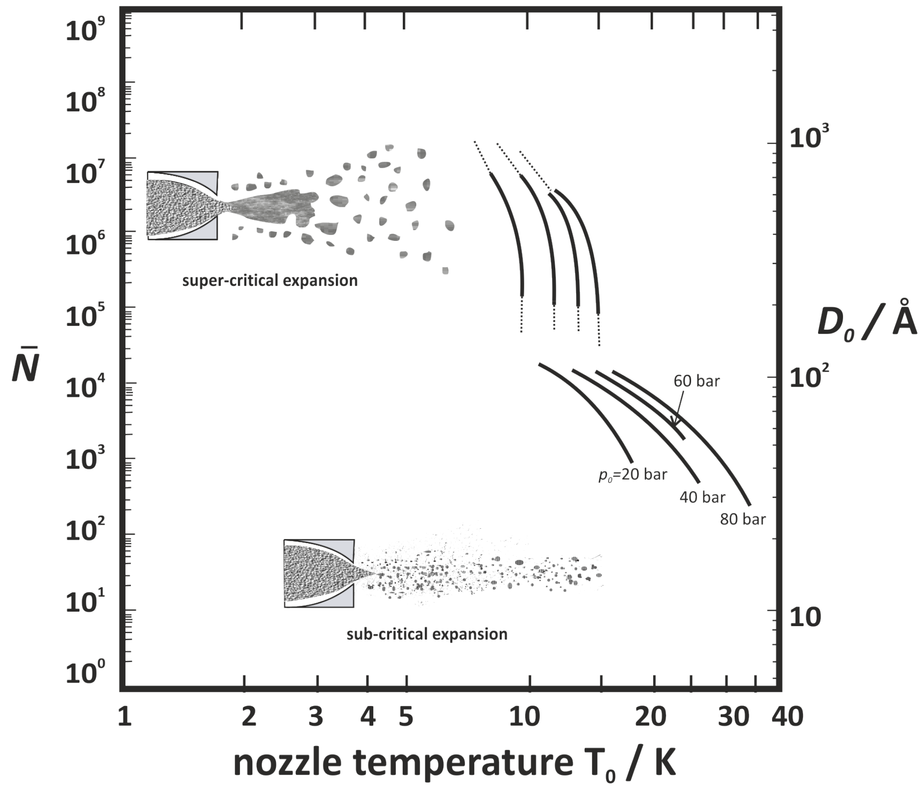

Fig. 2.6: A comparison of the mean droplet size $\bar{N}$ and radius $\bar{r}$ for sub-critical and super-critical helium formation [4]. Sub-critical expansion leads to significantly smaller clusters.

2.6. Recently, these results were confirmed by experiments measuring the attenuation of the droplet beam through collisions with argon and helium gases at room temperature [73]. It was reported that the average droplet size was identified by the attenuation of a continuous helium droplet beam through collisions with argon and helium at room temperature. By the Rayleigh breakup of the liquid of helium jets [74] the generation of micron-sized droplets ($N \geq 10^9$ atoms) is possible. In this case a liquid jet is induced to fragment into a sequence of large monodisperse droplets by Rayleigh oscillations.

The discussed values of the mean droplet size distribution were only valid for the continuous flow helium beam. The droplet size distribution of a pulsed droplet beam was carefully examined for an Even Lavie type pulsed valve modified for the generation of helium droplets [76] by means of Rayleigh scattering and laser-induced

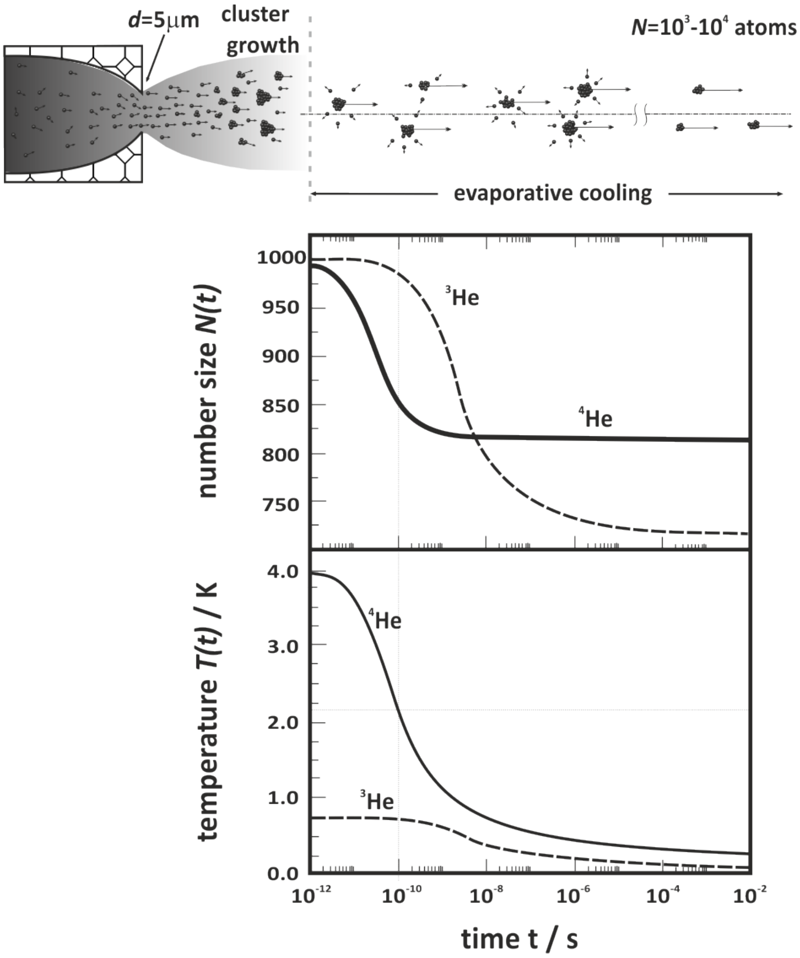

Fig. 2.7: Calculated time evolution of the atom number and temperature of a ^{3}He and a ^{4}He droplet containing 1000 atoms and an initial excitation energy of 1000 K taken from [75].

fluorescence [77]. These results clearly indicate a bimodal droplet size distribution with the smaller fraction in the leading part and very large droplets in the second half of the gas pulse. Upon doping via the pick-up procedure only the leading part with the smaller droplets could be loaded while the back section never revealed a contribution to the laser-induced fluorescence of the dopant. It could be estimated that a size distribution of the smaller helium clusters has to be significantly narrower than a log-normal distribution at an average size which can be varied between 10^4 and 10^6 helium atoms.

Figure 2.7 shows the calculated decrease of a helium droplet (upper pattern) and of the droplet temperature (lower pattern) during the thermalization of the droplet for both isomers, ^{3}He and ^{4}He [75]. It shows that ^{4}He reaches its final temperature in a time scale of nano seconds (10^{-8} to 10^{-7} s [11]). Every single evaporating helium atom is able to cool the droplet by approx. 4 cm^{-1} to 5 cm^{-1} ($\approx$ 7 K) [8, 78, 79]. ^{4}He reaches its steady state faster than ^{3}He. This can be attributed to the higher zero point energy of ^{3}He and thus, to a lower binding energy (E_b = 2.7 K) [4]. Although ^{3}He droplets reach lower temperatures than ^{4}He, they do not cool below the corresponding T_λ (3 mK) and therefore do not reach their superfluid state. The cooling process of any particles inside superfluid helium droplets is accomplished by a very fast dissipation (in the time scale of at least nano seconds [55]) of excess energy (translation, vibrational or rotational energy) into the helium droplet body followed by evaporative cooling. Thus, the cryogenic capability of helium droplets applied to the internal degrees of freedom of foreign particles exceed the corresponding capability of supersonic jet expansion or matrix isolation significantly.

2.2.2 Doping - Pick-up Process

The droplets are doped by a pick-up technique. The helium droplet beam passes a pick-up cell which is filled with a dopant species at a well defined vapor pressure. On its way through the cell, single particles (molecules or atoms) can be captured by the droplets due to inelastic collisions. This method has previously been applied to attaching for example SF_6 molecules to the surface of solid Ar_n clusters [80]. Since the mass of the helium droplets exceeds the mass of the dopant, the deflection of the helium droplets due to the inelastic collisions with the particles is negligible. The pick-up process is dependent on the path length l of the droplets through the pick-up cell and the vapor pressure p_s and thus, the gas phase particle density n_s of the sample inside the cell. This density is essential to control the average number of molecules doped into the helium droplets. Two constraints have to be considered when simulating the pick-up procedure by Poisson statistics [55, 65]. First, the real droplet size distribution is replaced by the value of the average droplet size and, secondly, the effect of evaporative cooling upon the pick-up of every single dopant particle is neglected by using a constant value for the capture cross section. Under these constraints the relation between particle density n_s of the substance and the number k of doped molecules inside one single helium cluster can be calculated by the poisson distribution shown in equation 2.12 [55, 65, 81].

$$P_k(l) = \frac{(\sigma_{cap} \cdot n_s \cdot l)^k}{k!} \cdot \exp(-\sigma_{cap} \cdot n_s \cdot l). \tag{2.12}$$

In the equation 2.12 $P_k(l)$ represents the probability of a droplet to capture k molecules crossing the distance l. Here n_s is the particle density of the probe in the cell and σ_{cap} the scattering cross section of the droplets[5]. For l equal to the length L of the cell, $P_k(L)$ represents the probability that the droplets are doped with k dopants after the pick-up cell. The cross section σ_{cap} is estimated to be equal to the geometric cross section of the helium droplets [4]. Thus, it can be calculated by the equation 2.13 [65].

$$\sigma_{cap}(N) = \sigma_0 \cdot N^{\frac{2}{3}} \tag{2.13}$$

with

$$\sigma_0 = \left(\frac{3}{4}\sqrt{\pi}\frac{m}{\rho}\right)^{\frac{2}{3}}. \tag{2.14}$$

In this equation ρ is equal to the density of the cluster and m is the mass of a helium atom. In case of liquid helium σ_{cap} equals to 15.4 Å$^2 \cdot N^{2/3}$ [65]. By changing the particle density n_s inside the pick-up cell, not only the mean number of k but also the relative probability of droplets doped with a certain number of k dopant particles can be controlled. As a rule of thumb, the partial pressure of the dopant species in the pick-up cell for single particle doping is in the range from 10^{-5} to 10^{-6} mbar [4]. For many substances this range of the partial pressure is reached at

---

[5] Because of the much higher cross section of the helium droplets in the order of nm^2, the cross section of the dopant can be neglected.

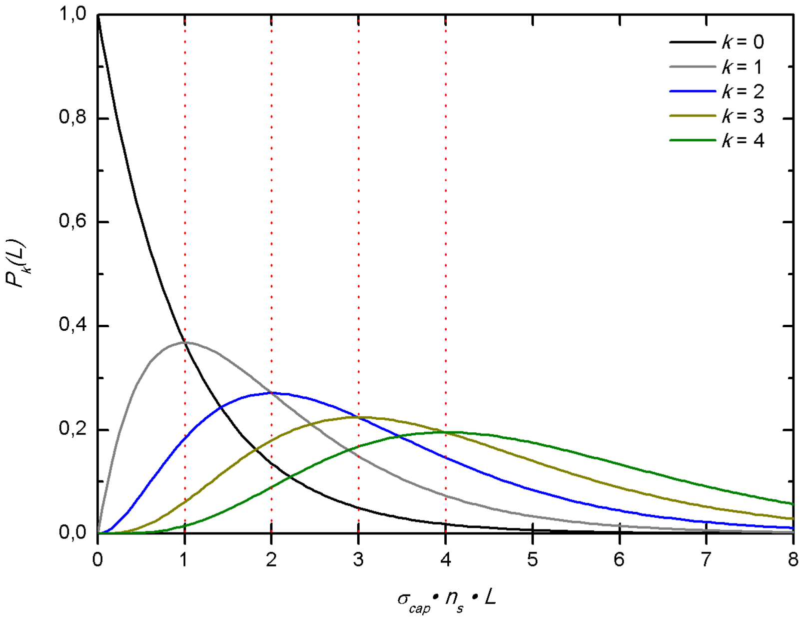

Fig. 2.8: Probability for a single droplet to pick up k dopants while crossing the pick-up cell of the dimension L and the particle density σ_{cap}. The curves were calculated with the equation 2.12. The maxima of each function, shifted by $k \cdot \sigma_{cap} \cdot n_s \cdot L$, are marked by the red dotted lines.

modest temperatures which is fortunate for the class of biomolecules which decompose or denaturate at higher temperatures. Moreover, only negligible amounts of the dopant species are needed compared to a supersonic jet experiment. Finally, the partial pressure needed for single particle doping can be further reduced by extending the length L of the droplet beam path through the pick-up cell. As a plot of the Poisson curves as a function of the partial pressure or particle density reveals, the result of the passage of the droplets through the pick-up cell ends with a distribution of the number k of incorporated particles. This can be seen in figure 2.8 which illustrates the Poisson distribution given in equation 2.12 as a function of the product of the cross section σ_{cap}, the particle density n_s and the length L of the pick-up cell. At the value of $\sigma_{cap} \cdot n_s \cdot L = 1$, for example, one obtains $P_0(L) = P_1(L) = 0.37$, $P_2(L) = 0.18$, $P_3(L) = 0.06$ and $P_4(L) = 0.01$. As a result, 37 % of all droplets remain empty and 25 % carry more than one dopant species. The chemical potential between the dopant and the helium traps the molecule inside the droplet. As mentioned above the energy (internal and kinetic) of the captured particles dissipates into the helium droplets. This energy intake reactivates evaporative cooling so that an energy of approximately 7 K per ^{4}He atom is released [8]. Thus, an energy of 1 eV causes the loss of approximately 1600 helium atoms [4]. The pick-up of a single SF_6 molecule provided under conditions as applied in Ref. [55], for example, is responsible for a loss of about 600 helium atoms [55]. This process defines a minimum size for droplets to be used for single particle doping. One kind of evaporation spectroscopy, which relies on the complete evaporation of the droplets following the excitation of the dissolved molecule and the subsequent detection of the remaining unsolvated molecule by mass spectrometry, demonstrated for benzene, showed that it is considerably more sensitive than the standard beam depletion method [82]. For multiple particle doping the binding energy released by complexation inside the droplet has also to be considered in addition to the cooling of each individual particle. Upon multiple particle doping, clusters are formed inside the droplets because of the free mobility and the attractive, long-range intermolecular forces inside which exceed those from the dopant to the helium environment. Whether one finds clusters surrounded by a solvation layer or with a cluster consisting of molecules individually surrounded by a solvation layer is subject of ongoing research on microsolvation in helium droplets. Another interesting point in the interaction between helium and dopant is worth mentioning. There are two types of dopants, namely heliophobic and heliophilic particles [3, 83]. For the first case, which includes the alkali metals and most of the alkali earth metals, the species remains on the surface of the helium droplets, whereas for the latter one, which includes almost all other elements as well as molecules, the species resides inside the helium droplets. The molecules examined in this work qualify for heliophilic behavior and thus, it can be assumed that they are located inside the droplets.

2.3 Electronic Spectroscopy inside Helium Droplets

2.3.1 Laser-Induced Fluorescence Spectroscopy

Since the dopant to helium interaction is of electrostatic origin, the electronic structure and thus, the valence electrons of the dopant play a key role in the corresponding spectroscopy. Because of that, the electronic degree of freedom of the dopant is of major importance beside vibration and rotation. Due to a comparison of an energy scheme of two electronic states occurring in the gas phase and the energy diagram of these two states in helium droplets, some special effects in the spectroscopic behavior inside helium can be recognized. In figure 2.9 two different electronic states, the ground state S_0 and the first excited one (S_1) of a molecule in the gas phase (left side), are contrasted with the same system when doped into a helium droplet (right side). For the following discussion vibronic or rotational states are neglected. Inside helium droplets both electronic states of a heliophilic dopant species are stabilized, which means exhibiting a reduced energy compared to the gas phase condition. This leads to a change in the transition frequency of the purely electronic transition, the so-called 0_0^0-transition which starts in the vibronic ground state ($\mathrm{v}'' = 0$) of S_0 into $\mathrm{v}' = 0$ of the excited state S_1. This transition is called zero phonon line (ZPL, see chapter 2.3.2). Depending on which electronic state is affected more strongly by the helium atoms, the ZPL can be shifted to the red as well as to the blue[6] and is found to be in the order of ±1 % of the 0_0^0-transition frequency in the gas phase experiment. This value is much smaller than the typical shift found in other rare gas matrices. In addition to pure molecular transitions, which also include vibronic transitions (sometimes even with rotational resolution), electronic spectra show phonon wings

---

[6] Red-shifted transitions, characteristic for large organic molecules attached to rare gases [84] appear at a lower frequency, blue-shifted ones at a higher frequency.

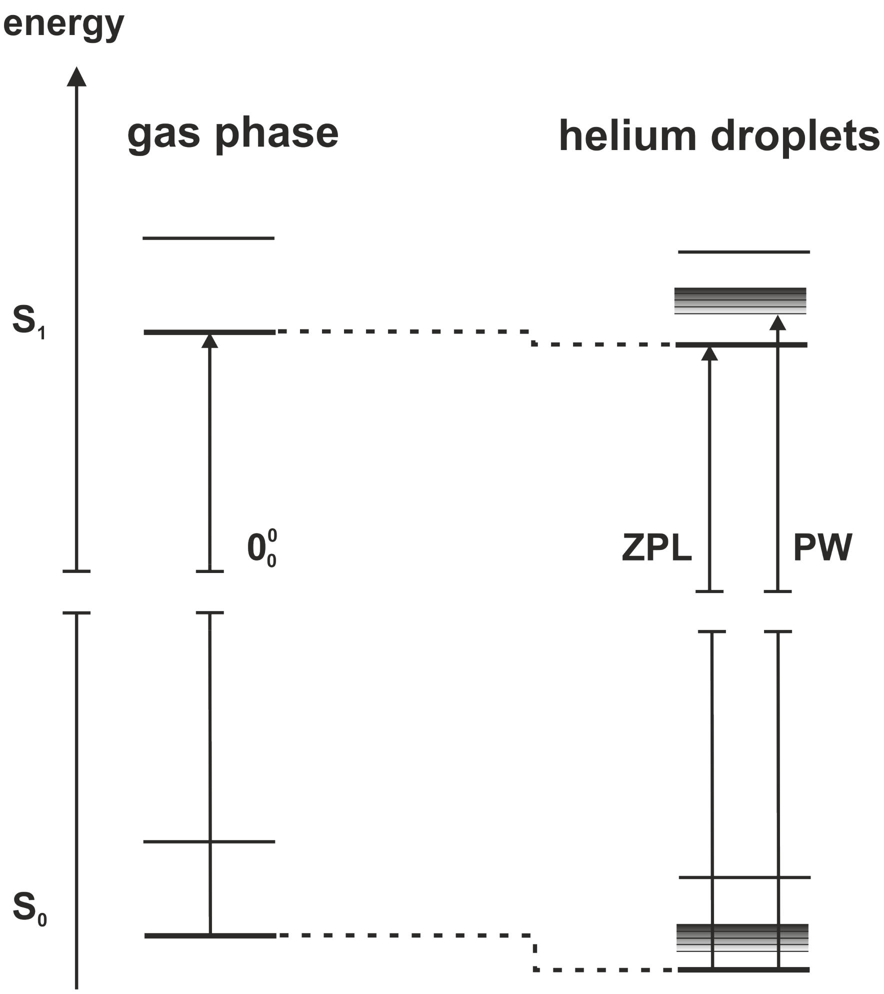

Fig. 2.9: Comparison of an electronic transition between two states S_1 and S_0 of an organic chromophore inside a matrix in contrast to the gas phase [85].

(see chapter 2.3.3) which constitute excitations of the helium environment coupled to the molecular transition. As a result of the low temperature of the superfluid helium droplets phonons are frozen out [86]. Therefore, in excitation the PW appears exclusively on the blue side of the corresponding ZPL. The gap between the ZPL and the first intense peak of the accompanying PW is about 6^{-1} (8 K) [87]. This value corresponds to the energy for elementary excitations of superfluid helium and relates directly to the energy of the roton excitation in bulk liquid helium [4].

2.3.2 Zero Phonon Line

Depending on which electronic state is affected more strongly by the helium atoms, the ZPL can be shifted toward the red or toward the blue compared to the gas phase transition frequency. As it is well known from cluster spectroscopy, the solvent shift increases with the number of attached solvent species in the present case helium atoms. Finally, the solvent shift converges to a maximum value which is reached for droplets at a size where the dopant does not recognize the finite size of the droplet anymore. Inside helium droplets this shift is usually in the order of ±1 % of the 0_0^0-transition frequency found in the gas phase measurement [3] and hence, its value is at least an order of magnitude smaller than shifts observed in solid rare gas matrices. Many substances examined so far in helium droplets show extremely sharp zero phonon lines with a line width below 1 cm^{-1}. In general, the inhomogeneous line broadening caused mostly by the droplet size distribution appears to be less dominant compared to other solid rare gas matrixes. The observation of rather small inhomogeneity in combination with small solvent shifts reflects what is expected from an ideal and extremely gentle host system. Compared to other rare gas matrices with a line broadening of hundreds of wavenumbers the corresponding effect in helium droplets is negligible. For some molecules e.g. pentacene or phthalocyanine [88] only one peak can be found in the ZPL. In contrast, other chromophores such as anthracene [77], indole [89], tetracene [90–92], magnesium- and zincphthalocyanine [93] or phorphine and TPC[7] [94] show multiplet splitting of the ZPL. The reason for this splitting is still controversially discussed and has not been solved. One possible explanation could be the existence of different conformations of the helium solvation layer consisting of helium atoms localized on the surface of the dopant molecule. Finally, there are some interesting results with respect to the examination of the line shape and frequency of the ZPL of phthalocyanine inside helium droplets [13, 95]. It could be shown that the inhomogeneously broadened asymmetric line shape of the electronic origin of Pc reflects the droplet size distribution quantitatively (cf.

---

[7] Tetraphenylchlorine

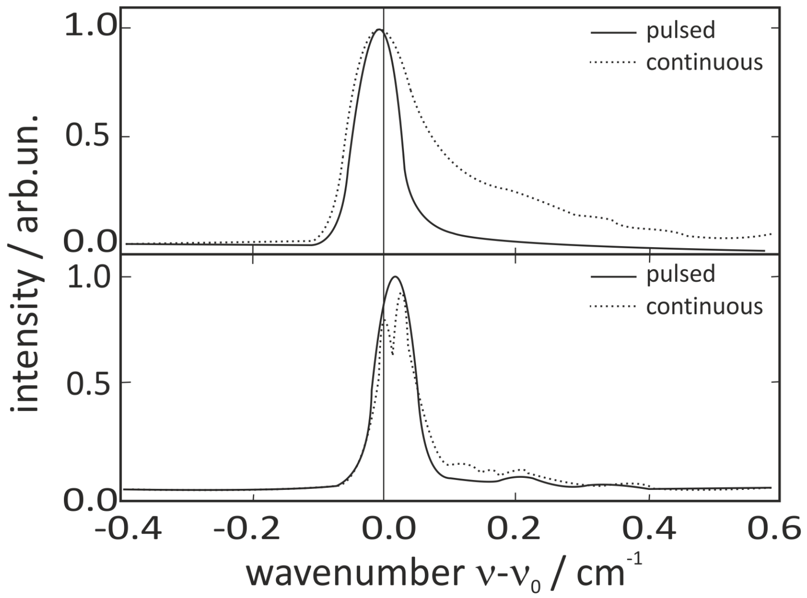

Fig. 2.10: LIF spectrum of phthalocyanine in helium droplets recorded for different expansion conditions. Top panel: continuous source at 20 bar and 11 K. Pulsed source at 80 bar and 25 K. Bottom panel: continuous source at 20 bar and 9.5 K. Pulsed source at 80 bar and 15 K. $\nu_0 = 15088.92\ \mathrm{cm}^{-1}$ [76].

figure 2.10 top panel). This is coherent to the excluded volume model which predicts the solvent shifts induced by a polarizable environment [84]. According to [13, 95] the maximum of the band can be shifted slightly by the experimental conditions. The model presented in Ref. [13] calculates the line shape of the dopant species by considering the actual droplet size distribution and the corresponding probability for single molecule doping. Vice versa, this model can be applied to extract the droplet size distribution from the particular line shape of the electronic origin of Pc in helium droplets. Under super-critical conditions (more than 10^5 atoms per droplet) the inhomogeneity has vanished entirely and the envelope of a rotational fine structure can be resolved for the Pc molecule (cf. dotted line in the lower panel of figure 2.10). These observations reflect the approach to the bulk limit ($> 10^6$ helium atoms) [76, 77]. Surprisingly, these experiments revealed another effect to the transition frequency of the ZPL. Whereas there is a continuous rising red shift, already predicted by the excluded volume model for huge clusters $> 10^5$ atoms [84], the red shift reaches a maximum at a certain average droplet size and for a further increasing droplet size it starts to decrease. Figure 2.10 shows the maximal red shift (top panel) as well as the slightly blue-shifted signals (bottom panel) measured in the pulsed as well as in the continuous helium beam. Up to now there is no explanation of this turn around the solvent shift which was also reported for tetrazene [92, 96].

2.3.3 Phonon Wing

In addition to the ZPL most molecules also show the blue-shifted phonon wing in electronic spectra. This phenomenon, which originates from excitation of the helium environment coupled to molecular excitations, exhibits a different saturation behavior than the corresponding ZPL. At low laser fluence ($\approx 1\ \mu$J per 10 ns pulse) the ratio of the ZPL and PW intensities is typically found to be less than 0.1 [4]. In general, the intensity of the PW rises linearly with the intensity of the laser, whereas the intensity of the ZPL can already be saturated. Consequently, by choosing an appropriate laser intensity, electronic spectra of molecules in helium droplets can be measured with or without the PW. The first electronic spectrum was published in 1996 [62] and can be found in figure 2.11. In this experiment the electronic origin of glyoxal in helium droplets was recorded. The upper panel shows the spectrum recorded in ^{4}He, the lower panel recorded in ^{3}He. In both spectra a sharp ZPL at different transition frequencies can be found and only the ZPL in the upper panel reveals rotational splitting. Both ZPL are followed by a broad, blue-shifted signal which can be identified as the PW. In case of the PW recorded in ^{4}He there is a gap of about 5 cm^{-1} between ZPL and PW. The spectral structure of the PW could be simulated by using the density of states of the phonons convoluted with a Lorentzian function (thin line, top panel). In contrast, the PW accompanying the ZPL of glyoxal in ^{3}He reflects what is expected from a normal fluid at a temperature way above the corresponding λ-point. The density of states of ^{4}He could be determined from neutron scattering experiments [63, 64]. The agreement of experimental result and simulation provides strong evidence for the superfluidity of ^{4}He droplets. Up to now,

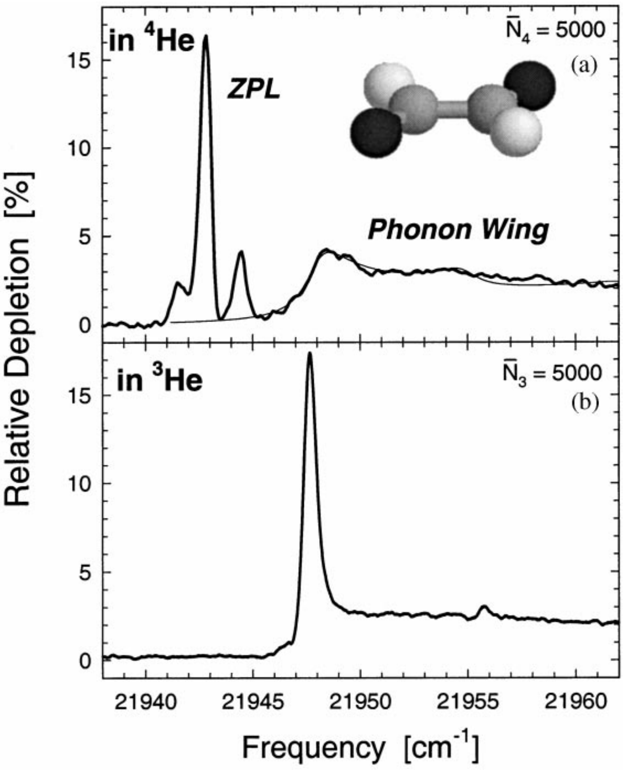

Fig. 2.11: Electronic spectra of glyoxal recorded in ^{4}He (a) and in ^{3}He (b) [97]: The thin line in the upper spectrum shows the simulation of the phonon wing by Hartmann [62].

glyoxal is the only example showing a PW with the spectral shape of the density of states of elementary excitations of superfluid helium. For other dopant species all the characteristic quantities such as phonon gap, maxon and roton maxima are found to be strongly modified or even entirely absent. The spectral shape of the numerous PW reported so far include rich fine structures with line widths identical to the ZPL and / or entirely unstructured signals of some broad undulations extending over several 100 cm^{-1} [94, 98–101]. Up to now these results are not explained comprehensively. There is no theory for quantitative simulation of any PW, not even for that of glyoxal. The simulation presented in Fig. 2.11 given in Ref. [62] was carried out without the glyoxal dopant. Instead, most authors refer to the generally accepted model of a helium solvation complex where the non-superfluid helium solvation layer on the surface covering the dopant molecule warrants for any spectral shape of a PW. This solvation layer may exhibit van der Waals modes coupled to the electronic excitation of the dopant molecule which may appear as sharp lines and have to be counted to the PW of the helium environment [88]. There are some computer simulations for individual PW giving an indication of the validity of this theory, but it has never been extended to a model for predicting the PW of a certain class or even any dopant species [14, 15, 102, 103].

2.4 Emission Spectroscopy inside Superfluid Helium Droplets

The radiative decay of vibronically excited organic closed shell molecules in helium droplets is preceeded by the dissipation of that part of the excitation energy which exceeds the pure electronic excitation to S_1. Thus, radiation originates exclusively from the ground level of the S_1 state. Similar to the ZPL and PW in the excitation spectra, dispersed emission spectra may also show a ZPL accompanied by a PW now on the red side [104]. Since dispersed emission relies on spontaneous emission in contrast to the stimulated one, neither the ZPL nor the PW are ever saturated. They show the natural relation of the transition probability as function of the frequency. In our laboratory, the line widths of the sharp ZPL transitions in the emission spectra are limited by the apparatus function.

Only dispersed emission spectra revealed a doubling effect of the entire emission spectrum of Pc which could be explained by the presence of two variants of a Pc-helium solvation complex. After excitation two independent, dispersed emission spectra, the first emission spectrum (FES) and the second emission spectrum (SES), were found shifted by 10.2 cm^{-1} with respect to each other [105–107]. The two spectra exhibit identical vibrational fine structures and identical Franck-Condon factors. The intensity ratio of both spectra can be varied by the amount of excess excitation energy put into the dopant molecule. With increasing excitation energy the red-shifted emission increases on expense of the blue one. The experimental

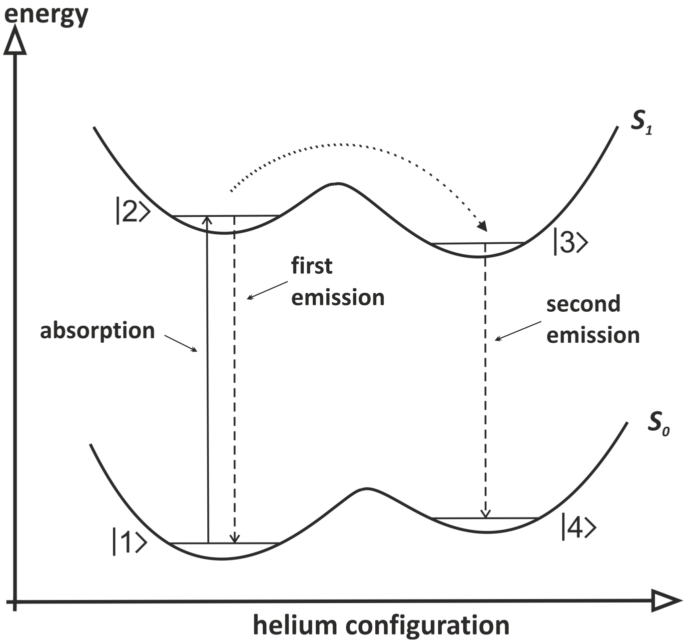

Fig. 2.12: Chart explaining the second emission spectrum which can be assigned to organic molecules i.e. phthalocyanines [104]. It shows the electronic ground state S_0 and the first excited one S_1, each of them with two energetic minima. They represent different arrangements of the helium atoms directly attached to the chromophore. The continuous arrow shows absorption, the dashed arrows give the two different emission spectra and the dotted arrow indicates the rearrangement of the solvation layer.

details recorded in the dispersed emission spectra of Pc could be explained by a model for the Pc-helium solvation complex which is depicted in Fig. 2.12. Starting in the exclusively populated global minimum configuration of the electronic ground state of the solvation complex, electronic excitation creates a metastable configuration which either decays radiatively or relaxes into a global minimum configuration prior to radiative decay. The latter decay path leads to a metastable configuration in the ground state which relaxes into the global minimum with a decay rate of roughly 0.2 MHz [99]. Mg-Pc and one particular van der Waals complex of phthalocyanine with one Ar atom show a similar splitting in the emission [86, 107]. These observations fit to the same model used for explaining the doubling in the emission of Pc in helium droplets [105]. Path integral Monte Carlo simulations revealed a metastable configuration in addition to the global minimum configuration of the helium solvation layer covering the Pc molecule in the electronic ground state. [15].

3 Experimental Setup and Methods

The setup of two different droplet beam apparatus will be summarized at the beginning of this chapter followed by a description of the laser system, detector units and measuring techniques which were used for the purpose of this study.

3.1 Construction of the Helium Droplet Apparatus

There are two different vaccum machines, one is capable of producing a continuous flow helium droplet beam, the other one is equipped with a pulsed valve generating a pulsed droplet beam.

3.1.1 Continuous Flow Helium Droplet Beam

The basic setup of the apparatus used for the purpose of this study is in general equal to the apparatus described in [2, 108]. Figure 3.1 shows the continuous flow apparatus which is built up from three differentially pumped vacuum chambers. The first one, the so-called source or nozzle chamber, is pumped by an oil diffusion pump Leybold DI 6000 E with a pumping speed of 6000 $\frac{l}{s}$ which is supported by a combination of a mechanical two-stage oil-sealed rotary vane vacuum pump Leybold Trivac D65B (pumping speed: 65 $\frac{m^3}{h}$) connected to a roots blower Leybold Ruvac WAU 251 (pumping speed: 253 $\frac{m^3}{h}$). Inside this chamber the continuous flow nozzle consisting of a copper holder, a gold gasket and a platinum disk with a pinhole of

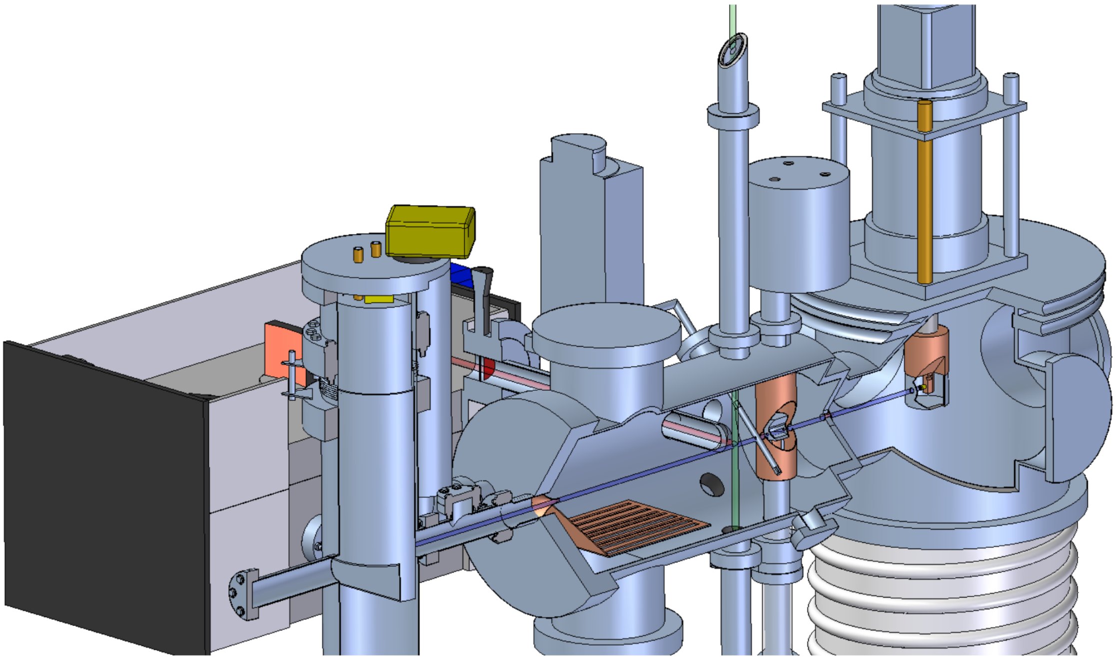

Fig. 3.1: Schematic setup of the continuous flow helium droplet apparatus used for the generation of the helium beam and the spectroscopic experiments.

5 μm is located. This setup is equal to the nozzle described in [2, 38, 108]. The copper holder is attached to the cold head RDK-408 via a copper cylinder. The cold head is connected to the closed cycle cryostat FH-50Hw (both Sumitomo Heavy Industries). By shielding the copper adapter and the orifice with an aluminium cover a contamination with pumping oil is prevented and thus, a plugging of the pinhole is obviated. The cryostat unit and therefore the nozzle can be shifted linearly in all three dimensions during operation. At the second stage of the cryostate (in a distance of about 2 cm) a temperature sensor (Pt100 (2 x 2 mm)) is fixed to measure the so-called nozzle temperature[1] T_0. 1.5 cm further away a heating resistor is in thermal contact with the copper adapter. It is mounted between the adapter and the copper cylinder. With this setup it is possible to tune the temperature T_0 between 7 K and 30 K. The helium inlet tube which is connected to the orifice is wound around the first stage of the cold head to achieve an efficient pre-cooling

---

[1] The actual temperature of the Pt nozzle cannot be measured; thus, T_0 means the measured value of the Pt100.

of the gaseous helium. The helium droplet beam is generated by the expansion of the precooled gaseous helium through the nozzle into the vacuum inside the first chamber (see chapter 2.2.1). For this purpose a high purity of the helium is required (helium 6.0, purity 99.9999 %, Linde AG). Thus, freezing-out of nitrogen or oxygen can be prevented and the contamination of the helium droplets by impurities can be avoided. Approximately 2 cm behind the nozzle the droplets have to pass a skimmer[2] to access the second chamber. It provides better vacuum conditions in the second chamber and leads to a supersonic free jet of helium droplets propagating along a well-defined axis through the second chamber. This so-called detection chamber is pumped by a pumping unit composed of an oil diffusion pump Diffstak 160 (pumping speed: 700 $\frac{L}{s}$) connected to a second mechanical oil-sealed rotary vane vacuum pump Edwards RV12 (pumping speed: 14.2 $\frac{m^3}{h}$). Above the oil pump a plane copper baffle is positioned and linked to a reservoir filled up with liquid nitrogen to reduce the oil from the Diffstak 160 in the background gas of the detection chamber. About 2 cm behind the skimmer the droplet beam can be blocked by a mechanical shutter. Further 13 cm behind the skimmer the droplet beam enters the first pick-up unit. The pick-up cell is designed for solid samples which sublimate into the gas phase controlled by temperature tuning. According to the requirements two different cells can be implemented. The first one, an oven, can be heated resistively up to 400°C for the thermal sublimation of the substance. The substance is provided as a pellet and placed at a removable top cover of the oven which is the coldest point of the cell. The second pick-up cell, a cryo cell, can be cooled down to -100°C to reduce the vapor pressure of the substance inside the cell. Both are made of a stainless steel hollow cylinder, which has got two opposite apertures with a diameter of 4 mm. Inside the chamber the pick-up cell is surrounded by a cylindrical copper shield, which also has got two opposite apertures. It functions as a cooling trap for background gas, especially water and any other molecule inside the detection chamber. Therefore this shield is in thermal contact with a reservoir

---

[2] Conical component containing an aperture with a diameter of 0.7 mm.

filled up with liquid nitrogen. The diameter of the copper shield is 6 cm and its two apertures ($\varnothing = 6$ mm) are aligned to the beam axis. The copper shield also avoids thermal radiation emitted by the oven to reach the optical detection unit. The inner diameter of the oven is 20 mm and of the cryocell 28 mm. The temperature inside the oven is measured by a sensor (thermocouple TKA 10/50, Thermocoax) and can be controlled by the electrical power fed into a heating wire (R= 50 Ω) which is wound around the oven. The wire is covered by a stainless steel tube ($\varnothing = 33$ mm) with apertures as the oven. In contrast to the oven, the head of the cryo cell is thermally connected to the cooling trap by means of a copper clamp. A heating resistor (R = 120 Ω) is attached to the bottom of the cell. The probe is inserted into a small blind hole in the center of the head of the cell. The temperature is measured by the same thermosensor which is also contacted to the head via a second blind hole. Both cells can be mounted onto the same cell holder. This is a long stainless steel tube with a diameter of about 3.5 cm which can be rotated around the cylinder axis and shifted along the cylinder axis to align the two apertures of the pick-up cell to the droplet beam axis. Just one of these two cells can be used for the experiment, but they can be exchanged or refilled anytime by moving the cell holder in situ vertical down through an airlock with a gate valve without breaking the vacuum inside the chamber. Only 1 cm behind the cylindrical cooling trap the second pick-up unit is mounted. This cell is a 15 cm long ($\varnothing = 6$ mm) stainless steel tube with a 4 mm hole aligned to the beam axis. This pick-up cell is connected to a reservoir of the dopant outside the chamber and via a leak valve (Oerlikon Leybold Vaccum; gas flow controllable between $5{\cdot}10^{-6}$ and 1000 $\frac{\text{mbar}\cdot\text{L}}{\text{s}}$) the particle density of the probe inside the pick-up tube can be regulated. This pick-up cell can be equally mounted in front of the cooling trap. Thereby the pick-up sequence of different dopant species can be altered. This pick-up cell is fed by gas phase samples or the vapor above its solid or liquid phase. A second skimmer ($\varnothing = 2$ mm) separates the detection chamber and the connecting tube to the third chamber. Right behind this second skimmer the helium beam can be blocked by a shutter made of quartz glass.

species	He_2^+ ion	He_3^+ ion	water	nitrogen	oxygen
mass amu	8	12	18	28	32
amplitude 10^{-10} A	3.0	0.4	0.4	0.4	0.4

Tab. 3.1: Overview of some typical signals recorded by the mass spectrometer in ampere at the conditions p_0 = 20 bar and T_0 = 14 K inside the continuous flow apparatus.

The last chamber, the bolometer chamber, is evacuated by a combination of a third oil-sealed rotary vane vaccuum pump Leybold Trivac S8B (pumping speed: 8 $\frac{m^3}{h}$) and a turbomolecular high vacuum pump Pfeiffer Balzers TPU510 (pumping speed: 510 $\frac{L}{s}$). The silicon bolometer unit #3342 (Infrared Laboratories) is mounted inside this chamber. This thermal energy detector (see chapter 3.2.3) can be adjusted slightly in vertical direction as well as tilted prependicular to the beam axis. At the end of this chamber a quadrupole mass spectrometer (Leybold Inficon Transpector) can be installed. Ions are generated by 70 eV electron impact. They are mass selected by a quadrupole mass filter and can be detected via a faraday cup (FC) or a electron multiplier (EM) (see chapter 3.2.4). If the bolometer is not installed, the droplet beam as well as the pick-up condition can be examined and optimized (cf. chapter 3.3.5) by the quadrupole mass spectrometer.

Table 3.1 shows some typical data obtained with the apparatus at operating conditions recorded by the mass spectrometer. The vacuum inside the chambers is monitored by two Active Inverted Magnetron gauges (AIM-SL-NW25, Boc Edwards) (Penning Gauge) directly mounted to the vacuum chambers (main pressure) and three active Pirani gauges (APG-M-NW16, Boc Edwards) connected to the pressure side of the two oil diffusion pumps (primary pressure) as well as to the pressure side of the turbo pump of the third chamber. The values measured by the gauges are displayed with an Active Digital Gauge Controller (Enhanced Version, Boc Edwards). The main pressure of the bolometer chamber can only be determined by

chamber	**operating pressure [mbar]**				**base pressure [mbar]**			
	T_0 = 10 K; p_0 = 20 bar				T_0 = 300 K; p_0 = 10 bar			
	continuous		p_0 = 80 bar pulsed		continuous		pulsed	
	primary	main	primary	main	primary	main	primary	main
source	$5.5 \cdot 10^{-2}$	$5 \cdot 10^{-5}$	$2 \cdot 10^{-5}$	$1 \cdot 10^{-5}$	$1.2 \cdot 10^{-2}$	$2 \cdot 10^{-6}$	$2 \cdot 10^{-2}$	$2 \cdot 10^{-6}$
detection	$2 \cdot 10^{-2}$	$3 \cdot 10^{-7}$	$2 \cdot 10^{-5}$	$9 \cdot 10^{-7}$	$5 \cdot 10^{-3}$	$5.5 \cdot 10^{-8}$	$2 \cdot 10^{-3}$	$1.5 \cdot 10^{-7}$
bolometer	$1 \cdot 10^{-1}$	$2.5 \cdot 10^{-7}$	—–	—–	—–	$2 \cdot 10^{-2}$	—–	—–

Tab. 3.2: Typical primary and main pressure data at different expansion conditions p_0 and T_0 inside both apparatus.

the mass spectrometer. Typical conditions inside the different chambers are listed in table 3.2. The high vacuum conditions avoid contamination of the droplets with impurities and are essential for the helium droplet formation and spectroscopic analysis.

3.1.2 Pulsed Helium Droplet Beam

In principle the two apparatus for the generation of the pulsed and the continuous flow helium droplet beam are similar and mainly differ in the helium droplet source. Figure 3.2 shows the pulsed helium droplet machine. It consists of only two differentially pumped vacuum chambers. The first one is evacuated by a pumping unit containing a mechanical oil-sealed rotary vane vacuum pump Pfeiffer DUO 060 A (pumping speed: 60 $\frac{m^3}{h}$) mounted to a roots blower Ulvac PMB 006CM (pumping speed: 500 $\frac{m^3}{h}$). These booster pumps support a turbomolecular pump Pfeiffer TPH 2200 (pumping speed: 2200 $\frac{l}{s}$). The nozzle, a temperature sensor (silicon diode DT-670-BCU, Lake Shore Cryotronics inc.) as well as a heating resistor are mounted to a copper adapter. This one is attached to a home-built copper cylinder which is connected to the cold head RDK-408D2 of the closed cycle compressor unit CSW-71 (Sumitomo Heavy Industries). The cryostat and therefore the nozzle are installed horizontally and can be shifted linearly in all three dimensions during operation. It

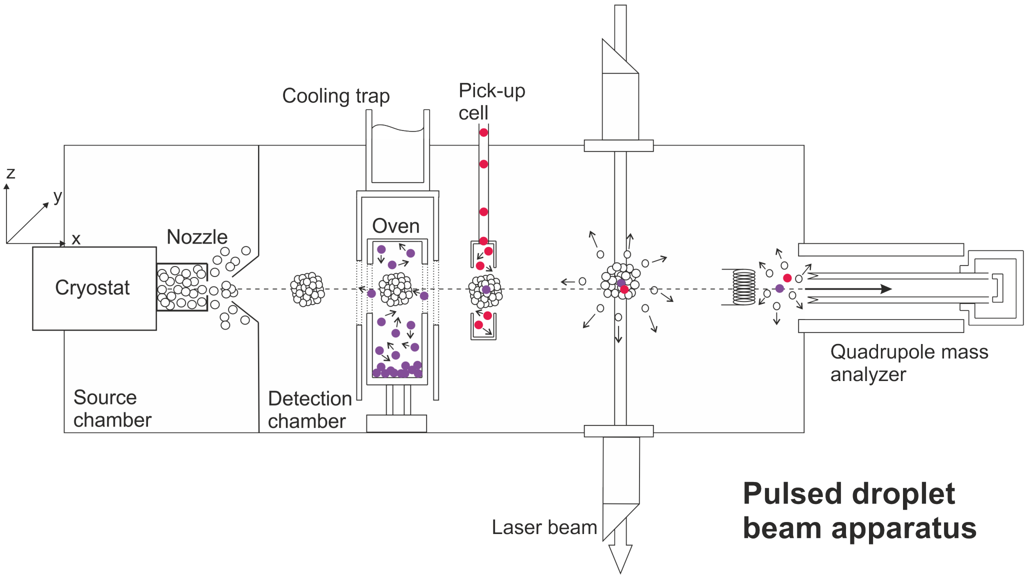

Fig. 3.2: Schematic setup of the pulsed helium droplet machine used for the generation of the pulsed beam and the spectroscopic experiments.

is possible to control the nozzle temperature T_0 from 6 K to 30 K. The main difference between the two machines is the nozzle itself. The pulsed machine is equipped with a pulsed Even-Lavie valve with an orifice of 60 μm in diameter [76, 77] which is used for generating droplets via adiabatic expansion of helium into the vacuum chamber. About 2 cm behind the nozzle the helium droplet beam passes a skimmer ($\varnothing = 6$ mm) which separates the source chamber from the detection chamber. The second chamber is pumped by a turbomolecular high vacuum pump Pfeiffer Balzers TPU510 (pumping speed: 510 $\frac{L}{s}$) backed by a mechanical oil-sealed rotary vane booster pump Pfeiffer DUO 030 A (pumping speed: 30 $\frac{m^3}{h}$). About 15 cm behind the skimmer the droplet beam can be doped by a similar setup as described in chapter 3.1.1. Two different pick-up units are implemented. Solid samples can be sublimated in a resistively heated cylindrical oven. It is also shielded by a copper hollow cylinder which is thermally contacted to a liquid nitrogen vessel outside the chamber. The vapor pressure of the sample inside the cell can be controlled by the electric heating and the temperature is measured by a thermosensor contacted to the bottom of the oven. A cryo cell cannot be implemented in this setup. The second pick-up unit is a reservoir filled with a gaseous or liquid sample outside the vacuum chamber. It is connected to the second pick-up cell. This is a stainless steel tube ($\varnothing = 5$ mm) with a 4 mm hole along the beam axis and can be equally mounted in front or behind the nitrogen cooling trap. The particle density of the sample inside that tube can be regulated via a leak valve (Oerlikon Leybold Vaccum; gas flow controllable between $5 \cdot 10^{-6}$ and 1000 $\frac{mbar \cdot L}{s}$). The pressure inside the two chambers is measured equally to the continuous flow apparatus by 2 gauges in front of the pumps as well as 2 gauges directly mounted to the two vacuum chambers.

3.2 Laser Setup and Detection Unit / Continuous Wave (cw)

3.2.1 cw Laser Setup

Only about 3 cm behind the cooling trap the droplet beam is crossed by the laser beam. The optical axis of the detection unit is perpendicular to the droplet beam axis. The laser used for the purpose of this study is a tunable continuous wave ring dye laser (Coherent Innova 899-29 autoscan) pumped by a high power optically pumped semiconductor laser (OPSL) (Coherent Verdi G10) with an output power up to 10 W at a wavelength of 532 nm. By means of different dyes the ring laser is tunable in single-mode TEM_{00} operation between 560 nm and 700 nm and its line width is only about 500 kHz. The typical output power of the dye laser is 300 mW to almost 1 W. The frequency of the laser is measured by a wavemeter as part of the dye laser system. The entire laser system is controlled via a computer and the smallest frequency step to be chosen is $0.0017\,\mathrm{cm}^{-1}$.

The light is transported by four plane aluminium coated mirrors and finally a quartz prism to the entrance window which is mounted in the Brewster angle (57°) on top of the apparatus at a long stainless steel tube. The linearly polarized laser is guided in p-polarization with respect to the Brewster window in order to minimize reflection.

Between the prism and the Brewster window a home-built Keppler type telescope is mounted in order to control the collimation of the laser beam. Inside the tube there are apertures and it is entirely blackened inside in order to minimize the laser stray light. On the opposite side of the chamber a similar tubing and Brewster window is mounted so that the laser beam can exit with minimum of reflexes.

3.2.2 LIF and Dispersed Emission

Figure 3.3 shows a schematic picture of the optical detection setup, seen along the droplet beam axis. The emerging fluorescence light is collected and parallelly oriented by the lens L_1 (focal length about 6 cm). The switching between PMT and spectrograph is accomplished by a simple pull or push of a deflecting mirror. The R943-02 photomultiplier tube (Hamamatsu) is used to detect the integrated laser-induced fluorescence (LIF) and can be cooled to -25°C to reduce the dark signal. In front of the PMT an edge filter is placed to reduce scattered laser light. It enhances the signal-to-noise-ratio of the spectra. By a third lens L_3 the whole cathode of the PMT is illuminated by the collected light. The focal point of L_3 lies behind the cathode. The signal of the PMT is amplified by a factor of 25 (amplifier Stanford Research Systems SRS 445) and the amplified signal is fed into a photon counter (Stanford Research Systems SR 400) remote-controlled by a PC. On the computer screen the counted events are displayed online and finally saved as individual data files by means of a LabView acquisition program. The synchronization of signal accumulation, data reading, and frequency tuning of the laser is achieved by two trigger pulses. After an experiment is started, the photon counter transmits a pulse to the controlling unit and the laser is set to the starting frequency. As this is done, the laser sends a trigger to the photon counter to start event counting for a given time interval. At the end of this time interval the loop starts again by sending a pulse to the laser initiating a tuning of the laser frequency by a given step. This pulse is also registered by the data acquisition computer to initiate a reading of the counts of the previous cycle from the photon counter. The cycle is repeated until the

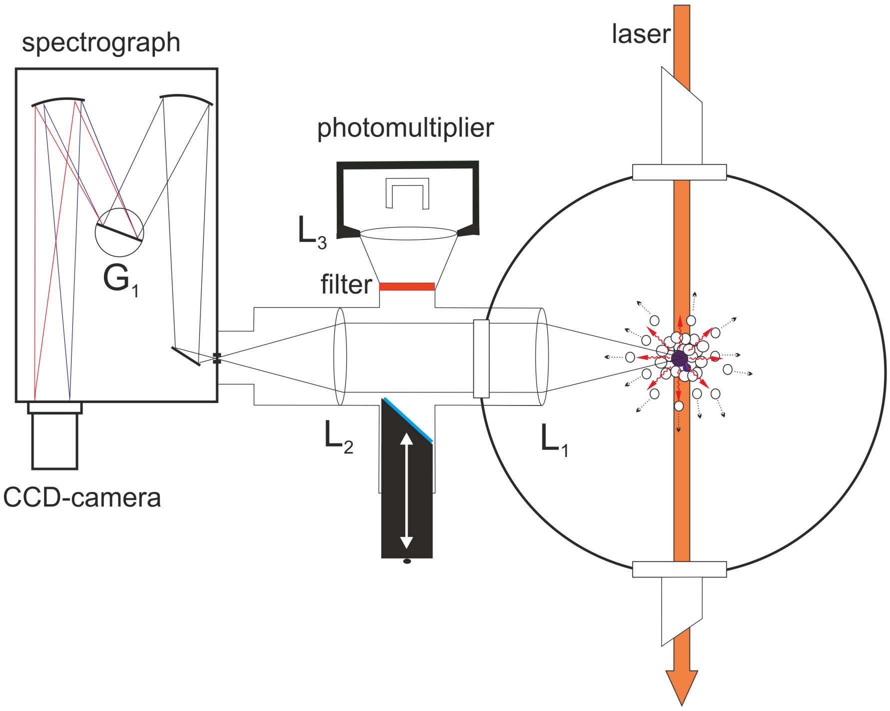

Fig. 3.3: Schematic picture of the optical detection unit (LIF and dispersed emission) used at both helium droplet machines.

last frequency interval is finished. The starting laser frequency, the scan distance as well as the frequency step width has to be defined in the laser software before the experiment is started. The frequency information is only saved on the laser computer by the controlling software and has to be combined with the intensity data saved on the lab computer. This can be easily done because frequency tuning and signal counting is perfectly synchronized so that there are always identical numbers of signal data and frequency data.

The dispersed emission can be recorded by means of a CCD-camera (charge coupled device) (Andor DU401-BV) mounted at the exit port of a spectrograph (Spex 1870 C). The spectrograph operates in Czerny-Turner configuration, its focal length is 50 cm and a grating G_1 with 1200 lines per mm is mounted inside. The chip of the camera is divided into 1024 × 127 pixels, each with a size of 26 × 26 μm. It is cooled to -65°C to reduce dark noise and for long-time acquisition the software eliminates false signals due to cosmic radiation. The parallelly oriented light (L_1) has to be focused onto the entrance slit of the spectrograph by a second lens L_2 (focal length about 10 cm). The lens L_2 can be moved along the connection tube while L_1 is glued onto a stainless steel tube in such a way that the other focal point of L_1 fits to the crossing volume of the laser beam and the droplet beam. The detection unit is used in combination with the continuous flow apparatus. The detection unit at the pulsed apparatus is similar to the described one.

3.2.3 Bolometer Unit

Fig. 3.4: Schematic drawing of the bolometer unit [109].

The bolometer monitors the energy flux on the droplet beam axis. Therefore, it has been mounted to the third chamber by a pair of bellows. The additional vacuum chamber shields the bolometer from any radiation. The connector is constructed in such a way that the bolometer unit can be tilted horizontally as well as adjusted vertically during operation. The bolometer is built up of three main parts, a silicon diode acting as the detector, the dewars and finally the LN6-C #3266 preamplifier (cf. fig. 3.5). The small silicon element is thermally connected to a blackened 2.0 mm × 5.0 mm diameter diamond absorber, bolted to the bottom of the liquid helium vessel and shielded against thermal radiation by a cover mounted to the cold surface of the LN He vessel. The entrance opening of the cover (3.2 mm × 6.0 mm) is in line with four baffles. These baffles minimize the angle of acceptance of the bolometer in combination with the second skimmer which enhances the performance significantly. The largest part of the

Fig. 3.5: Schematic circuit diagram of the LN6-C #3266 preamplifier [109] and the dewar internal components.

bolometer are two vessels on top of each other. The lower one is the liquid helium reservoir ($V_{He} = 2.29\,L$) and the other is a liquid nitrogen reservoir ($V_{N_2} = 1.49\,L$). Figure 3.4 shows the engineering drawing of the bolometer unit [109]. The detector responds highly sensitively to any transferred energy. Therefore it has to be cooled down to a temperature of approximately 1.8 K during the operation. Such a temperature can only be achieved by cooling the system with liquid helium. The work sequence starts with a pre-cooling procedure of the whole bolometer unit to liquid nitrogen temperature of 77 K. For this purpose both vessels are filled with liquid nitrogen. After about 20 minutes a thermal equilibrium should be reached and the pre-coolant liquid nitrogen inside the helium vessel is removed completely and the vessel is filled with liquid helium. Thereby it is important to ensure that there will be no nitrogen left inside the helium dewar. Otherwise the freezing nitrogen on the bottom will constrain the thermal conductivity between detector and the liquid helium reservoir. The helium is transferred from its storage dewar ($V_{He} \approx 100\,L$)

through a thermal-shielded[3] transfer tube (Infrared Laboratories) into the helium vessel of the bolometer. During the first 5 to 8 minutes all of the liquid helium is needed to cool the bottom of the reservoir to 4.2 K. This process is acompanied by violent evaporation of helium gas into the laboratory. As the temperature reaches 4.2 K, the evaporation stops for a short time and the collection of liquid helium starts. As the level of liquid helium rises, evaporation starts again. After about 3 to 5 minutes the reservoir is filled. This is indicated by a visible change of the shape of the helium efflux which is caused by evaporating helium since the liquid He reaches the top of the vessel. This sudden plume of very cold gas signals that the filling procedure is completed. The transfer has to be stopped by pulling the transfer tube out of the liquid helium inside the storage vessel. The helium efflux will be stopped and finally the transfer tube can be removed completely. This whole sequence should take between 8 and 12 minutes and consumes roughly between 4 and 5 liters of liquid helium from the storage dewar. Because of the fact that liquid helium is extremely expensive, this method is economically unviable. Thus, the cold helium efflux has to be transferred to the in-house recondensation factory. Therefore, a home-built transfer adapter on top of the bolometer unit should be used. This is connected via a gas volume flux meter to a pipe which delivers the helium efflux to the in-house recondensation factory. Between the transfer tube and the adapter on top of the bolometer o-ring sealing must not be used. Otherwise it is not possible to remove the transfer tube from the bolometer as long as the adapter is frozen. Thus, there is still a very small helium efflux during the cooling / filling time and not 100 % of the helium can be recycled. Unfortunately, this small efflux does not show the change of its shape when the helium vessel is filled and there is no possibility to measure the filling level of liquid He during the process. Thus, there is no indication when the filling procedure is completed. It was found that this procedure takes significantly more time and has to be continued for at least 25 minutes until enough liquid helium is transferred to the dewar of the bolometer. A

---

[3] The transfer tube is double-walled and evacuated.

reasonable explanation could be an excess pressure inside the helium vessel of the bolometer unit which hinders the transfer of the liquid. But the costs for the liquid helium are anyway reduced to an acceptable level.

Once the vessel is filled, the adapter has to be removed and the helium level inside the dewar can be estimated by using a thin pipe with a membrane on top. Being stuck into the helium vessel the membrane should start a fast vibration when the end of the tube is close to the surface and the vibration should slow down after the tube dips into the liquid.

For the operation mode as well as the standby mode of the filled bolometer unit another home-made adapter has to be mounted on top of the helium fill pipe. It connects the helium dewar to a balloon and an analog manometer[4] (Leybold DIAVAC-K, range between 1 and 760 torr) followed by a regulating valve in front of an oil-sealed single-stage rotary vane vacuum pump (Leybold Trivac S65B pumping speed: 65 $\frac{m^3}{h}$). The pressure side of the pump is connected to the pipe delivering the helium to the recondensation factory. The pump can be bypassed and the manometer can be protected against over pressure by a ball valve. In the standby mode the bypass is opened, the ball valve closed and the balloon acts as an indication of the pressure inside and as a safety vent of the helium vessel[5].

During the measurements the temperature of the detector has to be decreased from 4.2 K down to 1.8 K. This can be achieved by pumping off the helium inside the vessel. Therefore, the bypass has to be closed and the vacuum pump has to be turned on. It should be ensured that the regulating valve is opened slowly and step by step until the final pressure and temperature is reached. This procedure can take up to 30 minutes. The temperature of the liquid and the vapor pressure above the liquid are interrelated. The vapor pressure curve of ^{4}He can be approximated

---

[4] It is mounted about 150 cm behind the bolometer head near the vacuum pump. Hence, the actual vapor pressure above the liquid might differ slightly from this value.

[5] In case of an unexpected breakdown of the vacuum inside the apparatus, stored helium would evaporate spontaneously and the stress could release via the balloon.

	1.25 K - 2.1768 K	2.1768 K - 5.0 K		1.25 K - 2.1768 K	2.1768 K - 5.0 K
A_0	1.392408	3.146631	A_6	-0.017976	-0.004325
A_1	0.527153	1.357655	A_7	0.005409	-0.004973
A_2	0.166756	0.413923	A_8	0.013259	0.000000
A_3	0.050988	0.091159	B	5.600000	10.300000
A_4	0.026514	0.016349	C	2.900000	1.900000
A_5	0.001975	0.001826			

Tab. 3.3: Coefficients A, B and C of ^{4}He in the equation 3.1 according to ITS-90 [110].

T [K]	**second decimal place [K]**									
	0.00	0.01	0.02	0.03	0.04	0.05	0.06	0.07	0.08	0.09
1.2	0.082	0.087	0.093	0.100	0.107	0.115	0.123	0.131	0.139	0.148
1.3	0.158	0.168	0.178	0.189	0.201	0.213	0.226	0.239	0.252	0.267
1.4	0.282	0.298	0.314	0.331	0.348	0.367	0.387	0.407	0.428	0.449
1.5	0.472	0.495	0.519	0.544	0.570	0.597	0.625	0.654	0.684	0.715
1.6	0.747	0.780	0.813	0.849	0.885	0.922	0.961	1.001	1.042	1.084
1.7	1.128	1.173	1.219	1.266	1.315	1.365	1.417	1.470	1.525	1.581
1.8	**1.638**	1.697	1.758	1.820	1.883	1.948	2.015	2.084	2.154	2.226
1.9	2.299	2.374	2.451	2.530	2.610	2.692	2.776	2.862	2.949	3.039
2.0	3.130	3.223	3.317	3.414	3.512	3.613	3.715	3.818	3.925	4.032
2.1	4.141	4.253	4.366	4.481	4.597	4.716	4.836	**4.958**	5.082	5.207
2.2	5.335	5.465	5.597	5.731	5.867	6.005	6.146	6.288	6.433	6.580
2.3	6.730	6.882	7.036	7.192	7.351	7.512	7.675	7.841	8.009	8.180
2.4	8.354	8.529	8.708	8.889	9.072	9.258	9.447	9.638	9.832	10.03
2.5	10.23	10.43	10.64	10.83	11.05	11.27	11.48	11.70	11.92	12.15

Tab. 3.4: Vapor pressure of helium [110] in kPa between 1.2 K and 2.5 K according to ITS-90.

between 0.65K < T < 5.0K by the equation [110]:

$$T(K) = A_0 + \sum_{i=1}^{8} A_i \cdot \left[\frac{(ln(p[Pa]) - B}{C}\right]^i . \tag{3.1}$$

In table 3.3 the coefficients A, B and C are listed. The two temperature ranges of validity are divided by the λ-point. Table 3.4 shows the temperature dependency on the helium pressure between 1.2 K and 2.5 K [110]. The phase transition between normal and superfluid helium starts at a pressure of about 49.58 mbar and the operating temperature of $T = 1.8$ K is reached at a vapor pressure of $p = 16.38$ mbar. Both values are marked in the table. The transition can also be identified by displaying the signal of the bolometer. The time scan can be separated in two sections which differ significantly in the noise. At about 930 s a very short and intense negative peak marks the transition into He II, which is accompanied by a reduction of the noise by orders of magnitude. The large noise is most probable the bolometer

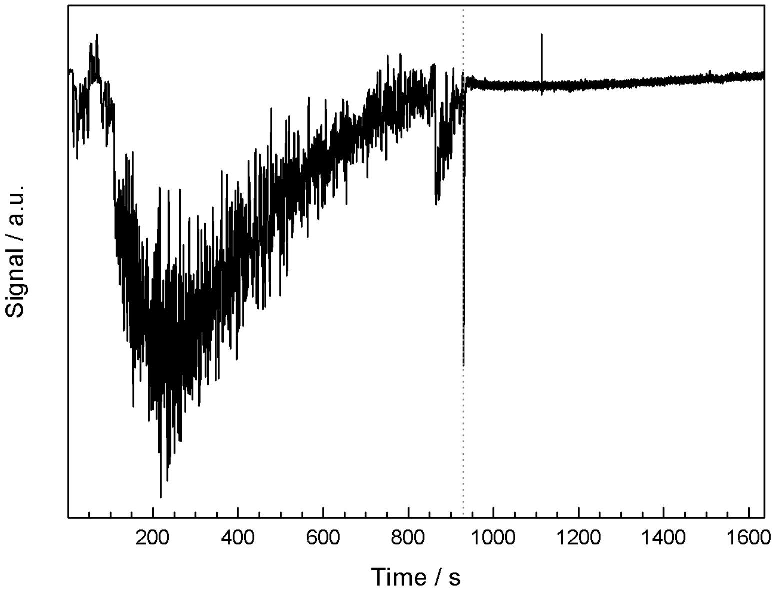

Fig. 3.6: Typical time-dependent curve recorded while the evaporative cooling of the liquid helium inside the helium vessel. After about 15 minutes the change of the signal indicates the crossing of the λ-point.

signal of a classical boiling of the liquid which is known to vanish entirely for He II. A plot of such a typical graph can be seen in figure 3.6, the λ-transition after approximately 15 minutes is marked with a grey dotted line. The manometer shows a value of approximately 30 mbar at the transition. The discrepancy to the expected pressure value listed in table 3.4 is due to the distance of the surface of the liquid and the manometer. The signal generated by the silicon diode of the bolometer is first amplified by a J-FET J230 (junction field effect transistor) coupled via a capacitor ($C_1 = 100\,\mu$F) to the LN-6C preamplifier (cf. fig. 3.5). This amplifier consists mainly of two operational amplifiers OPA LT1007 with an amplification factor of 1:9 and 1:20 (or 1:100). The capacitor accomplishes the reading of a gradient of the energy flux into the detector instead of reading the energy flux itself.

3.2.4 Quadrupol Mass Spectrometer

At the end of the last chamber the quadrupole mass spectrometer Transpector (Leybold Inficon Inc.) can be installed in a centered position to the beam axis. It is able to detect and analyze particles in a mass-to-charge ratio between $\frac{m}{z} = 1$ and 300 amu. Therefore it consists of three main parts: the EI ion source (electron impact ionization), the quadrupole mass filter, and the ion detector (Faraday cup). In case of weak signals an electron multiplier (accelerating voltage $U = -1.2$kV) can be used. The products of the ionization are the molecule with a single electron removed (the so-called parent ion) and two low energy electrons. Beside this reaction, doubly, triply or even more highly charged ions can be generated. In addition to these products, the EI ionization of the molecule can also lead to charged molecule fragments. While the ions may be either positive or negative, the Transpector detects only positive ones. Neutral fragments are not detected, either. The mass spectrometer can be mounted at the end of both helium droplet machines.

3.3 Methods of Detection

3.3.1 Laser-Induced Fluorescence LIF

The detection of LIF signals can be described in the following way. The fluorescence signal of the PMT is registered as function of the laser wavelength. Thus, electronic transitions from the ground state S_0 into higher electronic states are recorded. Since the internal energy of the dopant is entirely frozen at 0.37 K, LIF spectra examined inside superfluid helium droplets reveal the vibrational structure of the electronically excited states. The PMT signal is amplified and finally registered and digitized by means of a photon counter SR400 (cw setup) or a box car integrator SRS 200 (pulsed apparatus) which both are remote-controlled via PC by a home-made LabView data acquisition program. The characteristic spectral features induced by the interaction between the helium environment and the dopant are discussed in chapter 2.3.

3.3.2 Dispersed Emission

The dispersed emission spectrum is recorded by a spectrograph consisting of a grating monochromator with a CCD camera in place of the exit port. The laser is kept fixed at the frequency of one of the resonances recorded in the LIF spectrum. During the aquisition time, the emitted light is dispersed by the grating G_1 inside the spectrograph (cf. fig. 3.3). The CCD chip is capable of storing signals up to 2^{16} events. Thus, depending on the photon flux, the aquisition time has to be adapted to avoid the saturation of the chip. The grating determines the wavelength range covering the CCD chip. With a grating of 1200 /mm the CCD camera views about 40 nm within the red and orange part of the visible spectrum. For the data acquisition the camera software reads the chip in the mode "full vertical binning", which means that all 127 pixels within one of 1024 columns on the CCD chip are read as a single signal. Thus, each spectrum consists of 1024 data points (x/I_x). The camera software can also display a 2-dimensional image of 127x1024 pixels which allows to check for proper coupling of the signal to the center of the CCD chip. The spectral range recorded by the camera can be adjusted by tuning the grating of the spectrograph. The final wavelength scale was not taken from the PC program which calculates this data from optical and geometrical parameters of the monochromator and the grating position. Instead, an absolute calibration was accomplished for each specific position of the grating by means of the spectrum of an Ar-Ne lamp[6], whose wavelength was taken from the NIST data base of atomic lines (National Institute of Standards and Technology [111]). By such measurements a calibration function for the wavelength of each spectrum can be generated. By using of a quadratic function a sufficient calibration of the wavelength can be achieved.

Each frequency interval $\Delta\lambda$ is correlated to an intensity $I_{\Delta\lambda}$. By transforming the wavelength ranges $\Delta\lambda$ into wavenumber ranges $\Delta\tilde{\nu}$, the intensities also have to be transformed because of the non-linear correlation $\lambda = \tilde{\nu}^{-1}$. This can be done by a

---

[6] The glow lamp can be put in front of the entrance slit by removing the tilted mirrow below the PMT.

Jakobi factor. Thus, the conversion of each $\Delta\lambda$ into its $\Delta\tilde{\nu}$ is followed by the calculation of the fraction $\frac{I}{\Delta\tilde{\nu}}$, in which I is equal to $I_{\Delta\lambda}$. This transformation leads to the intensity $I_{\Delta\tilde{\nu}}$ for $\Delta\tilde{\nu}$ and can be plotted as function of the wavenumber. Beside thermal noise which is minimized by the cooling of the CCD chip, electronic noise may pertube the real spectrum. In order to discriminate against electronic noise, a dark spectrum is recorded under the same acquisition conditions as the spectra. The dark spectrum is finally subtracted from each molecular spectrum.

Since the excess energy of the dopant dissipates (cf. chapter 2.2), dispersed emission spectra examined inside superfluid helium droplets reveal the vibrational structure of the electronic ground state.

3.3.3 Depletion Technique

The depletion technique works differently than the optical detection of the LIF signal or the dispersed emission. The basic principle is the detection of a change in the energy flux. As a result of the enormous thermal conductivity of the superfluid helium droplets the mean droplet size will decrease due to the energy dissipation of the dopant. The electronic excitation of the dopant leads to an evaporation of helium atoms until the temperature of the droplets of 0.37 K is reached again (cf. chapter 2.2.1). Consequently, the mean droplet size of the beam will decrease. This attenuation in the helium droplet flow leads to a decrease in the energy flux as long as the laser is resonant to a transition of the chromophore. Since the preamplifier LN6-C is only sensitive to the gradient of a signal, it is necessary to modulate the depletion. This is done by a mechanical chopper[7] (HMS Light Beam Chopper 230) placed in front of the upper Brewster window. Thus, the laser beam is modulated with the frequency of the chopper f_{chop}[8] before it crosses the helium droplet beam. The signal output of the LN6-C preamplifier as well as the measured frequency f_{chop} are fed into the lock-in amplifier SRS 830 (Stanford Research Systems). This

---

[7] A mechanical rotating disc, alternately blocked and free segments of a circle

[8] f_{chop} is measured directly by a sensor mounted to the mechanical chopper.

amplifier extracts only the component f_{chop} of the signal output of the LN6-C. The data is transmitted by the lock-in amplifier to a computer for online displaying and saving on the hard disc.

The communication between the laser control unit and the main software is applied via the lock-in amplifier and can be done by two different modes. In principle it has to be ensured that the signal of the lock-in amplifier is read after a specific time delay and before the laser is shifted by one frequency step. The first mode is similar to the communication sequence used in case of the detection of the LIF signal. There are two communication lines between the laser control unit and the lock-in amplifier. When the laser has reached the starting wavelength, its controlling unit sets the line laser→lock-in ("data flag out") to TTL high and stays as long as the line lock-in→laser ("data enable in") is TTL low. After the selected time delay past the TTL high signal, the signal output of the lock-in amplifier is transferred to the main software where it is plotted on the computer. In the same moment the lock-in amplifier generates a TTL pulse transmitted by the "data enable in" line to the laser control unit. This signal initializes the next frequency step of the laser. During this time the "data flag out" is set to TTL low. When the wavelength is reached, the "data flag out" is set TTL high and the communication circle starts again until the last frequency step is completed. Finally, the data points can be saved by the computer. The intensity information is saved on the lab computer, whereas the laser control software stores to each step the wavelength information deduced by the laser software[9]. Thus, two data files with the same number of rows are created. One represents the depletion signal, the other one the wavelength information and both have to be combined to get the spectrum. The zero position, the length of the intervall and the width of the steps have to be set at the laser controlling software, whereas the delay time has to be set at the main program. During this communication mode, the laser and the lock-in amplifier are communicating for each single step of the laser.

---

[9] Only at the beginning of each segment the wavelength is measured by the wavemeter.

In contrast, the second communication mode works without a comunication between laser and software for each frequency step. The whole scan distance is divided into equal frequency segments of 10 GHz by the laser. The scan time of a segment and the frequency step width have to be determined before the scan. By these constants the time for each step Δt as well as the wavelength $\Delta\tilde{\nu}$ can be calculated. The laser control unit and the main program only communicate at the beginning of each segment. The laser tunes the 10 GHz of each segment without any communication with the main program via the lock-in amplifier. The signal output of the lock-in amplifier is read after the calculated time delay Δt. Thus, the input data which has to be set at the laser controlling unit also has to be set at the main program of the lab computer. At the end of a segment, the laser control unit and the main program are synchronized similarly to the first mode by two TTL-signals. This mode is much faster but it produces a small impreciseness because of a laser intern 10 MHz overlapping area at each segment transition. This error, however, can be neglected as long as the exact value of the wavelength does not matter. The time constant, the sensitivity, signal input, filters and reserve mode have to be set at the lock-in amplifier.

It has to be noted that the depletion of the pulsed helium droplet beam should be more difficult to be detected by the bolometer. Such a pulsed beam already represents a modulated signal generating an intense permanent output signal at the bolometer. Thus, the depletion signal is detected in addition to the permanent signal. Moreover, because of the bimodal droplet size distribution (cf. chapter 2.2.1) of the pulsed beam the absolute depletion is expected to be small since the large droplets cannot be probed. Thus, only the excitation of the doped small droplets contributes to the attenuation of the beam. This should result in a bad S/N ratio.

3.3.4 Stoichiometric Analysis

On the surface or inside the helium droplets different dopants can form complexes by van der Waals forces between the neutral dopants. The dopant-dopant van der

Waals forces are in general stronger than the weak interaction between helium atoms and other atoms or molecules [4, 55]. A complex formation can be achieved by successively doping the droplets with more than one dopant, e.g. atoms or molecules. These dopants are thermalized by the superfluid helium (0.37 K) before the complex is formed. Moreover, the binding energy of the complex can also dissipate. Thus, the spectroscopic study of complexes inside helium droplets profits from the low temperature of the complexes due to evaporative cooling. Since the pick-up process can be described by the Poisson distribution (cf. chapter 2.2.2), the distribution of the stoichiometric number of captured dopants is well-defined after the pick-up unit. For this reason it is possible to study the spectroscopic properties of molecular clusters and thus, their physical behavior within the helium [17, 86, 112]. The complexes can be analyzed by means of rotationally resolved IR spectroscopy and Stark spectroscopy [113–117]. A detailed analysis of the configuration was not possible in case of Pc-Ar_n [86, 107]. However, the stoichiometry of the complexes can be determined by means of electronic spectroscopy. The pick-up process can be described by a Poisson distribution (cf. chapter 2.2.2). It can be assumed that the intensity of the cluster signal in the electronic spectrum is proportional to the amount of these clusters. Thus, the number k of doped particles s can be determined. For this purpose the intensities $I_{spec.}$ of each resonance are plotted against the particle density $\mathrm{n_s}$ of the particle s in the pick-up cell. Then, the experimental data set ($I_{spec.}/\mathrm{n_s}$) of each resonance has to be fitted by a Poisson distribution (cf. equation 2.12) and k is obtained. The result of this analysis is the stoichiometry of the complex responsible for the particular cluster signal. The particle density $\mathrm{n_s}$ in the pick-up cell is measured indirectly. Following the ideal gas law it is proportional to the partial pressure $\mathrm{p_s}$ inside the pick-up cell. Due to effusion the particles s can also be found in the detection chamber, and the partial pressure $\mathrm{P_s}$ in the detection chamber is proportional to the partial pressure $\mathrm{p_s}$ inside the pick-up cell. $\mathrm{P_s}$ can be measured by means of the mass spectrometer since it is proportional to $\mathrm{I_s}$. For this purpose the intensity $\mathrm{I_s}$ at the mass of the particle s or equally at the mass of an ion fragment of the particle has to be monitored. This value reveals the relative particle density n_s in the pick-up cell.

3.3.5 Quadrupole Mass Spectrometer

The quadrupole mass spectrometer (QMS) provides information and control on various important experimental parameters. First, it is possible to check the vacuum conditions inside the apparatus. Due to the huge capture cross section of the helium droplets, high vacuum conditions are required inside the detection chamber to avoid a contamination of the droplets by particles of the background gas. Already the leak rate of gas evolution from the surface of the chamber and especially from the pellet of the probe can lead to a significant partial pressure of oxygen, nitrogen and water. The amount of these substances can be checked over time by the mass spectrometer and spectroscopic experiments can only be executed when the parameters indicate a low contamination of the background gas in the detection chamber. The detection of a signal at 19 amu is an indication of water inside the droplets and thus, it shows that the vacuum quality inside the detection chamber has to be optimized.

Next the quality of the helium droplet beam can be analyzed. During the electron impact ionization of the helium droplets in front of the quadrupole mass analyzer mostly helium ions He^+ ($\frac{M}{Z}$ = 4 amu) are produced, but also helium cluster ions He_N^+ ($\frac{M}{Z}$ = $4N$ amu)[10] are generated. Such a mass spectrum can be found in figure 6.9. The intensity of the helium signals at $4N$ amu is fading with increasing number N of the ion fragment size but nevertheless, it is possible to detect cluster ions over the entire mass range, which means up to He_{75}^+. The detection of these helium cluster signals up to He_{75}^+ in the QMS is an indication for an effective performance of the helium droplet source. The lack of such helium cluster signals indicates that there is a problem in the experimental setup and rectifications are nessecary. This may include the position of the nozzle, a contamination of the nozzle or the skimmer or

---

[10] Only the positively charged ions can be detected by the mass spectrometer (cf. chapter 3.2.4), thus, negatively charged ions are not discussed.

even a damage of a skimmer.

In case of doped helium droplets the mass spectrum shows - alongside the pure helium cluster ions - additional signals which can be attributed to the dopant. These signals include the parent ion at the mass X of the dopant as well as ion fragments of the dopant. Moreover, the mass spectrum also shows signals from complexes between the dopant and N helium atoms at the masses M_{X+4N}. These signals in the mass spectrum are clear evidence that the dopant was solvated in the helium droplets before it reached the ionization region. In case of free molecules from the background gas, these complex signals do not occur.

Moreover, the mass spectrometer signal is essential for the Poisson analysis of the doping as described above (cf. chapter 3.3.4).

Finally, there is another way by which the doping of the droplets can be analyzed by the mass spectrometer. Due to the pick-up of particles there is an attenuation of the intensity of the helium dimer ion signal at $M = 8$ amu. As a rule of thumb experimental conditions which lead to a helium dimer signal of about 80 % in the QMS (compared to the free helium droplet beam) favor single molecule doping. This can be monitored easily by the QMS and reveals an adequate first guess of the experimental conditions needed for a laser spectroscopic examination of a substance solvated in helium droplets.

4 Phthalocyanine

4.1 Introduction

Since the introduction of the helium droplet spectroscopy this technique has been applied to many different phthalocyanine derivates [15, 86, 88, 93, 95, 103, 106, 107, 118, 119]. Phthalocyanine (Pc) is a dark blue powder, can be sublimated and its chemical structure is shown in figure 4.1. This planar aromatic macrocycle (point group D_{2h}) has got a high fluorescence quantum efficiency (QE $= 0.6$ in 1-chloronaphthalene, excitation at $\lambda = 633$ nm [120]). Pc and its derivates can be

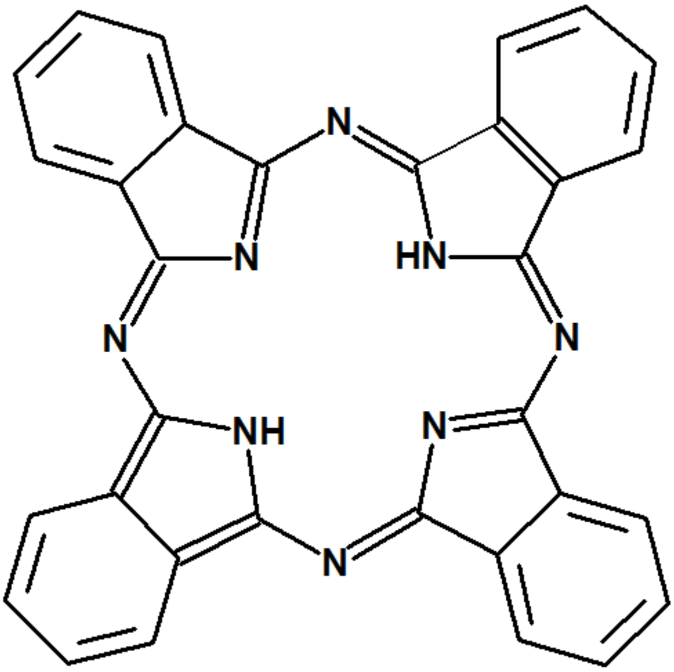

Fig. 4.1: Chemical structure of phthalocyanine.

used for various applications. They can be found as dyes in plastics, paints and printing inks, and are used for the dye of optical data carrier (CD-R) [121]. Moreover, it can be used as sensor material for illumination [122], photovoltaic cells [123], electrode materials in fuel cells [124–127], emitters in OLED[1] devices [128–130] and for optical limiting functional materials [131, 132]. They are also used in clinical therapy [133–140] as photosensitizers in the PDT[2].

The phthalocyanine used for the purpose of this study was purchased from Sigma Aldrich with a purity of at least 98 %. Thus, a further purification was not needed.

4.2 Experimental Results

4.2.1 Laser-Induced Fluorescence / ZPL and PW

First, the ZPL as well as the PW of phthalocyanine should be examined and compared with previous results [13, 86, 93, 95]. The LIF spectrum taken from [86] is shown in figure 4.2. As already known from the available literature, the maximum of the electronic origin can be found at a frequency $\tilde{\nu}_0 = 15088.9\ \mathrm{cm}^{-1}$. This sharp and dominant signal is followed by a structured fluorescence shifted by about $3.8\ \mathrm{cm}^{-1}$ with its maximum at a frequency of $\tilde{\nu} = 15092.7\ \mathrm{cm}^{-1}$ and was assigned to the phonon wing [86]. The distinction between PW and ZPL is usually proven by different transition probabilities between the states and thus, a different saturation behavior of the signals. Nevertheless, this argument does not take different complex forms between helium and the chromophore into account. These structure variants can be seen in analogy to different sites in a lattice and they would also show a different transition probability than the zero phonon line. Another indication of a ZPL can be found in the emission spectrum. Upon excitation at a PW the emission signal has to be red-shifted, whereas only in case of a ZPL of an electronic origin the

---

[1] OLED, organic light emitting diode

[2] PDT, photodynamic therapy: phthalocyanine is enriched inside a tumor and produces after excitation (between 600 and 800 nm) singulet oxygen which destroys the tumor cells.

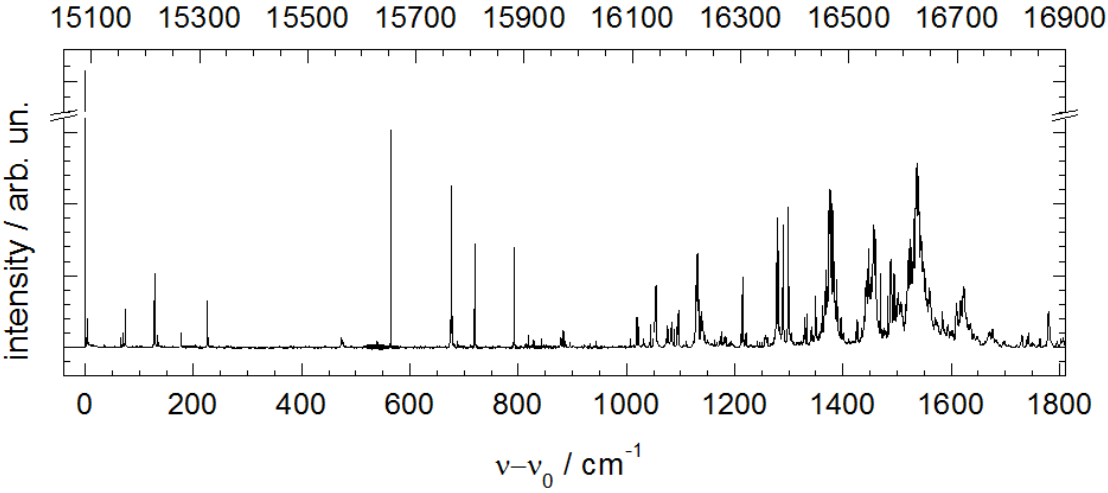

Fig. 4.2: LIF spectrum of phthalocyanine embedded inside superfluid helium droplets (mean droplet size $\bar{N} \approx 20000$) [86].

blue end of the emission and the red side of its absorption signal can be coincident [141]. A ZPL excited at vibronic transitions can also be shifted to lower frequencies. Doubtlessly, this means that we can identify only the electronic origin. But we cannot conclude from a red-shifted emission that a signal has to be attributed to the PW or a solvation complex. Moreover, it is clear that the LIF signal of a PW is red-shifted by the so-called phonon gap (c.f. chapter 2.3) but a ZPL of any other solvation structure would also be red-shifted to the ZPL of the global minimum. Thus, it is not sufficient to check the saturation behavior, if there is a shift in the LIF spectrum or in the emission or even both, to distinguish between electronic transitions of different helium chromophore complexes and PW signals.

Figure 4.3 shows in detail the ZPL of phthalocyanine in helium droplets generated at T_0 = 10.5 K and p_0 = 20 bar ($\bar{N} \approx 20000$). The ZPL has been analyzed with a Gaussian curve and an exponential function to come up to the blue tail of the signal. A more precise simulation of this asymmetric line shape can be found in [13, 95]. The deviation between the simulation and the ZPL near the maximum is attributed to the large frequency step width in the experiment and thus, the data misses the maximum at $\tilde{\nu}_0 = 15088.9\ \mathrm{cm}^{-1}$. Looking at the difference graph (green

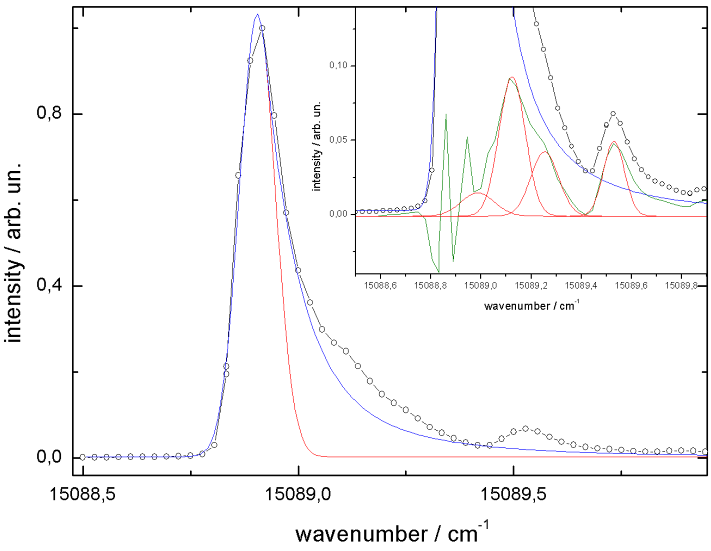

Fig. 4.3: Electronic origin (ZPL) of phthalocyanine in helium droplets (mean droplet size $\bar{N} \approx 20000$). The fit (blue) includes a Gaussian curve (red) as well as an exponential function. The green curve shows the residuum between data and fit. The remaining signals were analyzed with Gaussian functions.

curve Fig. 4.3) at least four more signals near $\tilde{\nu}_0$ can be found. The fluorescence between $\tilde{\nu} = 15089.0\ \mathrm{cm}^{-1}$ and $\tilde{\nu} = 15089.5\ \mathrm{cm}^{-1}$ and the resonance at $\tilde{\nu} = 15089.5\ \mathrm{cm}^{-1}$ were fitted with Gaussian functions. All parameters of the fit are listed in table 4.1. The width of these signals varies between the 1.0 and 1.5 times of the FWHM of the electronic origin and amplitudes between 1.5 % and 9.1 % can be found. Nevertheless, these values must be seen critically because of the asymmetric line shape of the ZPL which was approximated by an exponential function. In this respect, the signal at $\tilde{\nu} = 15089.5\ \mathrm{cm}^{-1}$ seems to be the most reliable one and the information of the fit reveals an intensity of 4.9 %, a width which is in the same order of magnitude than the width of the origin within the scope of the measurement accuracy. It also shows an asymmetric line shape at its blue side similar to the ZPL.

In figure 4.4 the black curve shows the laser-induced fluorescence of the phonon wing between $15091.5\ \mathrm{cm}^{-1} \leq \tilde{\nu} \leq 15094.5\ \mathrm{cm}^{-1}$. The offset of about 0.01 is thought to

	frequency cm^{-1}	**amplitude** a.u.	**FWHM** cm^{-1}
ZPL	15088.9	1.000	0.097
	15089.0	0.015	0.15
	15089.1	0.091	0.12
	15089.3	0.042	0.13
	15089.5	0.049	0.099
PW	15092.5	0.057	0.157
	15092.7	0.124	0.20
	15092.9	0.035	0.18

Tab. 4.1: Frequency, amplitude and full width at half maximum derived from the Gaussian fit data. The amplitudes were normalized to the electronic origin.

orginate from the blue asymmetric tail of the ZPL. On top of this signal a structured signal could be detected which is thought to be the spectral signature of the phonon wing of phthalocyanine in superfluid He droplets. It has been normalized to the maximum of the electronic origin and has been analyzed with different Gaussian functions (red). The offset was implemented into the fit and the sum of the Gaussians is represented by the blue dotted graph in figure 4.4. The parameters of the Gaussian fit applied at the maximum $\tilde{\nu}$ = 15092.7 cm^{-1} and the two fits next to it can be found in table 4.1. These three peaks were sufficient to reproduce the most intense signal of the PW. They are highlighted in bold and are marked with black arrows in figure 4.4. Comparing their line shapes with the line shape of the ZPL reveals that they also show an inhomogeneous line broadening. It reveals a Gaussian shape with a FWHM between 1.5 and 2 times of the width of the ZPL. Furthermore, the asymmetric blue tail of the ZPL could not be found at the signals of the PW. The parameter of the other fitted peaks are not listed because they could not be determined evidently enough.

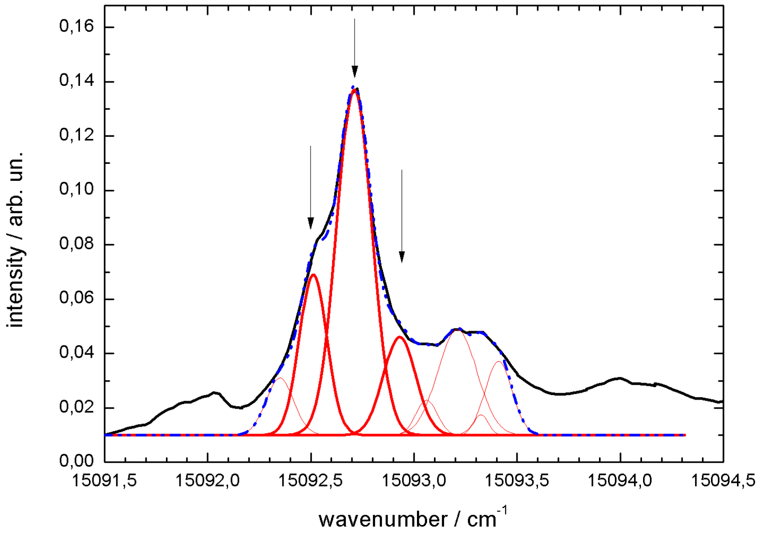

Fig. 4.4: LIF signal of the phonon wing (black) of phthalocyanine inside helium droplets recorded at a nozzle temperature $T_0 = 10.5$ K and $p_0 = 20$ bar ($\bar{N} \approx 20000$). The signal has been normalized to the maximum of the ZPL and was analyzed with Gaussian curves (red). The blue line shows the sum of the Gaussian functions.

4.2.2 Saturation Behavior of Pc

To obtain more information about the LIF signal of the ZPL and the PW, the saturation behavior of both signals has been examined. Figure 4.5 shows the ZPL (a) as well as the PW (b) of phthalocyanine measured with different laser intensities at $T_0 = 10.5$ K and $p_0 = 20$ bar. The laser intensity has been reduced by the usage of a polarizer in front of the upper brewster window. The two bold lines (black and purple) represent the signal at linear and nearly prependicular alignment of the polarizer with respect to the polarization of the laser light. The intensity of the excitation laser beam inside the vacuum chamber is mainly determined by the angle of the polarizer with respect to the plane of polarization of the linearly polarized laser beam. Finally it is slightly modified by the Brewster window with respect to both, the intensity as well as the plane of polarization. It has to be taken into account that even at an angle of 90° (cf. purple curve Fig. 4.5) the attenuation of the beam by the polarizer

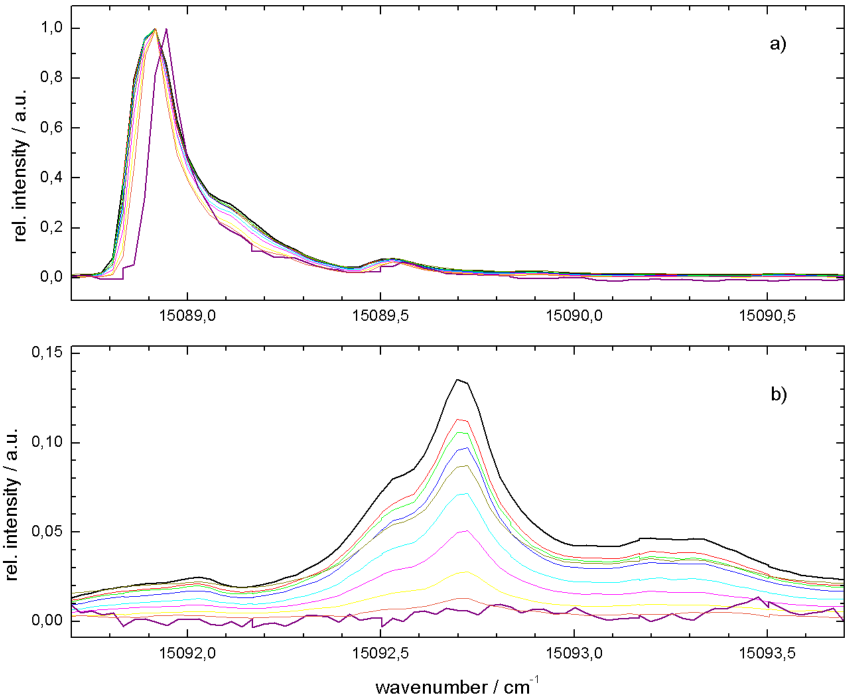

Fig. 4.5: ZPL (a) and PW (b) recorded with laser lights with different intensities at a nozzle temperature T_0 = 10.5 K and p_0 = 20 bar ($\bar{N} \approx 20000$). The data has been normalized to the maximum of the ZPL.

does not reach 100 %. The signals have been normalized to the maximum of the ZPL. The shift of the purple curve in figure 4.5 (a) has to be attributed to a shift of the laser of one frequency step. Its very low signal intensity as well as the poor signal-to-noise-ratio are caused by the low laser intensity at a polarizer position of 90 °.

Panel (a) (Fig. 4.5) shows that the line width of the ZPL changes from the orange to the black curve. At higher laser intensity it increases at the blue as well as at the red side. It could be shown that this change is due to a homogeneous line broadening caused by the saturation of the electronic transition at higher laser intensity. It was possible to reproduce the ZPL of the black curve by a convolution of the orange spectrum with a Gaussian function. Thus, this line broadening originates

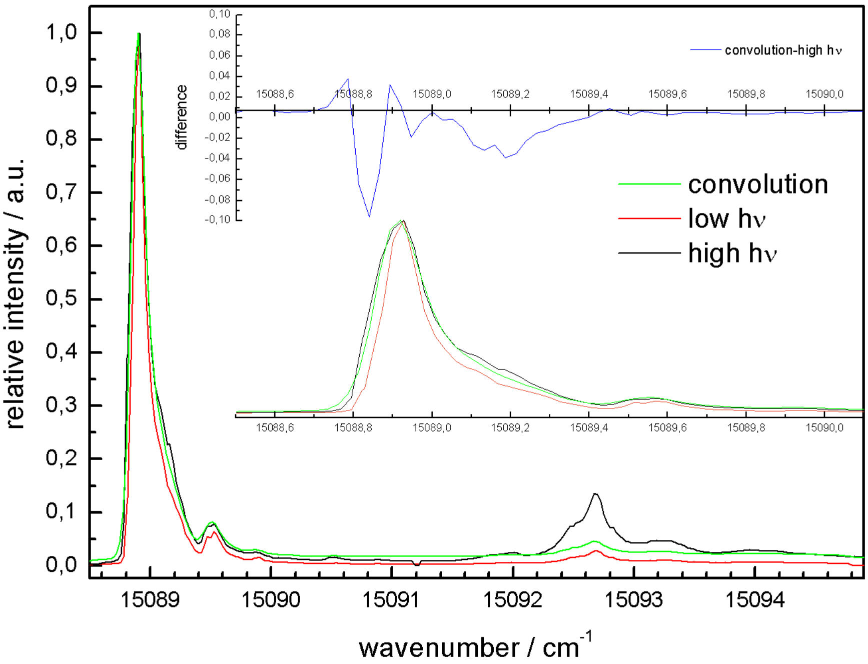

Fig. 4.6: ZPL recorded upon excitation at high (black) and low (red) laser intensity as well as the convolution of the red curve with a Gaussian function (green). The enlarged image shows only the ZPL as well as the residuum (blue) of the black and green spectrum in this range.

from the saturation of this transition. As it can be seen, figure 4.6 shows the ZPL recorded with high (black) and low (red) laser intensity as well as the convolution of the red curve with a Gaussian function (green). At the enlarged area the ZPL as well as the residuum (blue) of the black and green graph can be found in this range. The residuum reveals the deviation between convolution and most saturated signal around the ZPL. The deviation at the blue side as well as around the maximum of the ZPL is apparently caused by the large frequency step width used in this experiment. Beside these experimental artifacts, the residuum reveals another signal around $\tilde{\nu}$ = 15089.2 cm^{-1} on top of the blue asymmetric tail of the ZPL which cannot be attributed to experimental inaccuracy. It appears with rising laser intensity and hence, this weak signal shows a saturation behavior which is different than at the ZPL. In figure 4.3 it can be seen that it can only be reproduced by more contributions. One explanation for that could be the overlapping of electronic origins of different solvation configurations of the helium-phthalocyanine complex with slightly higher transition energies. The small spectral intensity may reflect a very weak transition dipole moment or a small population of these states or both. Since there is no method of predicting the transition probability of such unknown states, the saturation behavior neither supports nor opposes to this explanation. As long as the transition energy is a measure of the energetic difference between two states, it does not provide any information about the absolute values of the electronic levels. Consequently, they could be higher, lower and even nearly equal situated to the corresponding states which are responsible for the electronic origin at $\tilde{\nu} = 15089.0\ \mathrm{cm}^{-1}$. This means that it is not possible to deduce the occupation of such states by comparing the temperature inside the droplets ($\mathrm{T} = 0.37\ \mathrm{K} \mathrel{\hat{=}} 5.108 \cdot 10^{-24}\ \mathrm{J}$) with the energy gap of only $0.2\ \mathrm{cm}^{-1}$ ($\hat{=}\ 3.9756 \cdot 10^{-24}\ \mathrm{J}$). Consequently, the data shown in figure 4.5 does not suffice to distinguish between energetic higher states which are nearly not populated and energetic lower states with a higher transition energy but smaller transition dipole moment. However, it seems rather unlikely that there are populated, energetic lower states which cannot be excited. Beside this explanation another reason for the signal can be discussed. According to the information available so far (cf. [86, 90]) it can be assumed that additional signals shifted only a few wavenumbers to the blue side might be attributed to isotope signals caused by the fact that most of the elements are composed of more than one isotope[3]. In case of phthalocyanine it has to be considered that the $^{12}\mathrm{C}$ atoms can be substituted by a $^{13}\mathrm{C}$ isotope. As described in [86] the $0.6\ \mathrm{cm}^{-1}$ blue-shifted signal can be assigned to an isotope signal where one $^{12}\mathrm{C}$ is replaced by one $^{13}\mathrm{C}$. The results found for the intensity ratio between ZPL and the resonance at $15089.5\ \mathrm{cm}^{-1}$ of nearly 5 % as well as the equal width of both peaks (cf. tab. 4.1) support this presumption.

---

[3] variants of a chemical element which differ only in their number of neutrons

In addition, the dispersed emission revealed these two peaks as two different systems [86]. According to this assumption it seems quite reasonable to explain the signals around 15089.1 cm^{-1} by an excitation of phthalocyanine molecules where two ^{12}C atoms are replaced by ^{13}C. This probability $P(2)$ = 4 % can be calculated and must be divided by 4[4] to determine the expected intensity ratio. The structure of this signal (cf. Fig. 4.4) could indicate different places for the second ^{12}C compared to the first one. However, the different saturation behavior of the ZPL and this signal as well as its fine structure and the asymmetric tail of the ZPL do not allow to compare their intensities with the ZPL. In general, both discussed phenomena, solvation complexes as well as isotope signals, would be considered to exhibit only very small intensities. The different saturation behavior and the line shape as well as the missing asymmetric blue tail would support the assumption of different Pc helium complexes, whereas the small energy gap points to an isotope signal. Moreover, it cannot be excluded that the signal consists of both phenomena. So far, it has not been possible to reach a definitive conclusion to this question.

The predominant view propounded in literature is that ZPL and PW can be distinguished by their different saturation behavior and thus, the signals shown in Fig. 4.5 (b) represent the spectral signature of the phonon wing (PW) [4, 86, 88]. These signals were also scaled to the maximum of the ZPL and obviously they exhibit a different saturation behavior than the ZPL and the signals discussed above. The spectral width of the two panels (a) and (b) is equal. First, the intensities of the resonances between 15091.8 cm^{-1} and 1593.7 cm^{-1} have been analyzed. These values are plotted in figure 4.7 (non-filled symbols) and the functions $\cos(\alpha)$, $\cos^2(\alpha)$ and $\cos^4(\alpha)$ are added. The data points at 90° do not reach full attenuation because of the limitation by the quality of the polarizer. Apart from the data points at $\cos^2(\alpha)$=0.46 (α = 47°) the intensities of the resonances appear slightly below

---

[4] By neglecting the impact of the two H atoms in the center of phthalocyanine the 32 C atoms can be split into 4 groups of 8 equivalent C atoms [86].

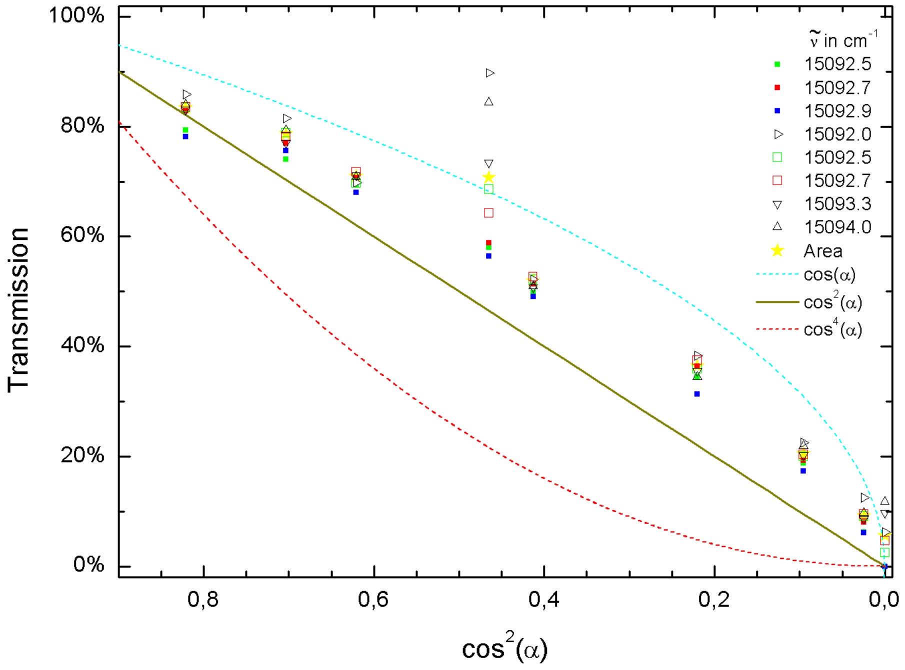

Fig. 4.7: Amplitude of the fitted peaks (filled squares), signal intensities at different frequencies (non-filled triangles and squares) as well as the area under the curve (yellow stars) are plotted for different polarizer adjustments. Additionally the functions cos(α), $\cos^2(\alpha)$ and $\cos^4(\alpha)$ are mapped in the diagram. The frequencies $\tilde{\nu}$ are listed in the legend of the plot.

or above the graph of $\cos^2(\alpha)$. This function is a measure for the attenuation of the laser light by the polarizer and thus, the LIF signal should be identical to this function as long as the transition is not saturated. Figure 4.8 shows the absolute deviation of the measured values from the calculated ones. In both figures the fitted amplitudes of the most intense resonance of the phonon wing were added. For this purpose the signals at $\tilde{\nu} = 15092.5\ \mathrm{cm}^{-1}$ (green ■), $\tilde{\nu} = 15092.7\ \mathrm{cm}^{-1}$ (red ■) and $\tilde{\nu} = 15092.9\ \mathrm{cm}^{-1}$ (blue ■) in each spectrum were analyzed and could be simulated best with Gaussian functions (cf. Fig. 4.4 bold Gaussian curves). Therefore the width as well as the frequency $\tilde{\nu}$ were kept fixed (cf. tab. 4.1) and only the ampli-

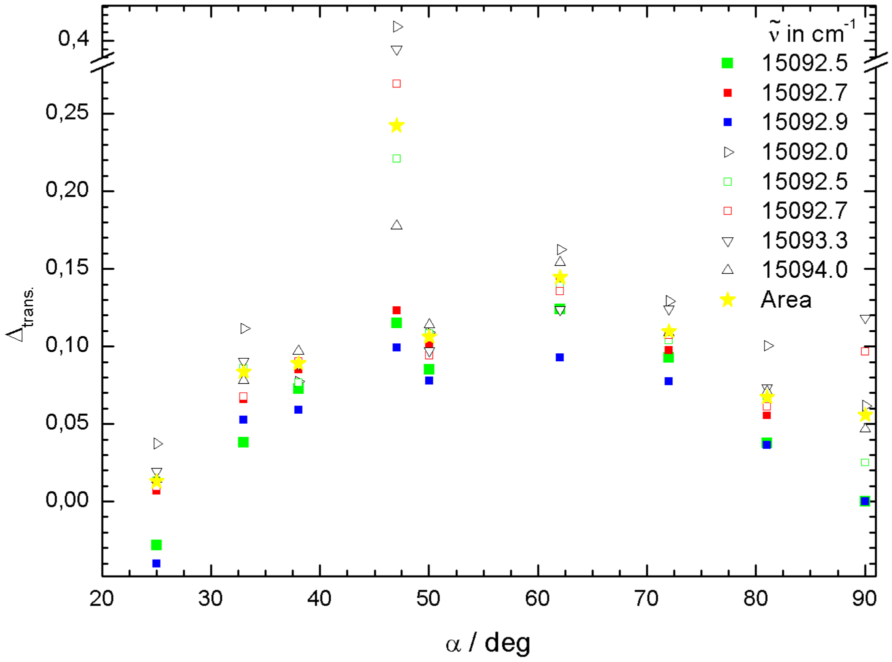

Fig. 4.8: Δ_{trans} shows the difference between the measured data points and the corresponding calculated $\cos^2(\alpha)$ function values.

tude was the fitted variable. In these fits the offset which results out of the blue tail of the ZPL was taken into account. By weakening the laser power (as it can be seen in figure 4.7) the squares largely coincide with the corresponding squares of the other peaks as well as with the decrease of the intensities (non-filled symbols). The variation of these signals for a given polarizer position is possibly caused by the limited accuracy of the Gaussian fits as well as limitations in the experimental accuracy in particular for the reading of the polarizer angle. On account of the experimental setup it was not possible to determine the exact value of the angle, so the values do not match exactly to the $\cos^2(\alpha)$ function. The inaccuracy of the experiment was found to be up to 7°. Nevertheless, one can clearly see that the experimental data fit best to the $\cos^2(\alpha)$ function. Taking a closer look at figure 4.8 showing the difference between each data point and the corresponding $\cos^2(\alpha)$

function value one can notice that there is a deviation from the function values. In case of high laser intensity (ca. 25 °) as well as low intensity (ca. 80 °) these values are smaller compared to the region between 35 ° and 80 °. Moreover, the data sets appear in a similar order. This is indicative for systematic errors and might be attributed to the slight movement of the beam axis caused by the refraction of the laser light by the polarizer. The yellow stars ($\star$) represent the integrated area under the curve between 15091.5 cm^{-1} and 15094.5 cm^{-1} for each polarizer position. The stars also largely coincide with the other data. The only clear expection from the $\cos^2(\alpha)$ function was found at the data points at 47 °, which were observed to be significantly higher. Taking a closer look at this data set in figure 4.8 one can see that the non-filled symbols as well as the star are shifted to higher values, whereas the filled squares are consistent with the other data. This individual deviation most probably reflects a systematic error for this particular spectrum which can easily be caused by fluctuations of helium droplet source conditions or laser conditions. The relative deviation between the filled squares (fitted amplitudes) and the other higher lying values (cf. Fig. 4.8) is thought to be caused by the blue tail of the ZPL. This signal was included into the fit. Thus, the background signal only affects the abso-

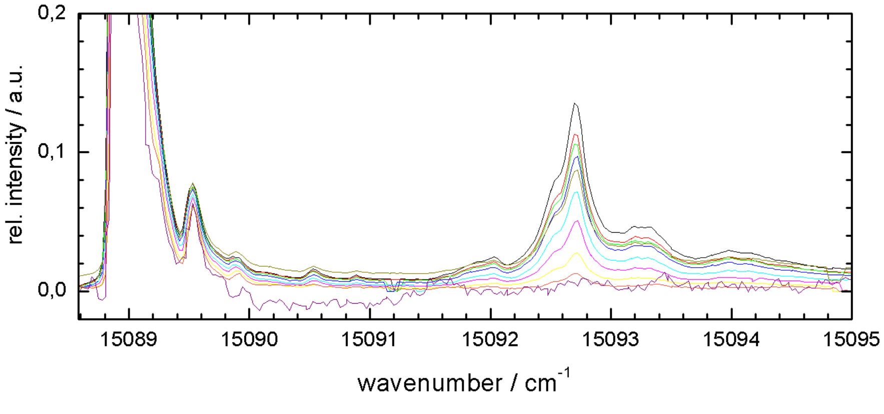

Fig. 4.9: LIF signals of Pc inside superfluid helium droplets ($\bar{N} \approx 20000$ atoms) for different laser intensities. Each spectrum has been normalized to its ZPL at $\tilde{\nu}_0 = 15088.9\,\mathrm{cm}^{-1}$. The purple curve was shifted by one step to the red side.

lute intensities as well as the integrated areas, whereas the fitted amplitudes (filled squares) are not affected. It can be confirmed that the signals between 15091.8 cm^{-1} and 15093.7 cm^{-1} show the same saturation behavior which is clearly different than the saturation of the electronic origin at 15088.9 cm^{-1}. This can be seen in figure 4.9 showing different spectra normalized to each maximum in the frequency range of the ZPL plus nearly 7 cm^{-1}. The intensities of the ZPL (enlarged area) as well as the ZPL of the isotope variant of Pc do not change, whereas the intensity of the blue-shifted structured signal vanishes. Thus, both signals are still saturated while the blue-shifted transitions cannot be detected anymore.

4.2.3 Dependence of ZPL and PW on the Mean Droplet Size

In order to collect further evidence for an assignment of ZPL and PW, another spectroscopic detail that provides information on the microscopic situation of the probe has been examined. It is known that the line shape and the position of the ZPL depends on the number of attached rare gase molecules [13, 84, 86, 95] (cf. chapter 2.3.2). In this regard, the line shape of the PW was analyzed at different droplet sizes and compared with the line shape at the electronic origin. Figure 4.10 shows the zero phonon line of phthalocyanine recorded for different mean droplet sizes between 25000 and 12000 helium atoms (64 nm - 50 nm; cf. chapter 2.2.1). Each spectrum has been normalized to its respective intensity maximum. It can be clearly seen that the onset of the ZPL is not affected whereas the steep rise on the red side and the blue asymmetric tail of the peak change by rising the nozzle temperature T_0 up to 12 K. Comparing the results of this experiment (T_0 from 10.5 K up to 12.0 K) one recognizes that the red edge of the peak becomes slightly flatter. At a temperature of 9.5 K the expansion is close to the transition from the sub-critical to the super-critical region, which causes a dramatic change in the droplet size distribution. The super-critical helium expansion leads to droplet sizes up to 10^6 helium atoms. This growth goes at the expense of the number of droplets, which is reflected by a reduced S/N. The data recorded at a temperature

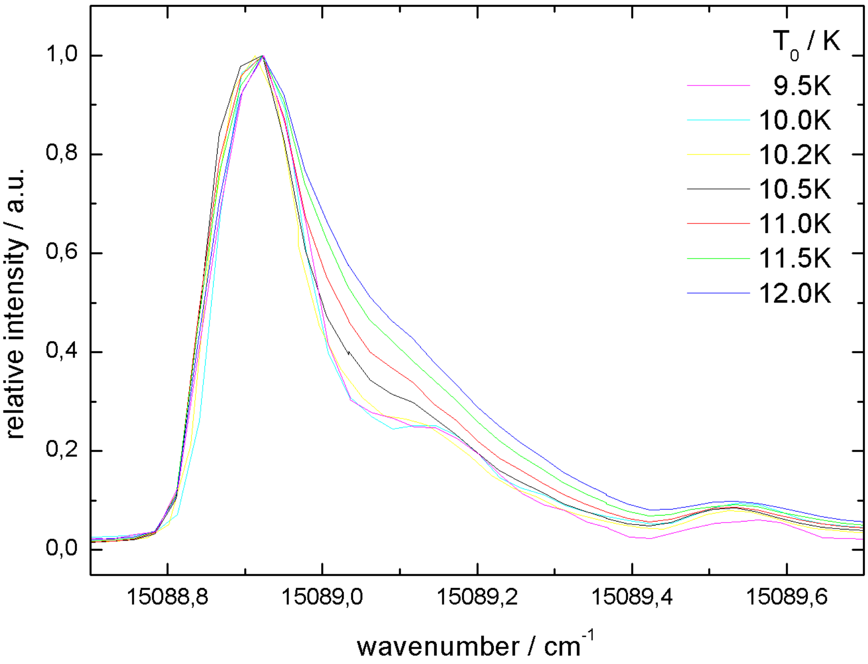

Fig. 4.10: Signal of the ZPL observed at various nozzle temperatures $9.5\,\mathrm{K} \leq \mathrm{T}_0 \leq 12.0\,\mathrm{K}$ and a stagnation pressure $\mathrm{p}_0 = 20$ bar ($25 \cdot 10^3 \leq \bar{N} \leq 12 \cdot 10^3$). The data has been normalized to each maximum of the spectra.

of 10.0 K and 10.2 K must also be critically reviewed because the error here was increased by the temperature controlling unit working at the borders between two heating powers, which leads to a significantly higher noise in T_0 and thus, to a higher fluctuation in the mean droplet size distribution. Moreover, the temperature fluctuations may cause variations between sub-critical and super-critical expansion conditions, which is accompanied by dramatic variations in the number of singly doped droplets and the corresponding spectral shape. The blue tail of the peak reveals that the inhomogeneous line broadening of the peak rises with T_0 and the additional signal at 15089.1 cm^{-1} cannot be resolved anymore. The asymmetric tail of the electronic origin can be attributed to an inhomogeneous line broadening effect caused by the log-normal droplet size distribution. The helium droplet environment can be treated classically as a polarizable environment of the Pc-chromophore. Such an environment causes a red shift in the electronic transition frequency. With an increasing radius of the environment the red shift converges to a limiting value which is the bulk value. This model has been applied in Refs. [95] and [13] to simulate the asymmetric line shape. It could be inverted so that the asymmetry could be used to determine the droplet size distribution. However, the experimental spectra presented in Refs. [95] and [13] lack a reasonable S/N ratio. Therefore, the line shape analysis for new spectra was repeated with significantly improved S/N.

The same examination has been performed for the signal of the phonon wing. The signals have been normalized after the background signal was subtracted. These results can be found in figure 4.11. At T_0 = 9.5 K only a weak LIF signal could be observed. Nevertheless, the purple graph still provides a good picture of the fine structure despite the bad signal-to-noise-ratio. The reason for this weak signal was already visible in the data of the ZPL, which was nearly two orders of magnitude less intense than the most intense electronic origin ($\bar{N} \approx 20000$ He atoms) and thus, the signal-to-noise-ratio increases.

Looking now at the change of the line shape of the most intensive peak of the PW signal, one can see that the signal becomes only slightly broader when the nozzle temperature is raised from 10.5 K up to 12.0 K. It is obvious that this change similarly affects the whole signal. Due to the fact that these spectra consist of two signals, the broad tail of the ZPL as well as the contribution of the PW, the normalization to the maxiumum of the PW at 1592.7 cm^{-1} affects the PW signal and the tail of the ZPL differently. The change of the signal shown in figure 4.11 can be attributed to this normalization. Thus, the asymmetric line broadening found at the blue tail of the ZPL cannot be observed at the maximum of the PW. The two experiments recorded at T_0 = 10.0 K and T_0 = 10.2 K revealed nearly identical signals showing a slightly smaller line broadening than detected at T_0 = 10.5 K. At T_0 = 9.5 K (purple curve) only a weak signal remains but the fine structure of the PW can still be resolved. The line width of this resonance seems to be broader than

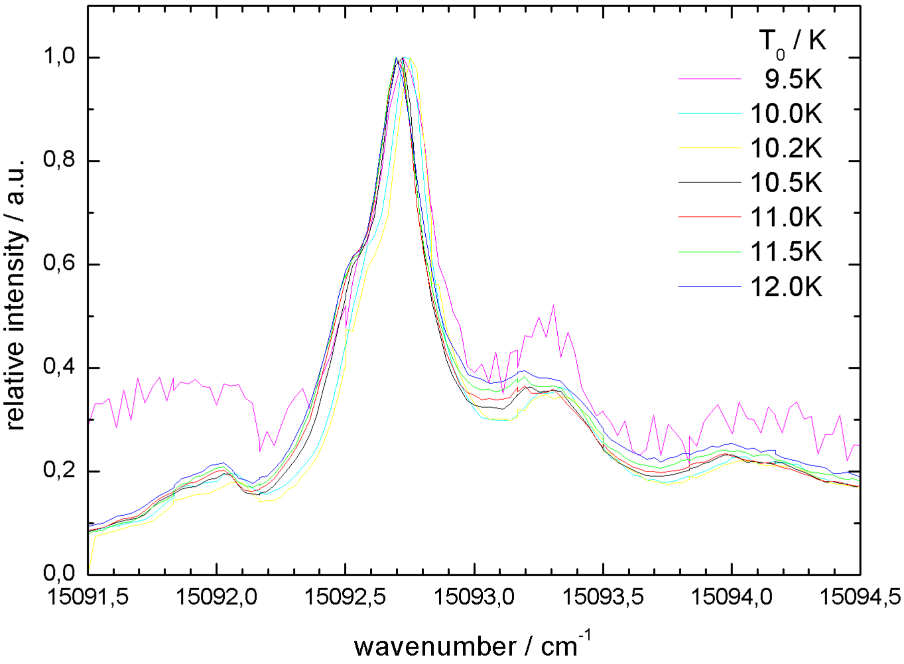

Fig. 4.11: Signal of the PW observed at various nozzle temperatures 9.5 K ≤ T_0 ≤ 12.0 K and a stagnation pressure p_0 = 20 bar ($25 \cdot 10^3 \leq \bar{N} \leq 12 \cdot 10^3$). The data has been normalized to the maximum of each spectrum after the background signal was subtracted.

the other signals. The weak signal might be due to the sub-critical helium expansion and thus, an enormous increase of the mean droplet size. However, because of the bad signal-to-noise-ratio in this spectrum and the background correction it was not possible to determine the change in the width of this signal.

Due to a comparison of the spectral position of the maximum in each recorded spectrum (Fig. 4.11) it can be seen that there is no shift between 10.5 K and 12.0 K. Figure 4.12 demonstrates that the two spectra recorded at 10.0 K and 10.2 K seem to be shifted by only one (10.0 K) and two (10.2 K) data points to the blue. The absolute spectral position of the maximum of the PW in the purple curve (9.5 K) is also shifted only one data point to the blue. The frequency step width in these

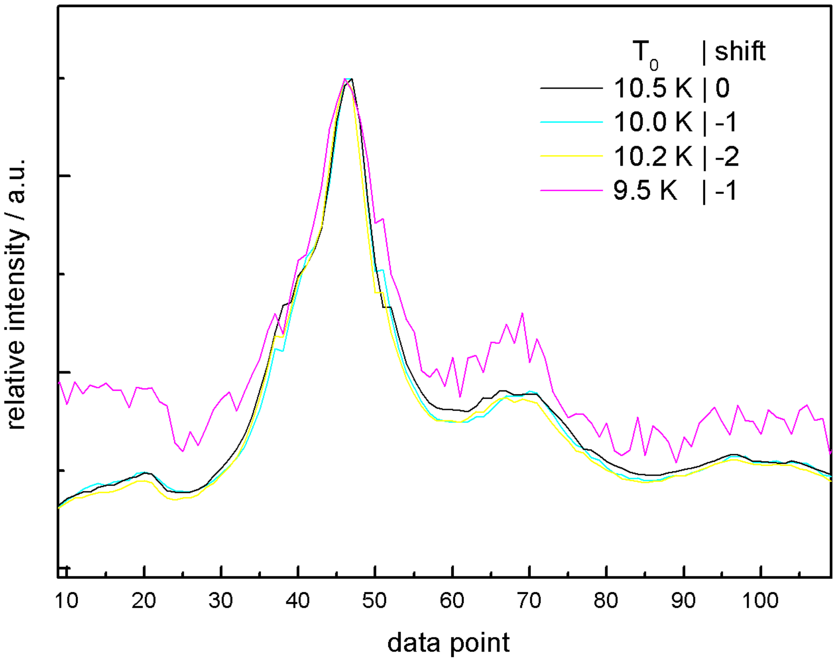

Fig. 4.12: Signal of the PW observed at various nozzle temperatures and a stagnation pressure $p_0 = 20$ bar $(25 \cdot 10^3 \leq \bar{N} \leq 12 \cdot 10^3)$. The data has been normalized to the maximum of each spectrum after the background signal was subtracted. The curves have been shifted by one and two data points.

experiments was 300 MHz, which means that the shift of the signals is only 0.01 cm^{-1} and 0.02 cm^{-1}. This is in the order of the absolute measurement accuracy of the laser frequency. Thus, these experiments revealed that the spectral position of the most intense resonance of the PW remains unchanged by the variation of the mean droplet size distribution of the helium droplets. This result can be transferred to the other signals detected in the frequency window between $\tilde{\nu} = 15091.5$ cm^{-1} and $\tilde{\nu} = 15095.0$ cm^{-1}. Thus, the blue shift observed at the ZPL for different T_0, which is accompanied by the asymmetric line broadening, could not be found for this spectral structure. Moreover, it can be noted that the change of the signals is a result of the asymmetric line broadening of the blue tail of the ZPL.

4.2.4 Dispersed Emission

In addition to LIF spectroscopy, the dispersed analysis of emitted light offers an important spectroscopic tool for the examination of photo physical effects. The first emission spectra of phthalocyanine embedded in superfluid ^{4}helium droplets were published in [105] in 2003 and show the emission of free-base phthalocyanine and magnesium phthalocyanine. One of the most striking results of these experiments was the observation of a second red-shifted emission spectrum (SES)[5] in addition to the normal first emission spectrum (FES) for both molecules. This doubling does not occur in the excitation spectrum nor can it be found in the gas phase experiment. All the spectroscopic features observed for the dual emission of these two Pc-compounds in helium droplets could be explained by assuming a dopant-helium solvation complex which exhibits different configurations which partly relax upon electronic excitation [105]. Pump-probe experiments of phthalocyanine inside helium droplets [99, 106] supported this assumption. To obtain more details which may help to distinguish between signals of the phonons and those of pure electronic transitions the dispersed emission spectra of phthalocyanine have been examined in this work. As already known, the emission spectra recorded upon excitation at a frequency of $\tilde{\nu}_1 = 15088.9\,\text{cm}^{-1}$ and $\tilde{\nu}_2 = 15092.7\ \text{cm}^{-1}$ coincide [141]. This observation was interpreted as evidence for a dissipation of the phonon energy into the helium droplet before the emission takes place [104, 105, 107]. Thus, the signals monitored after excitation at both frequencies $\tilde{\nu}_1$ and $\tilde{\nu}_2$ can be assigned to different transitions of the same electronic system or at least to systems that have to be linked to each other. This situation is identical to the dissipation of the vibrational energy prior to radiative decay of an initial vibronically excited dopant molecule [3, 4]. Figure 4.13 shows the dispersed emission of phthalocyanine inside helium droplets excited at a frequency $\tilde{\nu}_{\text{ex}} = 15217.0\,\text{cm}^{-1}$. This spectrum as well as all other emission spectra were transformed from intensities measured as function of the wavelength. It shows one intense and sharp transition followed by a series of similarly sharp

---

[5] SES and FES stands for Second and First Emission Spectrum.

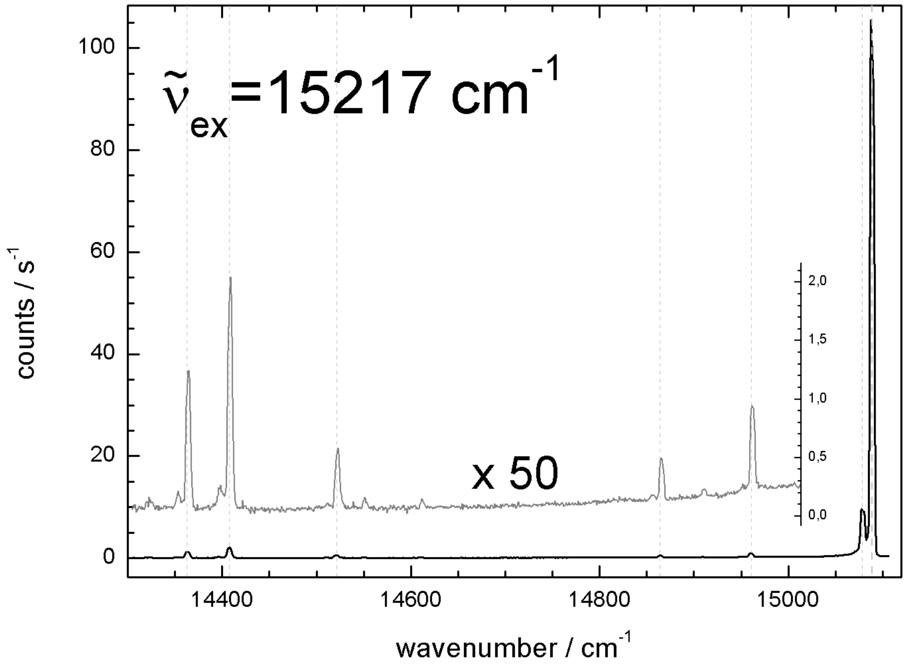

Fig. 4.13: Dispersed emission spectrum of phthalocyanine inside helium droplets ($\bar{N} \approx 20.000$ helium atoms). The spectrum was recorded at the laser frequency $\tilde{\nu}_{\mathrm{ex}} = 15217.0\ \mathrm{cm}^{-1}$. The dashed lines mark the vibronic transitions of the ground state as well as the origin of the second emission spectrum. For a better visualization the height scale of the grey graph was magnified by a factor of 50.

transitions with roughly two orders of magnitude lower intensities. The width of all emission signals in the experiment was determined by the spectral resolution of the detection unit. At $\tilde{\nu} = 15088.7\,\mathrm{cm}^{-1}$ the most intense peak is assigned to the pure electronic transition between the first excited state S_1 and the ground state S_0 (FES). The second signal $\tilde{\nu} = 15078.3\,\mathrm{cm}^{-1}$ is $10.4\,\mathrm{cm}^{-1}$ shifted to the red and was interpreted as an electronic origin (SES) of the emission of a chromophore surrounded by a helium solvation layer with different configuration and/or a different number of helium atoms of the helium solvation layer forming a local minimum structure on the potential energy surface in addition to the global minimum of the helium phthalocyanine interaction [105]. The intensity ratio between these two spectra changes continuously with the excess excitation energy [106]. A look at the enlarged grey curve in figure 4.13 reveals five other narrow signals. Their intensities are about two orders of magnitude smaller than the electronic origin. These signals represent different vibrational modes of the electronic ground state. Comparing each of these signals with the electronic origin shows that they are also followed by a much less intense, red-shifted sharp signal. Within the experimental accuracy the red shift was determined to be around 10.8 cm^{-1}. These additional signals can also be assigned to the second emission spectrum of phthalocyanine [86] and thus, they represent vibronic modes of a metastable solvation configuration of Pc-He_N cluster in the ground state. A comparison of $\Delta\tilde{\nu}$ and the red shift of the SES reveals that the rearrangement of the helium around the molecule has basically no influence on the vibrational frequencies of the Pc molecule. The model which explains the second emission spectrum is based on the assumption that electronic excitation causes a change of the configuration of the dopant-helium solvation complex from a global minimum configuration into a local minimum, which partly relaxes into a global minimum. The relaxation is driven by the amount of excess excitation energy [86]. For the purpose of this study, many emission spectra at different frequencies $\tilde{\nu}_{\mathrm{ex}}$ were taken and compared with the data shown in figure 4.13.

The proposed explanation for the dual emission of Pc in helium droplets suggests that the efficiency of the relaxation might be drastically enhanced by exciting the helium solvation layer which is equal to an excitation at the PW. It was shown for the example of Mg-Pc and for a Pc-Ar cluster that upon excitation at the PW the red-shifted emission and, thus, the relaxation probability exceeds by far the expectation with respect to the corresponding excess excitation energy [104]. Thus, in case of a PW excitation one expects a significant increase of the red-shifted emission compared to the recorded data for vibrational excess energy (cf. Ref. [105]). To check this assumption the dispersed emission signals of phthalocyanine were recorded after

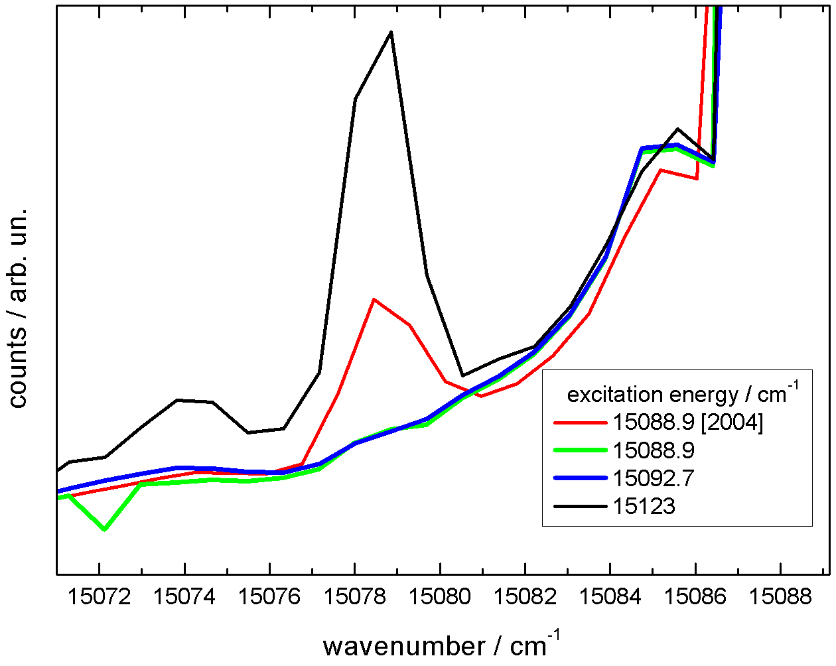

Fig. 4.14: Dispersed emission spectra of phthalocyanine inside helium droplets ($\bar{N} \approx 20.000$ helium atoms) around the origin of the SES. The molecule was excited at the electronic origin $\tilde{\nu}_{\mathrm{ex}}$ = 15088.9 cm^{-1} (green), the most intense signal of the phonon wing $\tilde{\nu}_{\mathrm{ex}}$ = 15092.7 cm^{-1}(blue) and off-resonantly at $\tilde{\nu}_{\mathrm{ex}}$ = 15123 cm^{-1} (black). The red spectrum was taken from [86].

excitation at the PW and compared to the emission signal of the electronic origin excited at $\tilde{\nu}_{\mathrm{ex}}$ = 15088.9 cm^{-1}. The intensity of the SES should be already 1.4 % of the FES after excitation at the electronic origin [107] and is supposed to rise with the excess energy [105]. Figure 4.14 shows the emission of phthalocyanine around the origin of the SES after excitation at $\tilde{\nu}_{\mathrm{ex}}$ = 15088.9 cm^{-1} (green), the most intense signal of the phonon wing $\tilde{\nu}_{\mathrm{ex}}$ = 15092.7 cm^{-1} (blue) and far away from a vibronic resonance with an excess energy of 34.1 cm^{-1} ($\tilde{\nu}_{\mathrm{ex}}$ = 15123 cm^{-1} black). Additionally, the red graph was added, showing the emission at the electronic origin (taken from [86]). All signals were scaled to the vibrational modes of the FES which are not shown in the plotted section of figure 4.14. By a comparison of the different spectra at the origin of the SES ($\tilde{\nu}_0$ = 15078.3 cm^{-1}) it is obvious that the most intense SES can be found after the excitation with the highest excess energy (black) compared to the pure electronic transition. This matches the results published in [105]. Beyond, it can be seen that the blue and the green curves do not differ significantly. Accordingly, no unexpected increase of the intensity of the SES can be found between the pure electronic excitation and the excitation at the PW, which means an excess energy of only 3.8 cm^{-1}, but an additional excitation of the surrounded helium atoms. If the assignment of the PW is correct, then the SES seems not to be enhanced dramatically upon the excitation of the helium solvation layer. Since this observation contradicts the expectations, it questions the assignment of this spectroscopic signature and might be an indication of zero phonon lines of different Pc helium complexes instead of phonon excitation.

For both emission spectra (blue and green, Fig. 4.14), the intensity of the SES lies well below the 1.4 % which is indicated by the red graph in figure 4.14. This result was reproducible and thus, the emission signal after excitation at the electronic origin differs from the observed emission published in [86, 105]. Since the same system was examined, this difference might be due to the instrumental differences between the two experiments, which mainly relates to the optical detection unit imaging the fluorescence onto the entrance slit of the spectrograph as well as the coupling of the laser light to the experiment. Nevertheless, both should not affect the relative intensities of the FES and the SES. On this account, it might be legitimately assumed that the value of 1.4 % has to be corrected. This statement is also supported by the fact that the intensity ratios detected after excitation at the vibronic transitions of Pc are consistent with the results obtained in [86, 105]. Consequently, no additional red-shifted signals could be resolved next to the vibronic modes of the FES after excitation at a frequency of $\tilde{\nu}_{\mathrm{ex}}$ = 15092.7 cm^{-1}. This frequency coincides with the maximum of the spectral structure shown in Fig. 4.4 / 4.5 b which is identified with the phonon band of Pc inside helium droplets. Figure 4.15 shows the detected

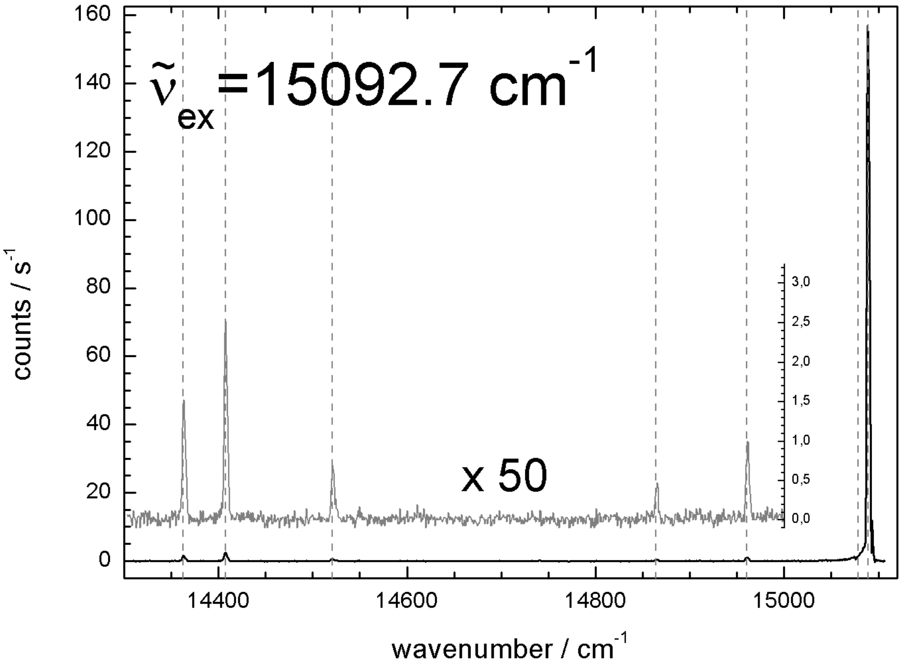

Fig. 4.15: Dispersed emission spectrum of phthalocyanine inside helium droplets ($\bar{N} \approx 20.000$ helium atoms). The spectrum was recorded at a laser frequency $\tilde{\nu}_{\text{ex}}$ = 15092.7 cm^{-1}. The dashed lines mark the vibronic transitions of the ground state as well as the origin of the second emission spectrum. For a better visualization the height scale of the grey graph was magnified by a factor of 50.

emission signal between 14300 cm^{-1} and 15100 cm^{-1}, which is quite similar to the data shown in figure 4.13 apart from the signals of the SES.

The experiment showed that the relaxation probability between FES and SES seems to be identical after excitation at $\tilde{\nu}_{\text{ex}}$ = 15092.7 cm^{-1} and excitation at the electronic origin. This observation does not confirm our expectation on the influence of phonons on the transition probability and allows for reasonable doubts with respect to the assignment of the phonon wing. However, the absence of the SES after excitation at the ZPL as well as at $\tilde{\nu}_{\text{ex}}$ = 15092.7 cm^{-1} represents a considerable problem for the distinction between the ZPL of different solvation complexes and the PW. Finally, also an enhanced relaxation probability would not be sufficient to prove a phonon excitation or a transition of a different helium solvation complex. The emission spectrum excited at $\tilde{\nu}_{\mathrm{ex}} = 15093.3\ \mathrm{cm}^{-1}$ reveals the same result and leads to an identical interpretation.

4.2.5 Van der Waals Complexes of Phthalocyanine Argon

The data of the next examinations should prove or refute previous results which were interpreted as a helium promoted dissociation dynamics of a Pc-Ar_1 van der Waal cluster which was published in [86, 141]. Gas phase experiments revealed that an excess energy of at least 661 cm^{-1} is required for a vibrational predissociation [142]. Upon electronic excitation of the Pc-Ar_1 cluster inside helium droplets the dispersed emission of the cluster was accompanied by the emission of bare Pc. This observation was explained by the dissociation of few of the excited clusters prior to radiative decay. Only 1/6 of the known dissociation energy of the free Pc-Ar cluster was sufficient for dissociation inside a helium droplet. Moreover, the intensity of the origin of bare Pc implied that the fraction of dissociation did not correlate to the excess excitation energy. Both these observations are rather remarkable and ask for further examination. Since the conductors of this previous study did not excite resonantly to the bare phthalocyanine-helium complex, they came to the result that the Pc-Ar bond breaks and thus, a dissociation of the excited Pc-Ar_1 complex must have taken place before the excited state decays radiatively. A simple proof of the proposed explanation would be the investigation of the emission of bare Pc upon excitation at the known resonances of the Pc-Ar cluster. Thus, the experiments done for the Pc-Ar cluster have been repeated with the simple modification that no Ar was provided at all. According to the conclusions outlined in Ref. [141] this new experiment should not show any signal neither in excitation nor in emission. Figure 4.16 shows the dispersed emission of phthalocyanine inside helium droplets after an excitation at the frequency of the 128.1 cm^{-1} vibrational mode of the Pc-

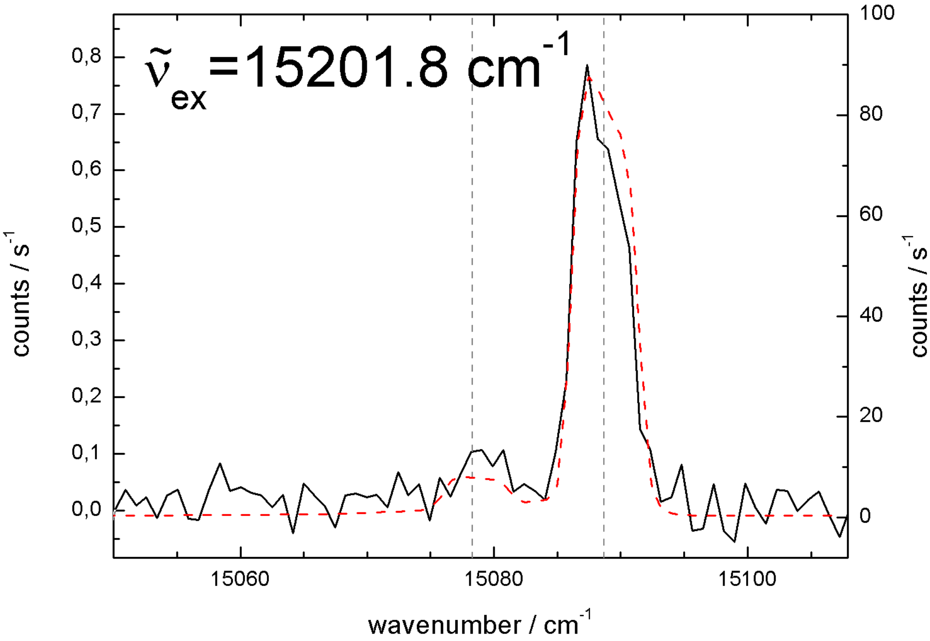

Fig. 4.16: Dispersed emission spectrum of phthalocyanine inside helium droplets ($\bar{N} \approx 20.000$ helium atoms). The spectrum was recorded at a laser frequency $\tilde{\nu}_{ex}$ = 15201.8 cm^{-1} which is coincident with the excitation energy of the 128.1 cm^{-1} vibrational mode of the Pc-Ar$_1$ cluster. The dashed lines mark the origin of the first and second emission spectrum. The dashed graph shows the emission after the excitation of the 128.1 cm^{-1} vibrational mode of bare Pc ($\tilde{\nu}_{ex}$ = 15217 cm^{-1}).

Ar$_1$ cluster ($\tilde{\nu}_{ex}$ = 15201.8 cm^{-1}). The emission was corrected with respect to the background signal, thus, scattered laser light as well as thermic noise of the CCD chip does not affect the data. The dotted curve shows the emission signal of bare Pc after excitation at the 128.1 cm^{-1} vibrational mode of Pc ($\tilde{\nu}_{ex}$ = 15217.0 cm^{-1}). The dashed lines mark the origin of the first and second emission spectrum. Contrary to the expectations figure 4.16 reveals two weak signals at the frequencies $\tilde{\nu}_1$ = 15088.7 cm^{-1} and $\tilde{\nu}_2$ = 15078.3 cm^{-1}. The absence of a signal at the origin of Pc-Ar$_1$ ($\tilde{\nu}_1$ = 15073.7 cm^{-1}) shows that no Pc-Ar clusters were excited. The observed

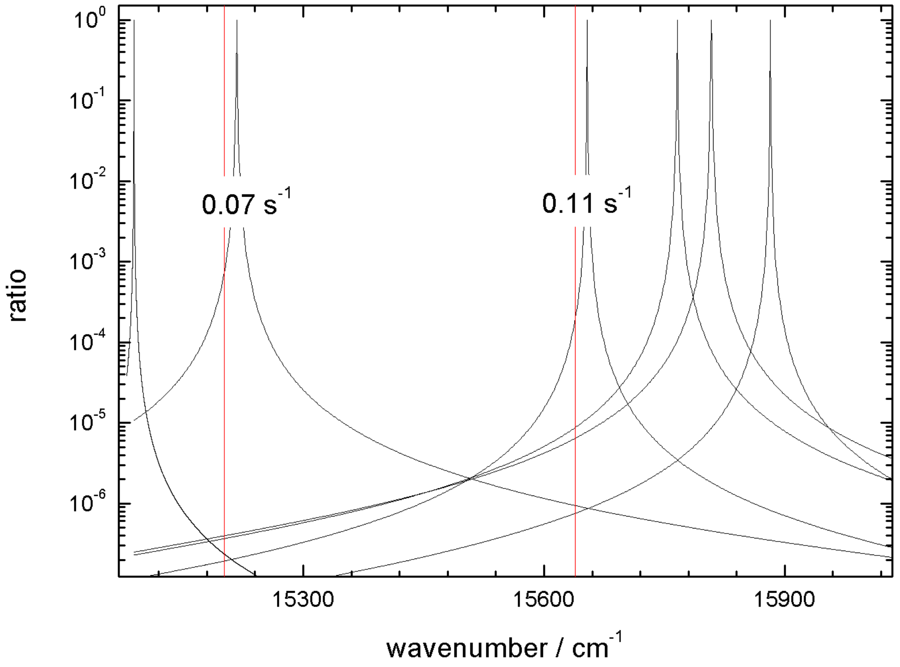

Fig. 4.17: Normalized Lorentzian curves of the intense vibronic transitions in the LIF spectrum of Pc inside helium droplets. The values for the width have been taken from [86]. The red lines mark the excitation frequencies of the Pc-Ar_1 clusters at $\tilde{\nu}_{\mathrm{ex}} = 15201.8\ \mathrm{cm}^{-1}$ and $\tilde{\nu}_{\mathrm{ex}} = 15638.6\ \mathrm{cm}^{-1}$.

frequencies are coincident with the electronic origin of the first and second emission spectrum of bare phthalocyanine inside helium droplets. Moreover, it can be seen that the intensity of the signals is lowered by two orders of magnitude compared to the emission signal recorded upon excitation in resonance with the 128.1 cm^{-1} vibrational mode of bare Pc (cf. dashed line in Fig. 4.16). Nevertheless, looking at the intensities shows that this emission is not only a consequence of the excitation in the tail of the vibronic transitions of bare Pc. As it can be seen in figure 4.17, such an excitation would only lead to a signal of $7.8 \cdot 10^{-4}$ times the emission of the 128.1 cm^{-1} vibrational excitation, which would mean an emission of only 0.07 counts per second. The contributions of the electronic origin as well as of the other vibrational signals would be less than 0.001 counts per second and thus, they are negligible. The parameter of the Lorentzian curves were taken from [86]. Furthermore, comparing the two graphs in figure 4.16 reveals that the ratio between the origin of the FES and SES is different than the ratio extracted out of the data excited at the vibronic mode (cf. Fig. 4.16, dotted curve). The relative intensity $\frac{I_{SES}}{I_{FES}+I_{SES}}$ reveals a value between 13 % and 15 % at $\tilde{\nu}_{\mathrm{ex}}$ = 15201.8 cm^{-1} and thus, differs from the value 6.5 % [141] / 7.7 % (cf. Tab. 4.2) found after the excitation of the pure molecular transition at 15217.0 cm^{-1}. This change would support the assumption that phonon excitations promote the rearrangement of the helium solvation layer. Anyway, since the emission signal after excitation in the region of the phonon wing showed nearly no SES (cf. Fig. 4.14), the difference shown in Fig. 4.16 might be caused by the weak signal-noise-ratio. Nevertheless, bare Pc solvated in a helium droplet also absorbs at the resonance frequency of Pc-Ar which is about 15 cm^{-1} off the closest vibronic resonance. Thus, the signal previously explained as a result of photodissociation of the cluster originates from bare Pc and thus, does not reveal a helium modified dissociation mechanism of the cluster. At the present signal level vibronic transitions remain below the noise level in the emission spectrum (cf. Fig. 4.16).

The same data has been taken at a frequency shifted by 15.2 cm^{-1} to the red side of the vibronic transition $\tilde{\nu}_{\mathrm{vib}}$ = 564.9 cm^{-1} of the phthalocyanine, which coincides with the corresponding vibronic transition of the Pc-Ar cluster. This experiment should also provide more information on the dissociation of the van der Waals bond, which was suggested due to the observation of an emission of bare Pc after the excitation of this vibrational mode of the Pc-Ar$_1$ cluster [141]. The experimental data revealed a similar result as discussed for the $\tilde{\nu}_{\mathrm{ex}}$ = 15201.8 cm^{-1} excitation above. This experiment shows only a weak signal of the dual emission of bare Pc inside helium droplets without any emission signal of the Pc-Ar$_1$ cluster. The data can be found in figure 4.18 together with the emission signal excited at the vibronic transition of Pc ($\tilde{\nu}_{\mathrm{ex}}$ = 15653.8 cm^{-1}). Obviously, the intensity ratio between the two observed signals has been changed in contrast to figure 4.16. The absolute intensity

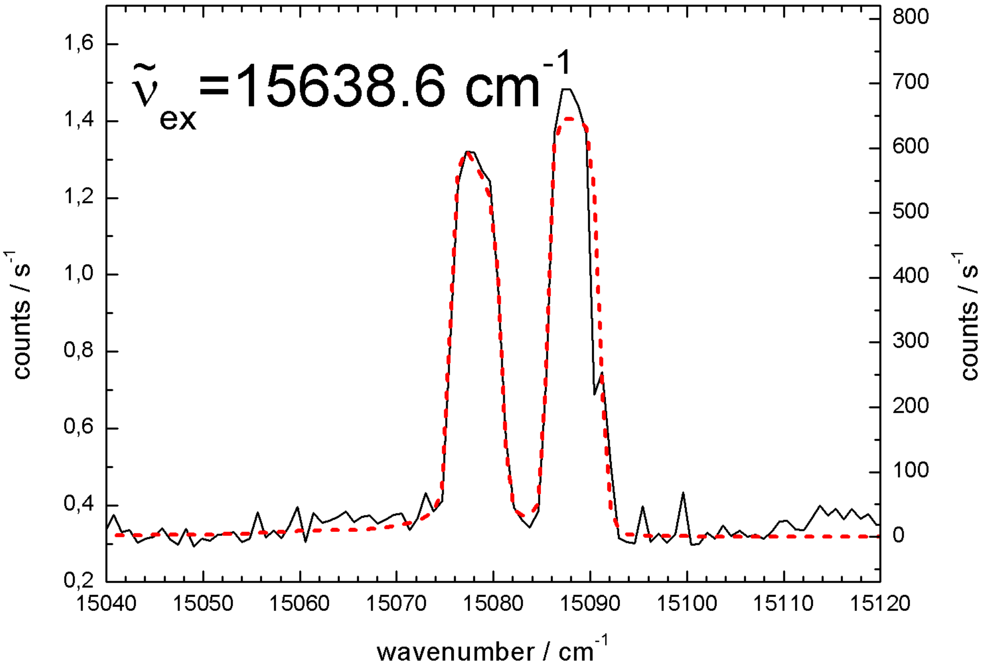

Fig. 4.18: Dispersed emission spectrum of Pc inside helium droplets ($\bar{N} \approx$ 20.000 helium atoms). The spectrum was recorded at a frequency $\tilde{\nu}_{\text{ex}}$ = 15638.6 cm^{-1}. The dashed lines mark the origin of the first and second emission spectrum. The red graph shows the origin of the emission spectrum of phthalocyanine excited resonantly at a frequency of $\tilde{\nu}_{\text{ex}}$ = 15653.8 cm^{-1}. Its intensity refers to the intensity scale on the right side.

of the signal at 15089 cm^{-1} exceeds the signal level which would be expected for the excitation of the tail of the vibronic transitions. In figure 4.17 the value of the expected intensity would be only in the order of 0.11 counts per second and thus, one order of magnitude lower than the observed emission. The intensity of both electronic origins of FES and SES are nearly identical, which is the same than the result found in the emission spectrum upon excitation at the vibronic transition of Pc at the vibrational mode $\tilde{\nu}_{\text{ex}}$ = 15653.8 cm^{-1} (cf. Fig. 4.18 dotted red spectrum). It can be noted that the origin of the SES seems to be slightly less intensive than found after excitation at the vibronic mode. Thus, it seems correct to interpret the higher value of the intensity ratio found at $\tilde{\nu}_{\mathrm{ex}}$ = 15201.8 cm^{-1} or the lower value at $\tilde{\nu}_{\mathrm{ex}}$ = 15217 cm^{-1} (cf. Fig. 4.16) as an experimental outlier. Anyway, the intensity ratio between FES and SES observed after the excitation at 15638.6 cm^{-1} is as expected according to the amount of excess excitation energy [107]. Similar observations could be found in the emission after the excitation shifted 15.2 cm^{-1} to the red side of all other vibronic transitions of Pc. These signals of Pc are independent of Ar.

4.2.6 Off-resonant Excitation of Phthalocyanine

Although the detected emission signals after off-resonant excitation are very weak, the data is reproducible with intensities exceeding the expectations from the tail of a simple Lorentzian line shape as deduced from high resolution excitation spectra [99]. To obtain any indication of the origin of these signals more spectra had been taken. Figure 4.19 shows the recorded data of the emission of phthalocyanine inside superfluid helium droplets excited off-resonantly at different excess energies. The frequency $\tilde{\nu}_{\mathrm{ex}}$ was increased from the top to the bottom panel ((a) → (h)) and is marked in the excitation spectrum shown in figure 4.20. Additionally, the emission signal (red curve) detected after resonant excitation at the vibronic transition $\tilde{\nu}_{\mathrm{ex}}$ = 15638.6 cm^{-1} is shown in panel (a) with its intensity referred to the scale axis on the right side. It should be noted that for all of the spectra presented in Fig. 4.19 the excitation frequency is on the blue side beyond the plotted spectral range. In layer (a) an intense signal can be found at a frequency of $\tilde{\nu}$ = 15089 cm^{-1} which is assigned - due to its frequency - to the origin of the FES of Pc. This signal can be found in each spectrum shown in figure 4.19. When one compares the values of the intensities of the electronic origin in all emission spectra, the extremely weak signal detected at $\tilde{\nu}_{\mathrm{ex}}$ = 15500 cm^{-1} (cf. Fig. 4.19 (d)) is particularly striking. The intensities in panels (a) - (c) are in the same order of magnitude as well as the recorded intensities (f) - (h). Looking at Fig. 4.20 one can recognize that the data can be divided into

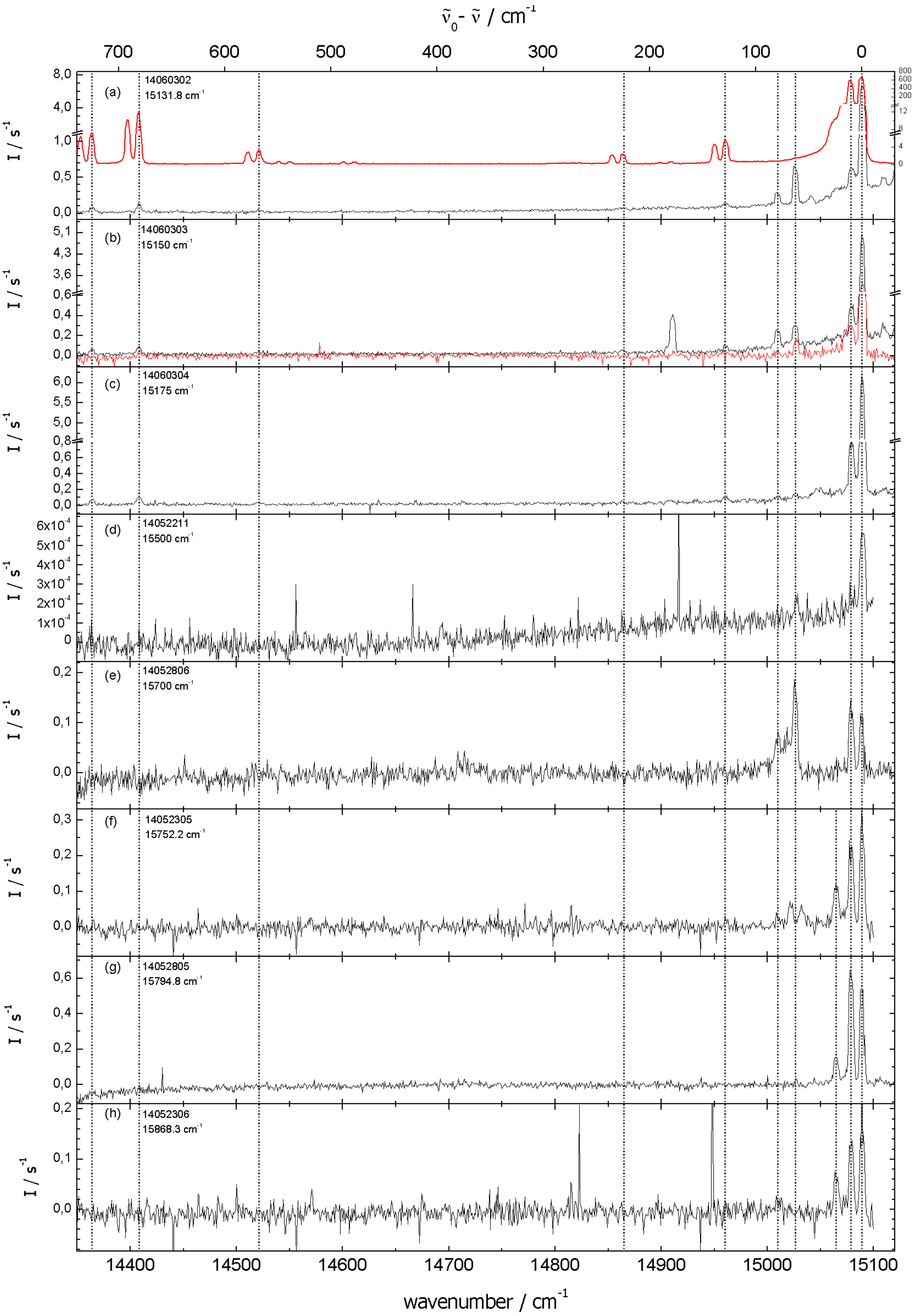

Fig. 4.19: Dispersed emission spectra of phthalocyanine inside helium droplets ($\bar{N} \approx 20.000$ helium atoms). The spectra were recorded at different laser frequencies $\tilde{\nu}_{\mathrm{ex}}$. The frequencies are given in each panel. The energy rises from (a) to (h). Panel (a) also shows the emission after the excitation of the vibronic resonance $\tilde{\nu}_{\mathrm{ex}} = 15638.6\ \mathrm{cm}^{-1}$. Its intensity refers to the scale axis on the right side. The dashed lines are added as an orientation.

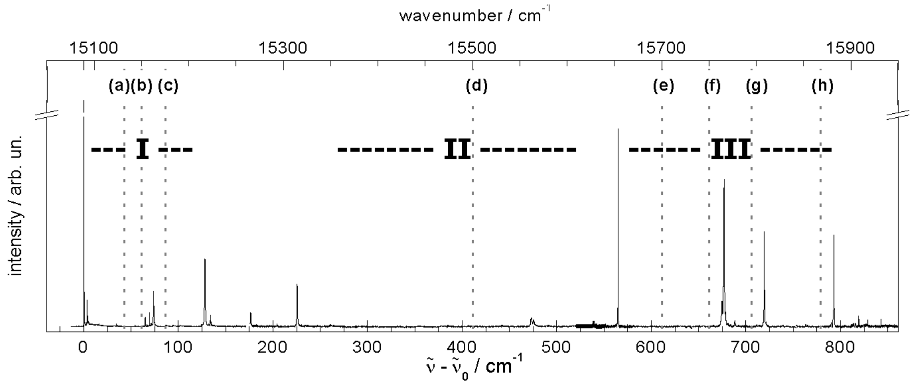

Fig. 4.20: LIF spectra of phthalocyanine inside helium droplets ($\bar{N} \approx 20.000$ helium atoms) taken from [105]. The excitation frequencies used for the data shown in figure 4.19 are marked by grey dotted lines.

three groups: Spectra excited near the electronic origin (I), spectra excited far away from the electronic origin but near intense vibronic modes (III) and finally spectra excited far off any resonance (II). First, the spectra excited in area (I) were analyzed. Since the electronic origin is far more intense than the vibronic transitions, its phonon wing is also more intense than the phonon wing of any vibronic mode. This leads to the assumption that the recorded emission signals in area (I) are caused by the radiative decay of Pc after the excitation of phonons of the electronic origin. If one looks at layer (b) and (c) where the intensity of the origin rises from (b) to (c) again, it seems reasonable to explain that observation by an excitation of phonons of the electronic origin as well as of the vibrational mode at $\tilde{\nu}_{\text{vib}}$ = 128.1 cm^{-1}. Comparing the detected signals of the off-resonantly excited emission signal (a) with an additional, resonantly excited one shown in figure 4.19 (a) one can notice that the five weak signals shifted by more than 100 cm^{-1} to the red of the electronic origin coincide with vibronic transitions into the ground state of Pc. Apart from the two most intense vibronic transitions ($\tilde{\nu}_{\text{vib}}$ = 681 cm^{-1} and $\tilde{\nu}_{\text{vib}}$ = 725 cm^{-1}) occurring also in layer (b) and (c), these transitions remain hidden below the noise level in the other spectra. Beside these vibrational transitions, a signal shifted only about 10 cm^{-1} to the red can be resolved. As already mentioned, this signal can be attributed to the origin of the second emission spectrum. Close to the origin of the FES and SES, three more red-shifted (48 cm^{-1} 63 cm^{-1} 79 cm^{-1}) as well as one blue-shifted signal (-20 cm^{-1}) can be found. It is conspicuous that the double structure at the frequencies 15026 cm^{-1} and 15010 cm^{-1} is repeated with different intensities in the panels (b) - (e). Its intensity nearly vanishes from (c) - (d) while it rises at an excitation frequency of 15700 cm^{-1} again. At higher excitation frequencies this double structure could not be detected anymore. The weak signal shifted 48 cm^{-1} to the red could only be seen in (a). Given the fact that the excitation energy of (a) coincides with the excitation energy of phthalocyanine in the gas phase it can be excluded that the weak emission signals are caused by the emission of vibronic states of bare phthalocyanine. The shift of the signals to this origin ranges between 92 cm^{-1} and 122 cm^{-1} and thus, does not match to the first vibronic resonance of bare phthalocyanine in the gas phase ($\tilde{\nu}$ = 127 cm^{-1} [143]). Hence, these signals can only be an emission of phthalocyanine embedded inside superfluid helium droplets. There are two explanations of their origin. These signals could represent the emission of different helium phthalocyanine complexes whose intensities are not only influenced by the amount of the excess energy. That could mean that they might be evidence for other solvation conformers. Another possible explanation for these signals could be the excitation of complexes between phthalocyanine and gas molecules such as water, oxygen, nitrogen or the rare gas argon. These substances might be left in small quantities inside the chamber binding to the Pc inside the helium droplets. Such signals could be found in the LIF spectrum between 15088.9 cm^{-1} and 15073 cm^{-1} and were assigned to argon, nitrogen and water clusters [86]. But only in case of argon the origin was identified [141]. In the presented emission spectra (figure 4.19), the origin of Pc-Ar could not be observed and between 15088.9 cm^{-1} and 15073 cm^{-1} no additional signals were found. Thus, these signals do not belong to the Pc-Ar cluster and do not coincide with the peaks found in the excitation spectrum, either. However, the experimental data of this work does not suffice to confirm one of these explanations.

$\tilde{\nu}_{\text{ex}}/\text{cm}^{-1}$	$\tilde{\nu}_{\text{ex}} - \tilde{\nu}_0/\text{cm}^{-1}$	$\tilde{\nu}_{\text{vib}}/\text{cm}^{-1}$	$\tilde{\nu}_{\text{vib}} - \tilde{\nu}_{\text{ex}}/\text{cm}^{-1}$	$\tilde{\nu}_{\text{ex}} - \tilde{\nu}_{\text{vib}}/\text{cm}^{-1}$	$\frac{I_{SES}}{I_{FES}+I_{SES}}$
15088.9*	-	-	-	-	1.5 %* / $\ll$ 1 %
15092.7	3.7		-	70.1	$\ll$ 1 %
15110.0	21.1		-	52.8	1.0 %
15123.0	34.1			39.8	1.8 %
15131.8	42.9		-	31.0	5.0 %
15150.0	61.1		-	12.8	5.8 %
15162.8*		73.9			2.7 %*
15175.0	86.1		12.2	42.0	7.2 %
15190.0	101.1		27.2	27	10.1 %
15201.8	112.9		39.0	15.2	15.1
15203.3	114.4		40.5	13.7	13.2 %
15207.0	118.1		44.2	10	13.0 %
15217.0*		128.1			6.5 %* / 7.7 %
15222.9*		134.0			-
15240.0					12.9 %
15265.5*		176.6			-
15314.6*		225.7			21.2 %*
15500.0	411.1		185.4	62.0	35.5 %
15510.0	421.1		195.4	52.0	34.7 %
15562.0*		473.1			-
15564.7*		475.8			-
15600.0	511.1		35.3	53.8	42.9 %
15638.6	549.7		73.9	15.2	46.0 %
15653.8*		564.9		47.2 %	47.2 %* / 46.9 %
15695.0	606.1		42.1	70.9	47.8 %
15700.0	611.1		46.2	65.9	53.6 %
15752.0	663.3		98.2	13.9	45.3 %
15752.2	663.3		98.4	13.7	42.6 %
15765.9*		677.0			51.1 %* / 50.9 %
15790.0	711.1		24.1	18.5	52.2 %
15794.8	705.9		28.9	13.7	54.2 %
15800.0	711.1		34.1	8.5	52.2 %
15808.5*		719.5			53.9 %* / 52.7 %
15830.0	741.1		21.5	52	53.1 %*
15868.3	779.4		59.8	13.7	55.5 %*
15882.0*		793.0			58.2 %* / 56.2 %
15905.0	816.1		23	-	58.7 %*
15910.0	821.1		28	-	57.1 %*

Tab. 4.2: Overview of data derived from the different emission spectra. The data marked with * has been taken from [105].

Since the blue-shifted signal in (a)-(c) indicates a higher transition energy than the electronic origin, it might be explained by an emission of phthalocyanine molecules which are not relaxed into the vibrational ground state of S_1. As the first vibrational mode in S_1 contains 73.9 cm^{-1}, a transition between this state and the vibrational ground state of S_0 (Δv= −1) would be supposed to show a blue shift of this value with respect to the electronic origin. The transition following Δv= 0 would lead to a red shift of about 13 cm^{-1}. Thus, these transitions do not explain the 20 cm^{-1} blue-shifted signal in the spectra. Since the laser radiation was eliminated by a background subtraction, it might be possible that the blue-shifted signal is only an experimental artifact.

In addition to the signals found in (a), figure 4.19 (b) shows one more intense resonance at 14911 cm^{-1}. It could be shown that this signal appears after using a new Pc sample which contains impurities such as water, oxygen and nitrogen. This signal decreases over time (Fig. 4.19 (b) red curve, the drift in this panel is due to the background subtraction). Most probably it is caused by the emission of an excited phthalocyanine water complex inside the droplets.

In the next part the intensities of FES and SES were included into the analysis. When taking the relative intensity $\frac{I_{SES}}{I_{FES}+I_{SES}}$ into account, values of 7.2 % (Fig. 4.19 (c)) and 7.7 % respectively (Fig. 4.13) can be found. The values of the relative intensities derived from all experiments are listed in table 4.2 and plotted in figure 4.21. They could be compared with the intensity ratios published in Ref. [105] which are also plotted in figure 4.21 (stars). The red curve represents a polynomial fit to the data points according to the method of the least square error. It shows that the intensity ratios 6.5 % at the vibrational mode $\tilde{\nu}_{vib}$ = 128.1 cm^{-1} and 2.7 % at $\tilde{\nu}_{vib}$ = 73.9 cm^{-1} found in reference [105] lie far below the curve which was fitted to the experimental data. This observation is in contrast to the deviation between the intensity ratio found after the excitation at the electronic origin and the corresponding value from [105], which lies significantly higher than the fitted curve. As long as it does not seem reasonable that the same experimental setup leads to different shifts, one could only speculate about single outliers at the origin or after the excitation at the vibronic modes. Looking at the data recorded at $\tilde{\nu}$ = 15217.0 cm^{-1}, one can see that the value from [107] as well as the data collected in this study also lie clearly below the fitted curve. These observations could equally be seen as experimental outliers, but it also seems reasonable to interpret this observation as an exception since the data was reproducible. This would mean that the transition between the two different helium solvation configurations would not only be dependent on the excess energy. Since an off-resonance excitation can contain two different contributions, the excitation of phonons and the excitation in the falling edge of a molecular transition, the relation between both also seems to affect the transition between the different helium solvation complexes. Such an observation could be already found in case of the magnesium-phthalocyanine and phthalocyanine-argon clusters inside helium droplets [107]. There, an increase of the intensity of the SES was observed after the excitation at the PW.

With respect to the emission signal (d) (Fig. 4.19) recorded after the excitation at 15500 cm^{-1} (area II) only a very weak resonance could be detected. The frequency of this signal is coincident with the electronic origin of Pc inside helium droplets. Beside this, only a week signal of the double peak at 15026 cm^{-1} could be observed due to the low signal-to-noise-ratio. On account of the fact that the excitation energy of (d) is far off any electronic or vibronic transition, the emission has to be assigned to phonons of the electronic origin of phthalocyanine trapped inside helium droplets. Phonons are modes of the helium environment which are coupled to the dopant excitation [4]. Three types may be distinguished: volume modes of the superfluid helium environment which are thought to be broad, unstructured and their transition probabilities are much lower than those of molecular transitions, then surface modes of the helium droplet and van der Waals modes of the non-superfluid helium solvation layer which are expected to show sharp spectroscopic signatures. At the excitation frequency of (d) it is most likely that the volume modes of the

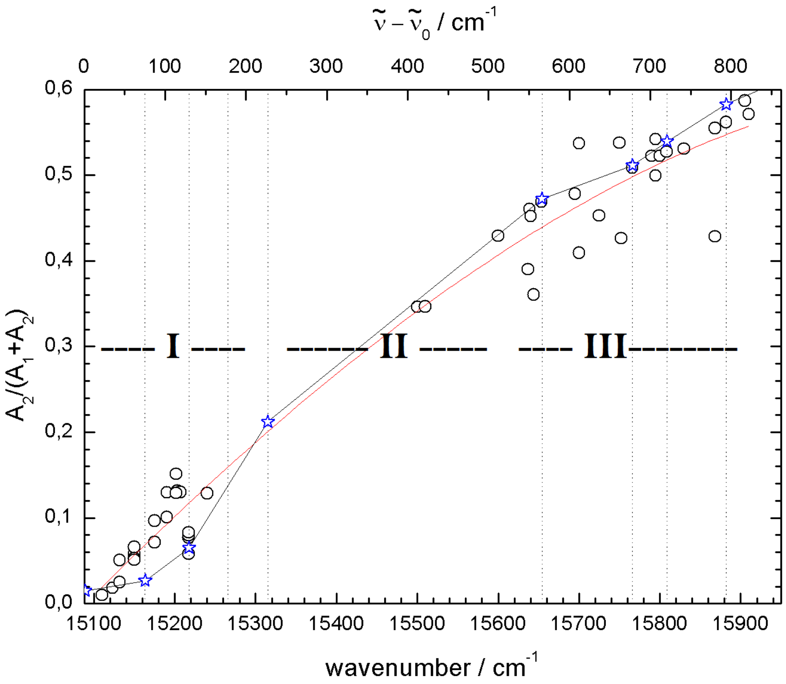

Fig. 4.21: Relative intensity of the SES deduced from the spectra of phthalocyanine inside helium droplets ($\bar{N} \approx 20.000$ helium atoms) for each detected frequency. ⋆ marks the intensities taken from [105].

helium droplet are excited. It is striking that the signal in (d) does not show the origin of the second emission spectrum. According to figure 4.21 the relative intensity between FES and SES should be around 30 % which leads to a value of about $1.7 \cdot 10^{-4}$ s^{-1}. Although this signal intensity is only slightly higher than the noise and might be covered by the bad signal-to-noise-ratio, nobody would expect this observation. Thus, this signal has been examined again in the second measurement series. Nevertheless, the observed signal in Fig. 4.19 (d) clearly shows electronic origin of the FES, which indicates that the phonon band is extended over a wide spectral range.

Far more interesting signals than in (d) can be found after the excitation in area (III). By an analysis of the spectra recorded upon excitation in the frequency area (III) (figure 4.19 e - h) it becomes obvious that the intensity of the electronic origin increases again substantially. Comparing these signals, one can realize that the intensity in layer (g) is 2 times higher than in (f) and 3 times higher than in (e, h). The excitation energy of (g) is significantly closer to a vibronic transition than the other excitation energies. That could indicate that the intensity of the observable fluorescence of a phonon excitation, which might be induced by vibronic modes, decreases in general with the distance to the next red-shifted vibronic mode. The further blue-shifted the excitation from a vibronic transition, the less of the corresponding PW can be excited. Figure 4.21 shows that the relative intensities in area (III) are scattered around the data found in Ref. [105]. At 15700 cm^{-1} the value varies between 41 % and 53 % (e). The data recorded at 15750 cm^{-1} and 15752.2 cm^{-1} revealed values of 53 % and 42 % (f). The excitation at 15868.3 cm^{-1} (cf. panel h) leads to a very low value of only 43 %, which lies far below the expected value. At the frequency 15794.8 cm^{-1} an intensity ratio of 50 % and 54 % could be derived, which both correspond to the expected values. The high uncertainty of the values seems to be caused by a fluctuation in the experimental parameters during the different measurements.

As already discussed, the double peak found after the excitation in area (I) could be observed in area (III) only at a frequency of 15700 cm^{-1}. It seems that not only the excess energy but also individual frequencies support these signals. Looking at the panels (f) - (h) it is conspicuous that these spectra reveal a third sharp emission signal shifted by 24.5 cm^{-1} to the red of the origin of the FES. It is notable that this signal at $\tilde{\nu}$ = 15064.5 cm^{-1} looks quite similar to the origin of the second emission spectrum. Compared to the gap of 10.2 cm^{-1} between FES and SES the spacing between SES and the third signal of 14.3 cm^{-1} is only slightly higher (about 4 cm^{-1}). Thus, this signal might indicate the existence of a third electronic origin and consequently would lead to experimental evidence of another local minimum on the potential energy surface of the phthalocyanine-helium interaction in the excited state. Beside this signal, panel (f) reveals a weak emission double structure which is 57 cm^{-1}, 67 cm^{-1} shifted to lower frequencies than the origin of the FES. Moreover, it is notable that the splitting of 10 cm^{-1} of this double peak is the same than the splitting between FES and SES. Thus, these two signals are different than the double structure observed in (a) - (e). It might also be explained by a configurational variant of the Pc-helium solvation complex.

Further experiments were performed and figure 4.22 shows these emission spectra of Pc between 14945 cm^{-1} and 15140 cm^{-1}. They were also excited off-resonantly to any molecular transition of phthalocyanine. The relative intensities were summarized in table 4.2 and plotted in figure 4.21. The excitation energies have been changed from 15100 cm^{-1} (area I) up to 15905 cm^{-1} (area III). All recorded emission signals show the origin of the first emission spectrum at 15089 cm^{-1} as well as of the second one at 15078.8 cm^{-1}.

Some panels (1, 2, 5 - 7 and 9) show sharp emission signals blue-shifted to the ZPL of phthalocyanine. It was not possible to clarify the origin of these signals. More data will be needed to explain the origin of these blue-shifted emission signals.

If one looks closer at the data recorded after the excitation at a frequency of 15110.0 cm^{-1} and 15123.0 cm^{-1} (cf. Fig. 4.22 no. 1 and 2) (area I), values of 1.0 % and 1.8 % could be extracted for the relative intensities. By comparing these two results with the intensity of 1.5 % found after the excitation of the electronic origin in [105], it becomes clear that they do not correlate. The higher excess energies lead to a lower relaxation of the Pc helium solvation complex. This supports the assumption mentioned above that the result of 1.5 % maybe has to be corrected or the different observations have to be attributed to the differences of the experimental setups. The other values of the ratio in area I are distributed around the fitted curve. It might be supposed that not only the experimental noise causes this spread of the data, but also the influence of the phonon modes to the transition efficiency between different helium configurations has to be taken into account. Beside the two electronic origins, both panels no. 1 and 2 show more different sharp signals, some of them could be already observed in figure 4.19. The first vibronic transition at 15002 cm^{-1} [86] cannot be detected because its expected intensity is far below

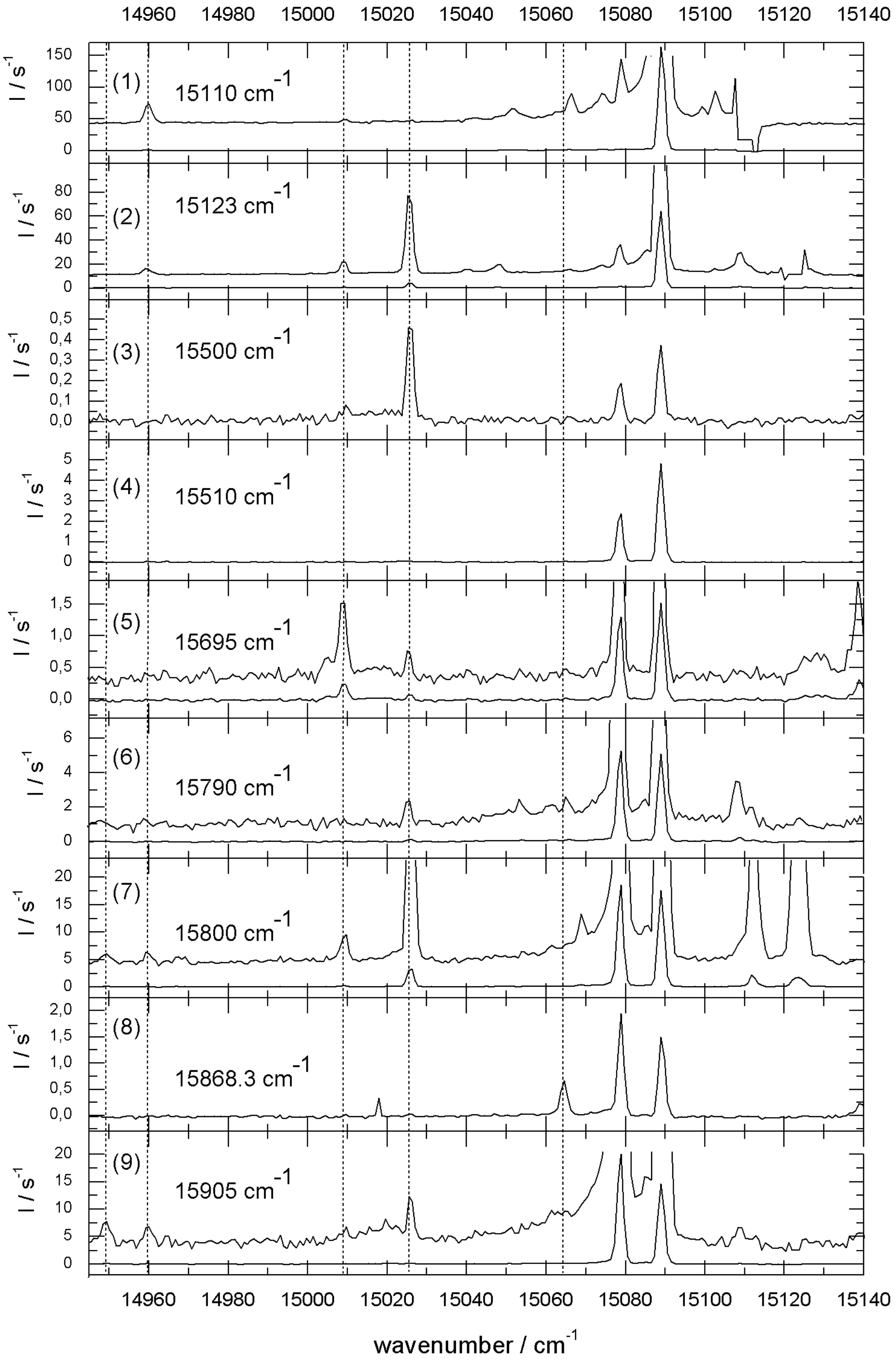

Fig. 4.22: Dispersed emission spectra of phthalocyanine inside helium droplets ($\bar{N} \approx$ 20.000 helium atoms) between 14945 cm^{-1} and 15140 cm^{-1} excited at different frequencies.

the detection limit and only the next vibronic transition at 14960 cm^{-1} can be found. This signal stays above the detection limit as long as the origin of the FES or SES shows more than 10 counts per second (cf. Fig. 4.22 no. 1,2,7 and 9).

The value of the intensity ratio in area (II) plotted in Fig. 4.21 was taken from the second measurement series. Figure 4.22 shows the emission signals of these experiments. In this figure panel no. 3 and 4 were recorded after the excitation at a frequency of 15500 cm^{-1} and 15510 cm^{-1}. In both experiments two sharp peaks could be detected which arise at the frequencies of the origin of the FES and SES. The intensity found after the excitation at 15500 cm^{-1} is one order of magnitude lower than detected after the excitation at 15510 cm^{-1}, but is still far more intense than the signal in panel (d) (cf. Fig. 4.19). The relative intensity ratio around 30 % fits to the value expected at an excess energy of about 410 cm^{-1}. These values are listed in table 4.2 and also plotted in figure 4.21. Based on these findings it seems reasonable to argue that the SES in figure 4.19 (d) must be covered by the experimental noise. It might also be reasonable to assume that the poor signal in (d) is a result out of a drift or even a shift of the excitation frequency of the laser before or during the experiment. The higher, absolute signal intensity detected at $\tilde{\nu_{ex}}$ =15510 cm^{-1} indicates any structure in the phonon band, a weak maximum of a molecular transition or is again influenced by the relation between the excitation of phonons and the excitation in the falling edge of a molecular transition. Nevertheless, all emission spectra recorded upon excitation in area (II) show that phonons of phthalocyanine inside helium droplets can be excited in a extremely wide spectral range which goes up to at least 400 cm^{-1} shifted to the blue of the ZPL.

The analysis of the results of the second measurement series (Fig. 4.22) in area (III) leads to similar conclusions which were already found in the first series. The spectra no. 5 - 9 were recorded after an excitation off-resonant to any molecular transition in the range between 15695 cm^{-1} and 15905 cm^{-1}. All emission spectra show two intense resonances at 15089 cm^{-1} and 15078.8 cm^{-1}, which can be attributed to the two origins of the FES and SES of phthalocyanine inside helium droplets. By comparing the absolute signal intensities in panel no. 8 to panel (h) in Fig. 4.19, which were both excited at 15868.3 cm^{-1}, it can be noted that the second series is one order of magnitude more intense. This might be due to experimental conditions and should be taken into account for the other data. The spectra shown in panel 5 and 6 of Fig. 4.22 are recorded upon excitation at 15695 cm^{-1} and 15790 cm^{-1}, respectively. These excitation frequencies are close to those used in panel (e) and (g) of Fig. 4.19. But the first two are closer to the corresponding red-shifted vibronic resonance than the latter two. It can be recognized that the intensity of the emission signals increases by one order of magnitude. It seems reasonable to attribute that to experimental conditions, since the LIF spectrum does not show a change of the signal in this region. Thus, the shifts in the excitation energy of 5 cm^{-1} and 4.8 cm^{-1} do not affect the absolute intensities of the emission signals significantly. The intensity ratio between FES and SES derived from the emission signals in panel 5 and 6 (Fig. 4.22) result in the values 48 % and 52 %. These findings match very well with the expected intensity ratio between FES and SES. Panel no. 7 was recorded after the excitation at 15800 cm^{-1}. Even though this frequency is close to the excitation frequency of panel (g), the intensity of its emission signal is increased by a factor of 30. The shift in the excitation energy of 5.2 cm^{-1} increases the distance to the next red-shifted vibronic transition and decreases the gap to the next blue-shifted one. These effects should not be sufficient enough for nearly tripling the intensity, one order of magnitude is thought to be experimental framework. Since there is no change in the LIF spectrum, the rearrangement of the helium solvation layer seems to depend on the relation between the two different contributions, the excitation of phonons and the excitation in the falling edge of a molecular transition. The relative intensity ratio in panel no. 7 can be calculated to a value of 52 %, which again fits very well to the expected one. The detected emission signal shown in panel no. 8 reveals a relative intensity ratio of 55 %, which also fits well to the expected value. Beside the origin of the FES and SES, this emission signal is the only one in figure 4.22 which shows the third emission signal. This signal is shifted by nearly 25 cm^{-1} to the red of the origin of the FES and has already been observed in the panels (f) - (h) in Fig. 4.19. It is striking that the excitation frequencies of these spectra coincide with the excitation energy of high energetic vibronic modes of the Pc-Ar_1 cluster inside helium droplets. It can be noticed that a tripling of the emission signal has already been observed for Pc-Ar_1, but the splitting found in this case was only in the order of 14 cm^{-1} [107]. The fact that an excitation between the vibronic transition of the Pc-Ar_1 cluster and the corresponding transition of bare Pc (cf. panel no. 7) does not lead to the additional emission signal indicates that the intensity of this signal cannot be enhanced by increasing the excess energy. Thus, it seems that the relation between phonon excitation and the excitation in the edge of a molecular transition determines this resonance in the emission signal. It can only be observed after an excitation 15.2 cm^{-1} red-shifted to the vibrational modes (677.0 cm^{-1}, 719.5 cm^{-1} and 793.0 cm^{-1}) of Pc. The last spectrum no. 9, which can be seen in Fig. 4.22, was excited at a frequency of 15905.0 cm^{-1}. It reveals again only two intense resonances at the frequencies of the first and second emission spectrum of phthalocyanine. Compared to panel no. 8 the absolute intensity rose about one order of magnitude and the relative intensity ratio reveals a value of 58 %, which lies in the order of the value expected at this excess energy.

It is obvious that the relative intensity ratios extracted from the second measurement series clearly show less dispersion from the expected values than the data derived from the spectra shown in Fig. 4.19. One obvious difference between these two series is the absolute intensity of the detected signals. That leads to the assumption that the higher the absolute intensity, the better the derived relative intensity might be. Thus, it seems reasonable that the high fluctuation in Fig. 4.21 area (III) is due to the low intensities of the detected emission spectra. Table 4.2 summarizes all intensity data extracted out of the different emission spectra. The data marked by * are taken from [105]. Both measurement series (cf. Fig. 4.19 and 4.22) show that the intensity of the SES rises in contrast to the intensity of the FES. As already mentioned above, the intensity pattern of the two origins is mostly similar to the intensity ratio detected after the excitation of the nearby vibronic transition. The values of the relative intensity ratio match the data published in [105] apart from the electronic origin as well as the 73.9 cm^{-1} and 128.1 cm^{-1} vibrational modes. The absolute intensity varies with the spectral gap between excitation frequency and ZPL / vibronic mode. The different absolute intensity between panel no. 7, 6 (Fig. 4.22) and (g) (Fig. 4.19) as well as the fact that the intensity of the electronic origin in layer (e) is smaller than in (f) (Fig. 4.19) might imply that the rearrangement is influenced by the ratio of the two components, phonons and off-resonant excitation of molecular transitions that contribute to the detected emission signal.

Some of the vibronic transitions of Pc can be resolved in the emission signals shown in figure 4.22. The first vibronic mode of Pc cannot be resolved in contrast to the second one which can be seen in the panels no. 1, 2, 7 and 9. The higher energetic vibronic transitions, which could also be detected, are not shown in the frequency range of figure 4.22. They coincide in their spectral position and relative intensities with the vibrational structure of the FES. The vibronic transitions of the SES could be detected in panel no. 7 and 9 of the second measurement series 4.22. They show the same intensity distribution compared to the vibrational resonances of the FES which was found at the corresponding origins.

When one looks for identical signals in both measurement series, some of the emission signals can be found again. Beside the origin of the FES, SES and the signal at 15064 cm^{-1} some more can be found in different spectra. At the frequencies $\tilde{\nu}$=15026 cm^{-1} and $\tilde{\nu}$=15010 cm^{-1} the double peak could be found in nearly all panels expect of no. 1, 4 and 8. It is notable that this structure is missing after the excitation at the transition energy of the Pc-Ar_1 complexes (15.2 cm^{-1} red-shifted to molecular transitions of Pc) and only in these spectra the third emission signal at 15064.5 cm^{-1} can be observed. This correlation could not have been explained so far. The additional weak signals found in panel no. 1 and 2 are shifted up to 49 cm^{-1} and could not be found in any other spectrum or in the first measurement series (cf. Fig. 4.22).

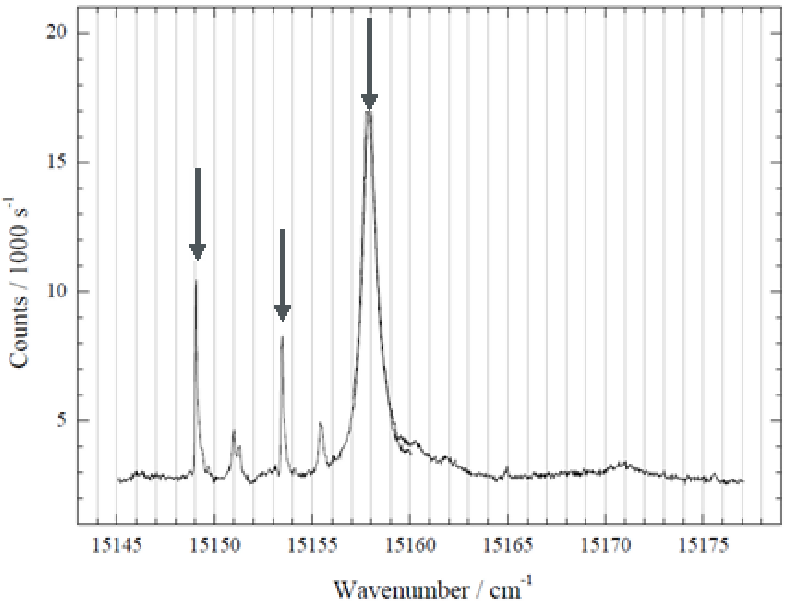

Fig. 4.23: LIF spectrum of phthalocyanine inside helium droplets ($\bar{N} \approx 20.000$ helium atoms) taken from [86]. The excitation frequencies of the emission spectra are marked by arrows.

4.2.7 Low Frequent Vibronic Excitation

Another spectroscopic examination was provided to the first vibronic transition of phthalocyanine inside helium droplets and revealed an unexpected result. The LIF spectrum of this transition is shown in figure 4.23. The phthalocyanine was excited at the vibronic transition at 15157.87 cm^{-1} and at the two resonances at the frequencies 15153.47 cm^{-1} and 15149.06 cm^{-1} which show a similar asymmetric line shape than the electronic origin of Pc. All three frequencies are marked by an arrow in figure 4.23. The two sharp signals between the excitation frequencies in Fig. 4.23 might be due to the emission of phthalocyanine dimers, but this assumption was not verified. The detected emission spectra showed many sharp emission signals. One weak signal coincides with the origin of the normal emission signal of phthalocyanine at 15088.9 cm^{-1} and thus, was attributed to the normal expected emission of Pc. The most intense emission signal could be found blue-shifted to the normal ZPL by 65.5 cm^{-1}. This value is nearly the same than the energy of the first vibrational mode of Pc (68.9 cm^{-1}). Additionally, the most intense emission signal also revealed the vibronic fine structure of phthalocyanine inside helium droplets. However, all these vibronic resonances are also blue-shifted by 65.5 cm^{-1} compared to the normal vibronic modes of Pc. The relative intensities of the blue-shifted vibronic emission signals fit well to the intensities known from the vibronic structure of the normal emission signal of Pc inside helium droplets. Shifted by 65.5 cm^{-1} to the red, this spectrum perfectly matches the normal emission spectrum of Pc. Thus, this second emission signal was also attributed to the radiative decay of excited phthalocyanine inside helium droplets. The vibrational fine structure of the weak emission signal at 15088.9 cm^{-1} remains below the limit of detection and could not be found in the emission spectra. Beside the two different Pc emission signals, additional sharp emission lines red-shifted to the most intense signal could be detected. The emission spectra are shown in figure 4.24. Both signals, the normal electronic origin of Pc as well as the blue-shifted origin with its vibrational structure could be found in the three emission spectra. Only some relative intensities appear differently in the three spectra. Repeating the experiments revealed the same results. Thus, the observed effects are reproducible and it can be excluded that any experimental mistakes might be responsible for the blue-shifted emission. Since the transition energy of the blue-shifted emission is higher than the energy of the ZPL, this observation has to be evidence for an electronic transition which does not follow $\Delta v = 0$. This is remarkable since phthalocyanine is a rigid molecule, which means that the vibrational structure in the ground state and the first excited one are similar. Moreover, in case of rigid molecules the geometrical structure of the nuclei remains nearly the same after an electronic excitation has taken place. Thus, following the Franck-Condon principle, the most intense transitions in absorption as well as the emission spectra of phthalocyanine should be transitions with $\Delta v = 0$. However, the blue-shifted emission is clear evidence that this does not happen and that instead the transition $\Delta v = -1$ is about 30 times more intense than the transition with $\Delta v = 0$. The additional red-shifted signals might be electronic origins of different Pc helium com-

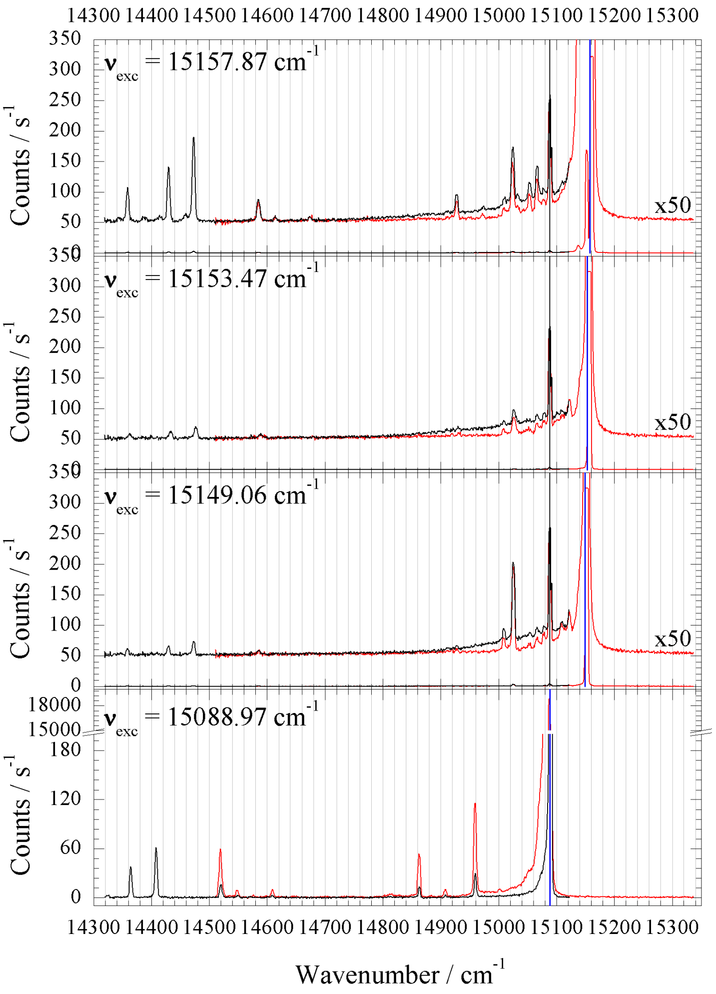

Fig. 4.24: Emission spectra of phthalocyanine inside helium droplets ($\bar{N} \approx 20.000$ helium atoms). The excitation frequencies at 15157.87 cm^{-1}, 15153.47 cm^{-1}, 15149.06 cm^{-1} as well as at the electronic origin at 15088.9 cm^{-1} are marked by the blue lines.

plex isomers. Thus, this observation could be an experimental indication of the existence of such different metastable solvation complexes. After the excitation they can possibly be populated during the low frequent motion and during the following transformation into different low frequent vibrational modes of the Pc molecule. The relative intensities between the origin of FES and SES derived from these experiments were between 7.6 % and 10.9 % after the excitation at 15157.87 cm^{-1} as well as 9.0 % at 15153.47 cm^{-1} and 8.4 % at 15149.06 cm^{-1}. Because of the weak intensity of the SES these values are only rough estimations. Thus, small changes which might occur between vibronic and phonon excitation cannot be proven. Anyway, the values fit to the curve shown in figure 4.21 and thus, lie clearly above the relative intensity of 2.7 % observed at this vibronic transition in [86].

4.3 Conclusions

In this work phthalocyanine has been examined inside superfluid helium droplets by the analysis of high resolution fluorescence excitation spectra as well as dispersed emission spectra. From many empirical findings it is known that the helium environment has got different effects on the spectroscopic properties of organic chromophores [4], which cannot be observed in the gas phase experiment. During the last 20 years the idea of a solvation complex consisting of the chromophore and non-superfluid helium atoms was developed and established to provide a model that explains the microsolvation effects occurring inside the helium droplets. It claims a non-superfluid helium solvation layer bound to the chromophore located inside the superfluid helium droplets. Both helium fractions, the non-superfluid as well as the superfluid one, affect the spectroscopic properties of the chromophore. These structural and dynamical effects are related to additional signals as well as line broadening in the electronic spectroscopy. The model could describe empirically different, experimentally observed spectral features like line shapes, line broadening, phonon wings and different solvation complexes. These effects are absent in the data recorded in the gas phase. Studying the literature one has to note that there are some characteristic criteria which are commonly attributed to the phonon wing. Nevertheless, these experimentally observed effects might be attributed to the right phenomena, but they do not provide enough information to allow a clear distinction between ZPL and PW. It becomes more doubtable if structured and sharp spectral signals are assigned to van der Waals modes between the non-superfluid helium and the chromophore. This common practice is challenged and has to be critically questioned. Additional experiments are required to prove whether this is true. Since gas phase experiments of huge complexes between a chromophore and rare gas atoms or molecules do not show sharp spectroscopic signals of the van der Waals modes, it seems reasonable to discuss the microsolvation inside helium droplets from a different perspective.

In the course of the spectroscopic examination of the helium-mediated vibrational predissociation [141] of the van der Waals cluster Pc-Ar_1 inside the droplets presented in this chapter, it could be shown by dispersed emission spectra that this dynamic process does not occur. Experiments with bare Pc made a revision of the previous interpretation necessary. Obviously, the typical dual emission of bare Pc can be recorded far off any molecular resonance throughout the electronic excitation spectrum of Pc. Up to now the reason for this observation could not be completely clarified. The detected emission signals may arise from two different contributions, the excitation of phonon modes of the superfluid helium droplets or the excitation in the tail of the Lorentzian line shape of a molecular transition. The presented data does not suffice to distinguish between both effects. Moreover, it cannot be excluded that both effects, the PW and the excitation in the edge of a ZPL, are involved at the same time. However, by means of spectroscopic methods it is impossible to detect both signal contributions separately.

The detailed examination of dispersed emission spectra upon far-off-resonant excitation revealed unexpected signals which are neither part of the FES nor of the SES of Pc. These narrow signals were found in the frequency range between the electronic origin and the vibronic modes in the emission spectra of Pc. The unexpected rich spectral features reveal surprising dynamic processes. It is known that the helium environment is perturbed due to the electronic excitation of the molecule [100]. Thus, it seems reasonable that such a change of the electron density distribution of phthalocyanine also massively affects the non-superfluid helium solvation layer around the chromophore [106]. From this Franck-Condon-like point the Pc helium complex might be reordered, and relaxes into a cascade of metastable as well as stable configurations of the helium solvation complex. This explanation seems to be the most likely one, describing the unexpected signals in the emission spectra presented in this chapter.

As already shown in previous experiments, it is known that the relaxation of the configuration of the helium solvation layer depends indirectly on the vibrational state of the molecule and is enhanced due to additional excitation of higher molecular vibrations [105]. In addition, it was noted that the relaxation probability is also influenced directly by vibrations of the solvation layer. In case of Mg-Pc and Ar-Pc a massive increase of the SES could be observed [104]. The data presented in this work of bare Pc showed that no unexpected increase of the intensity of the SES could be found. The excitation frequency was set resonantly to an intense signal blue-shifted to the electronic origin which is assigned to van der Waals modes of the Pc-He solvation complex [88]. This observation implies that the assignment of this signal to the phonon wing must be critically reviewed.

All these experimental results lead to the question whether the experimental criteria are sufficient to distinguish between ZPL, PW, and metastable variants of the configuration of the solvation complex. The standard criteria such as a blue shift in the excitation spectra, saturation behavior, and the red shift of the emission signal are challenged. They might be necessary but not sufficient to unequivocally identify PW signals. These criteria do not exclude any of the three phenomena for the assignment nor do they favor one of them. In this regard, when one looks at structured and narrow spectroscopic signals as found for instance in the case of tetracene, pentacene, porphin or phthalocyanine [88], the assignment of these signals must be critically reviewed. Beside the excitation of phonons and van der Waals modes be-

tween helium and the chromophore, the existence of different solvation complexes has to be taken into account. The data presented in this chapter showed that spectroscopic observations like saturation behavior, stokes shift in the emission spectra, relaxation probability of the solvation complex etc. do not allow to distinguish between solvation complexes and van der Waals modes of the PW. Thus, up to now the two different phenomena induced by the microsolvation inside helium droplets cannot be clearly separated and identified.
During the investigation of phthalocyanine another surprising observation could be found. A direct radiative decay without previous dissipation of the vibrational energy has been observed for the lowest vibronic level accessible via electronic excitation. Moreover, the radiative decay follows $\Delta v = -1$ instead of the expected $\Delta v = 0$ transition. Only a small fraction of these excited molecules decays via dissipation of the vibrational energy prior to radiative decay. This effect could be observed exclusively for the first vibronically excited level of Pc, all other vibronically excited levels follow dissipation prior to radiative decay.

The results presented in this chapter have shown the need for further examinations. The main difference between PW and a metastable solvation complex is the electronic ground state. In the first case it is shared with the ZPL while in the second case it is not. Only pump-probe experiments are able to prove a common ground state among a series of signals. In the present case a second single mode ring dye laser would be needed to perform such pump-probe experiments. Based on such experimental data, theoretical methods to simulate microsolvation in superfluid helium droplets should look for metastable configurations in addition to the global minima. Besides, the van der Waals modes of stable and metastable solvation complexes are needed. By these means it might be possible to decipher the helium-induced signals and, thus, microsolvation in superfluid helium droplets.

5 Depletion Spectroscopy

Within the scientific project of this thesis a bolometer was implemented into the continuous flow helium droplet machine in order to serve as a detector for recording depletion spectra of electronic transitions. Therefore, various test measurements have been performed to demonstrate the proper functioning and the sensitivity compared to fluorescence excitation spectra.

5.1 Introduction

A new commercially available bolometer had to be implemented into the experimental setup as well as into the data acquisition program. This part of the work was finally completed by test measurements with a substance whose spectroscopy in helium droplets is well-known from fluorescence excitation spectra. Since phthalocyanine is hardly soluble by any solvent and thus, hardly removed when condensed on a cold surface, another more volatile dopant species, namely pentacene, was chosen to test the bolometer. Beside the existing previous knowledge on the electronic spectrum of pentacene in helium droplets [86, 88], it was fortunately accessible by our cw ring-dye-laser. At room temperature pentacene ($C_{22}H_{14}$) is a dark purple powder with a triclinic crystal structure. The molecule consists of five linearly associated benzene rings. Figure 5.1 shows the corresponding Lewis structure. This polycyclic aromatic hydrocarbonic system (PAH) is planar and highly conjugated and therefore acts like many other organic semiconductors. Classicially it can be synthesized by the Elbs reaction, which is a pyrolysis of an ortho-methyl substituted

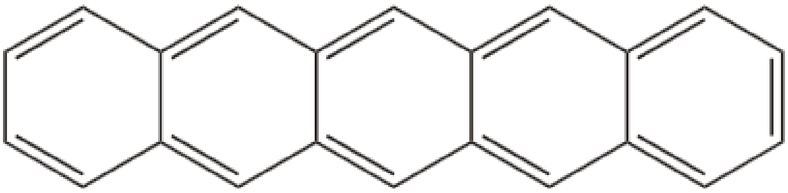

Fig. 5.1: Lewis structure of pentacene.

benzophenone [144]. Alternative syntheses are described in [145, 146]. In the series of the linear (poly)acenes pentacene is the fifth after tetracene. They can be excited into higher electronic states upon absorption of ultraviolet or visible light. The absorption and emission in this homologous series is shifted with the number of benzene rings to lower frequencies. While bare benzene shows ultraviolet absorption and emission, the fluorescence of tetracene can be found in the visible region of electromagnetic radiation. This red shift can be explained by the extension of the conjugated π-electron system by each benzene ring. Pentacene belongs to the point group D_{2h}, the first electronic transition is a $\pi \rightarrow \pi^*$ transition. It starts in the ground state X^1A_g and ends in the first excited state A^1B_{2u}. The intersystem crossing rate between S_1 and T_1 is negligibly small and the fluorescence quantum yield in p-terphenyl could be determined as about $\Phi_F = 0.78$ [147]. The spectral properties of pentacene have been investigated in different matrices [147–149], in supersonic jets [150–153] as well as in superfluid helium droplets [86, 90].

5.2 Experimental Details

5.2.1 Bolometer - Basic Experiments

On account of the fact that the electronics of the bolometer detector are sensitive to the gradient of a signal (cf. chapter 3.3.3), only the change of a signal can be detected. Therefore, the modulated flux of the pulsed helium droplet source was the ideal system for first test measurements. A detailed description of the bolometer unit, the description of the data acquisition software as well as the filling procedure of the bolometer dewar with liquid helium and the cryo pumping can be found in chapter 3.2.3.

In the first experiment the response of the bolometer detector to the pulsed helium droplet beam was recorded. In figure 5.2 this signal is depicted. Without further amplification it was fed into the oscilloscope. About 1 ms after the trigger pulse sent to the pulsed droplet source a broad, positive signal could be detected at the bolometer. Since the width of the droplet pulse is in the order of 50 μs [76], the shape of the signal (FWHM ≈ 200 μs) has to be due to internal time constants of the bolometer electronics. For a well-known distance from the nozzle to the detector of 0.4 m the velocity of the droplet pulses can be determined to 400 $\frac{\text{m}}{\text{s}}$. This value fits to the expected speed of a helium droplet beam at the given stagnation conditions. The signal shown in Fig. 5.2 decays exponentially and no additional signal

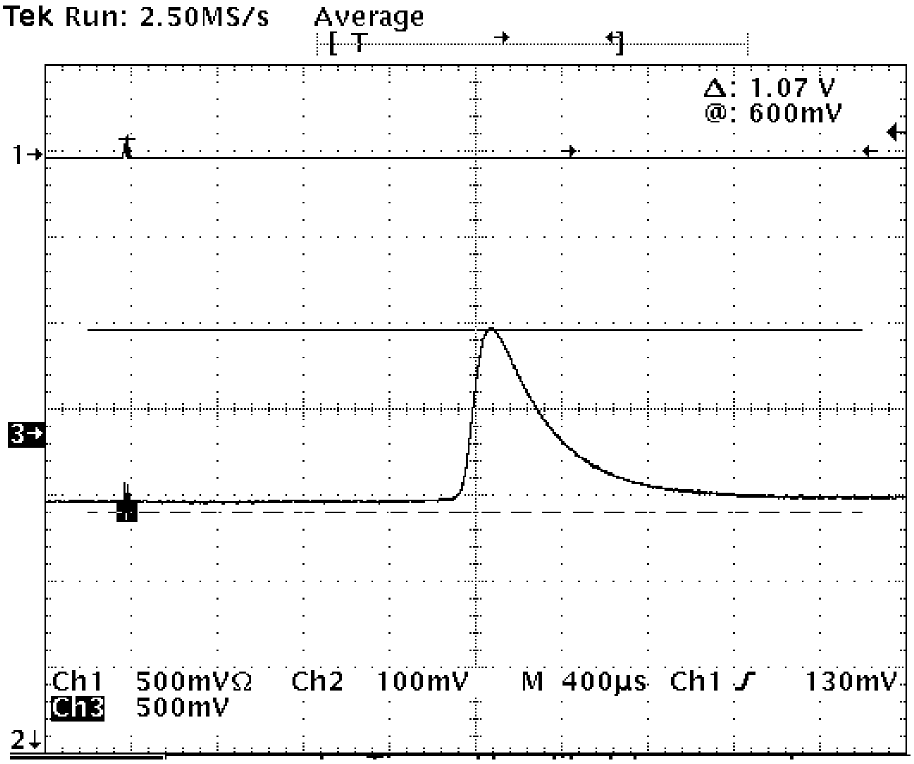

Fig. 5.2: Response signal from the bolometer detector to the pulsed helium droplet beam. The signal was accumulated over 80 shots of the orifice.

contribution could be detected between two helium droplet pulses. Since the bolometer can only detect the change in the energy flux to the silicon diode, the pulsed helium droplet beam should cause both, an increase as well as a decrease in the energy flux. Thus, the detector should show a positive as well as a negative signal. It can be noticed that the signal in figure 5.2 only shows a positive contribution. The negative signal contribution might not detectable on the time scale of ms due to the time resolution of the bolometer electronics.

Since the velocity of the helium droplets depends on the nozzle temperature, the bolometer signal should be sensitive to the arrival time of the helium pulses. This was examined by varying T_0. Figure 5.3 shows the bolometer signals for this exam-

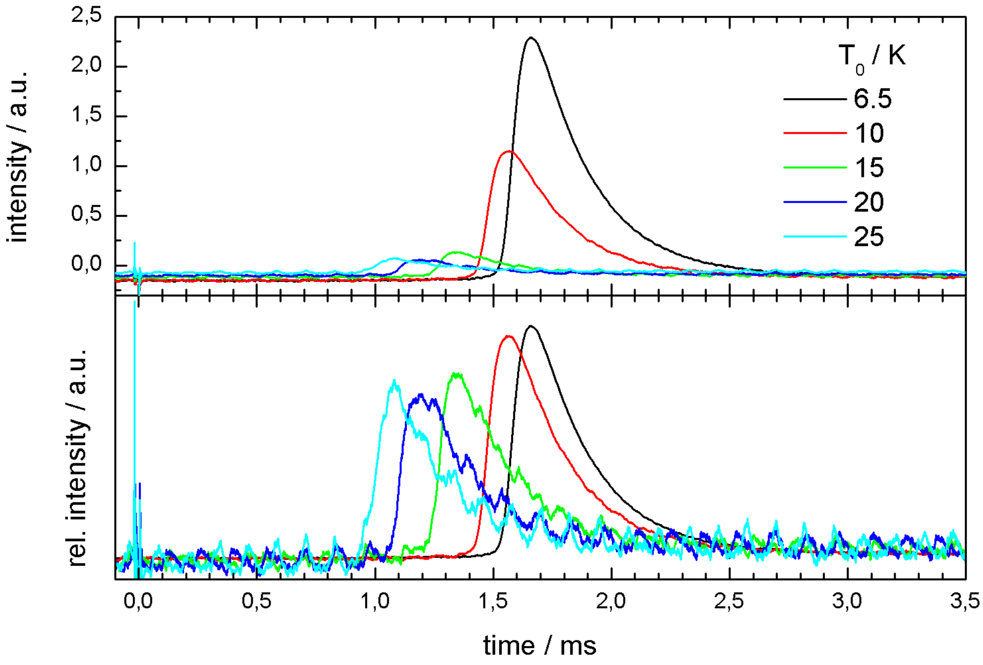

Fig. 5.3: Response signal from the bolometer detector to the pulsed helium droplet beam at different expansion temperatures T_0 (p_0 = 80 bar, repetition rate 3 Hz). The signals are accumulated over 80 shots of the orifice. The signals in the lower panel were normalized.

ination. The repetition rate was set to 3 Hz, the stagnation pressure p_0 was kept at 80 bar and all signals were accumulated over 80 shots. The signals in the lower panel were normalized. It can be seen that the maximum of the signal shifts from 1.6 ms (T_0 = 6.5 K) to 1.1 ms (T_0 = 25 K). This observation matches the change of the velocity induced by the change of the nozzle temperature T_0 from 6.5 K up to 25 K. This clearly demonstrates the correlation between helium droplet beam and the bolometer signal. The calculated velocities range from 250 $\frac{m}{s}$ to 365 $\frac{m}{s}$. Moreover, it can be seen that the signal-to-noise-ratio of the detected signal decreases with the temperature T_0. It can be noted that there is a massive change in the signal intensity between 10 K and 15 K by one order of magnitude. This observation indicates the transition between sub-critical and super-critical helium expansion, which can be found around 15 K (cf. Fig. 2.6) for the given stagnation pressure of 80 bar. The helium flux inside the detection chamber is lower in case of the expansion of helium gas compared to the expansion of liquid helium, which leads to a decrease of the bolometer signal.

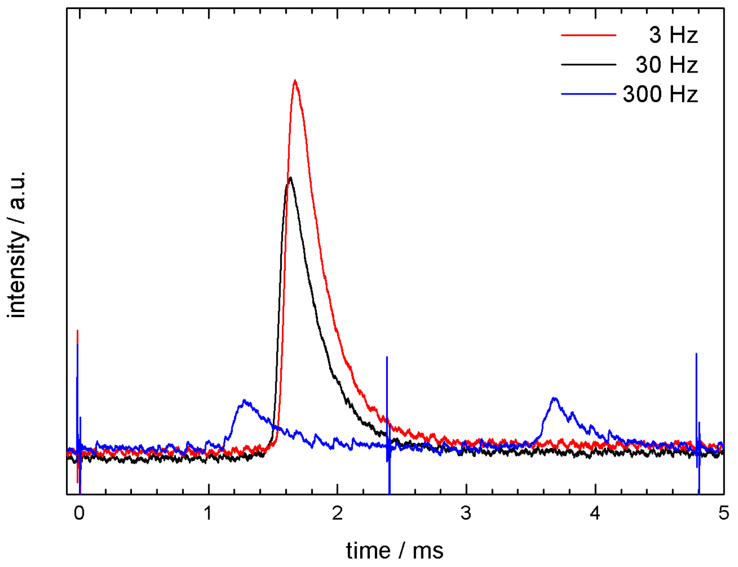

Fig. 5.4: Response signal from the bolometer detector to the pulsed helium droplet beam at different repetition rates of the pulsed orifice.

Finally, the influence of the repetition rate of the pulsed orifice was examined. Figure 5.4 shows the response signal from the bolometer detector to the pulsed helium droplet beam at different repetition rates. As it can be seen, the velocity of the droplet beam increases with the repetition rate. This can be explained by the fact that the pulsed valve and thus, the nozzle is heated by the increased power intake for high repetition rates and consequently, the velocity of the droplets increases. For a repetition rate of 300 Hz the increase of the velocity changes the arrival time of the droplet pulse so that two consecutive gas pulses can be observed within the time scale of the oscilloscope.

In the next step, the bolometer unit was mounted directly to the detection chamber of the continuous flow helium droplet machine. By means of a pair of bellows the bolometer could be aligned to the beam axis during operation. In addition, a mechanical beam shutter was installed in the beam axis of the helium droplet beam.

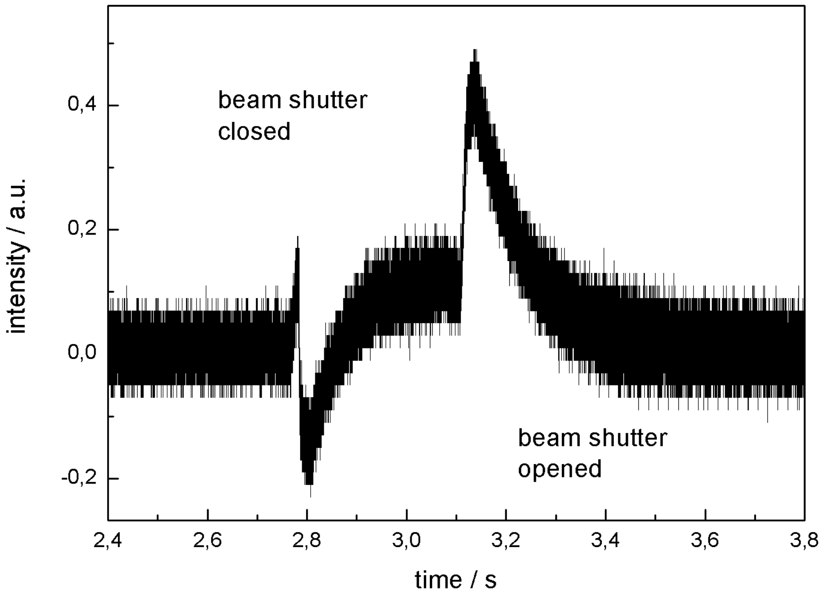

Fig. 5.5: Absolute response from the bolometer detector to the continuous flow helium droplet beam due to subsequent closing and opening of the beam shutter.

By this shutter it was possible to verify the alignment of orifice, pick-up cell as well as bolometer detector. Figure 5.5 shows the response of the bolometer to the closing and opening of the helium droplet beam by the mechanical shutter. By closing the beam shutter a negative signal can be registered. The signal decays exponentially up to a positive signal of about 0.1. When the beam shutter is left closed, this positive signal reaches 0 again. After the beam shutter has been opened again, a steep rising, positive signal can be detected, which decays exponentially down to 0. Figure 5.5 clearly demonstrates that the droplet beam can be detected with the bolometer by means of the beam shutter. This technique was used for the alignment of the pick-up cell, the nozzle and the bolometer detector to a common optical axis. It has to be mentioned that the observed positive depletion in combination with the negative signal are in contrast to the exclusively positive depletion signal detected in case of the pulsed helium droplet beam. The time constant of this experiment is several orders of magnitude higher, which seems to be slow enough to observe both signal contributions. This confirms the assumption that the detection is limited by the time constant of the electronics of the bolometer.

5.2.2 Pentacene

The pentacene was delivered by Sigma Aldrich. The purity of the substance was at least 99.99%, thus, a further purification was not necessary. The probe was pressed to pellets which were placed in the heatable pick-up cell. Optimized pick-up conditions for single molecule doping were found at an oven temperature of 165°C for droplets of an average size of 20000 helium atoms.

The examination of the electronic excitation of pentacene showed that the angle of acceptance of the bolometer plays the decisive role. To achieve a reduced angle, the bolometer was mounted to a third vacuum chamber which was separated from the detection chamber by another skimmer. This increased the S/N ratio of the detectable beam depletion by orders of magnitude.

The electronic excitation of pentacene is followed by a dissipation of fractions of the excitation energy into the helium droplet. Each evaporated helium atom releases about 5 cm^{-1} [78, 79]. By means of the data extracted from emission spectra and summarized in [86] it is possible to estimate the number of helium atoms that are evaporated from the droplet due to the electronic excitation of the pentacene. Figure 5.6 shows an emission spectrum of pentacene in superfluid helium droplets [86] upon excitation at the electronic origin. It can be seen that the most intense transition can be found at $\Delta v = 0$. The other less intense emission signals lead to a vibrational energy $E_{vib} \approx 709\ cm^{-1}$ in the electronic ground state. This energy will dissipate into the helium droplets and thus, the mean droplet size will decrease by about 142 helium atoms. As an estimation, the quantum yield in p-terphenyl $\Phi_F = 0.78$ [147] can be taken into account, which leads to about 110 helium atoms (550 cm^{-1}) that will be evaporated due to the vibrational excess energy in S_0 and about 816 (4080 cm^{-1}) because of the non-radiative decay of the excited pentacene. Thus, the estimation results in two values, 142 and 926 helium atoms, depending on the radiative and non-radiative rate of pentacene inside helium droplets. That means that the mean droplet size will decrease by about 0.7 % to 4.6 % due to an excita-

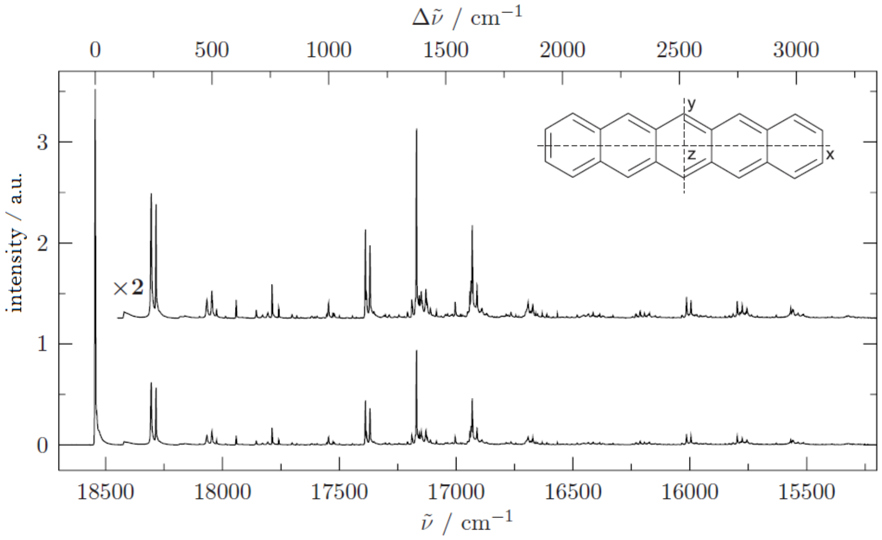

Fig. 5.6: Dispersed emission spectrum of pentacene inside superfluid helium droplets ($\bar{N} \approx$ 20.000) excited at the electronic origin $\tilde{\nu} = 18545.2\ cm^{-1}$ taken from [86].

tion at the electronic origin of pentacene. If one considers the doping process of the droplets, one has to estimate that only 25 % of the droplets are doped with only one pentacene molecule. That means that the depletion of the energy flux detected by the bolometer is at least 4 times smaller.

5.3 LIF and Depletion

Figure 5.7 shows the fluorescence excitation spectrum of pentacene in superfluid helium droplets ($\bar{N}$ = 20.000). The spectrum was detected simultaneously by the bolometer detector in combination with a lock-in amplifier and the photomultiplier. It can be seen that both spectra coincide perfectly. The experimental parameters were optimized only with respect to the depletion signal, the LIF was recorded additionally. By an analysis of the depletion signal (red curve), it is obvious that a signal could be resolved with at least one order of magnitude less intense than the electronic origin of pentacene. That means it should easily be possible to detect the loss of 10 or 100 helium atoms from 20.000 helium atoms with the bolometer detector. Consequently, it should be possible to detect a change in the energy flux of only 0.1 %.

Since the excitation volume of the dye laser is within the spectator angle of the bolometer, the signal might also be due to heating of the silicon diode by the fluorescence of the molecule and the stray light of the laser. In order to be able to exclude such an artefact, a quartz glass window was installed about 15 cm in front of the bolometer unit. It can block as well as unblock the helium droplet beam without blocking any fluorescence or stray light. By constant monitoring the depletion (induced by the excitation of pentacene), it could be shown that the depletion signal depends on the position of the quartz glass window. Blocking the droplet beam with the quartz glass window shuts down the depletion signal immediately. This experiment certainly demonstrated that the detected signal is not related to

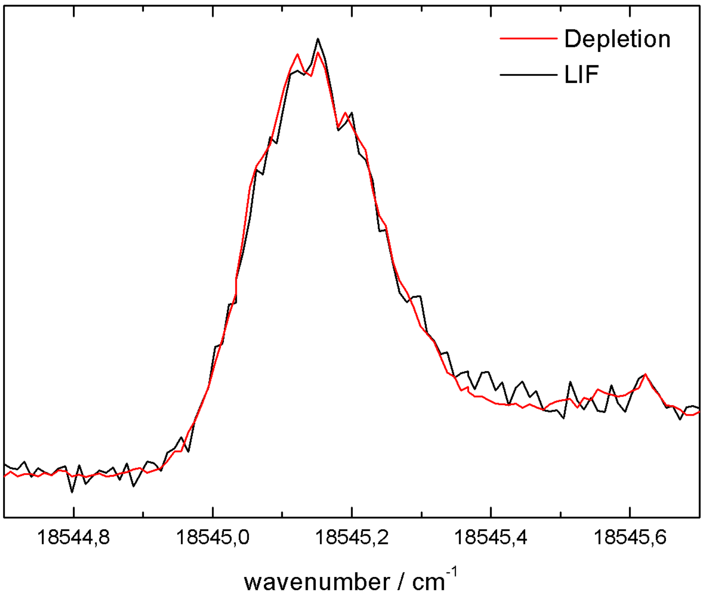

Fig. 5.7: LIF spectrum of pentacene inside superfluid helium droplets ($\bar{\mathrm{N}} \approx 20.000$) recorded simultaneously by the photomultiplier (black) and bolometer detector (red).

any radiation reaching the silicon diode of the bolometer and thus, only shows the depletion of the helium droplet beam induced by the excitation of the pentacene, which causes shrinking of the doped droplets.

Over all, these experiments show that the bolometer unit in combination with the lock-in amplifier is able to detect the loss of few ‰ in the energy flux. The bolometer was tested by the $S_1 \leftarrow S_0$ transition of pentacene which could be recorded with reasonable S/N ratio. By means of a beam shutter it is also possible to test and align the experimental setup independently of any dopant. Thus, this experimental setup fulfills the expected requirements. It should be possible to detect excitation spectra of iodine inside superfluid helium droplets.

6 Iodine in Superfluid Helium Droplets

6.1 Motivation

In this work the microsolvation of superfluid helium droplets was of main interest. By means of experimental methods, new data should be collected to provide a better empiric understanding for microsolvation as a consequence of the interaction between helium and a chromophore. For this purpose the chromophore should mainly fulfill two aspects, namely a simple molecular structure and the possibility of examining helium clusters from small up to huge mean sizes. These conditions were chosen in order to avoid the presence of numerous variants of configurations of the solvation complex. Both requirements can be achieved by the iodine molecule. Furthermore, in contrast to the rather large organic dopant species the iodine dimer allows for rotational resolution of electronic transitions. Thus, a direct access to the moment of inertia is possible which provides insight into the structure of the solvation complex. Finally, the data can be extended and compared by a similar analysis of the polar ICl molecule embedded inside superfluid helium droplets. All these spectroscopic data might stimulate theoretical simulations to enhance the understanding of the microsolvation inside the droplets.

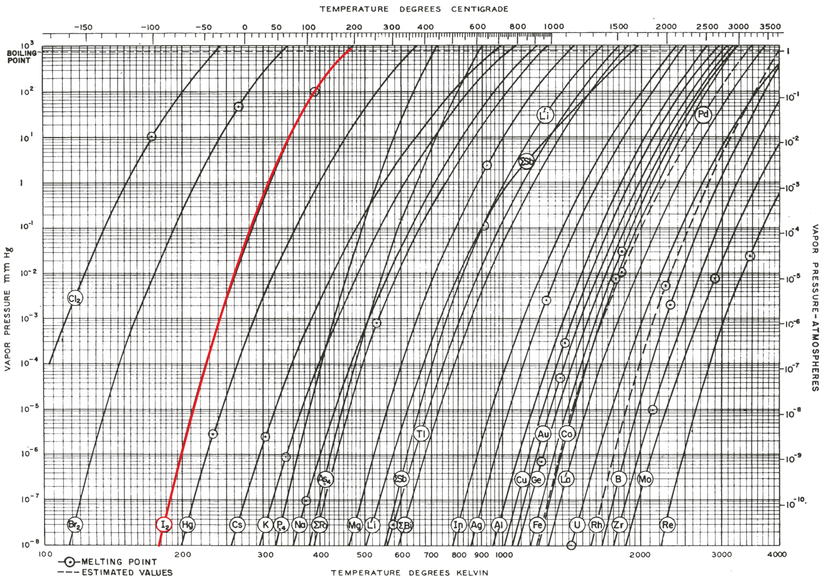

Fig. 6.1: Vapor pressure as a function of the temperature for iodine (red) and numerous other species (black) as indicated. The plot is taken from [155].

6.2 Introduction

Iodine is a rare element and belongs to the group of the halogens. It is the heaviest stable halogen and its molecular mass is 253.8 amu. At room temperature it is a greyish black solid showing a metallic shine. Besides, a vapor pressure of p = 0.33 mbar [154] can be measured. Figure 6.1 shows the vapor pressure of iodine over a wide range of temperatures [155]. Iodine sublimates into a noxious violet-pink I_2 gas consisting of diatomic molecules. The melting point can be found at a temperature of 113.7°C. It is only slightly soluble in water and can be dissolved in non-polar solvents such as hexane or carbon tetrachloride. It binds with many elements but it is less reactive than the other halogens like fluorine or chlorine [156]. The spectroscopic properties of iodine were examined a long time ago [157–163]. Since the induced fluorescence of iodine is intense and expands over a wide visible spectral range, it became an optical standard for calibration in the visible range. In 1978 Gerstenkorn and Luc published the absorption spectrum of iodine in the gas phase from 14800 cm^{-1} to 20000 cm^{-1} [18] and assigned every peak to a rovibronic transition of the iodine molecule. Besides, this work [19] also provides detailed spectroscopic data of iodine, whereas [20] also includes hyperfine splitting. Thus, the electronic absorption and fluorescence spectrum of iodine has long been an optical reference for molecular spectroscopy in the visible spectral range.

6.2.1 Spectroscopic Properties of Iodine

The visible absorption spectrum of iodine is caused by an electronic transition between the ground state $X^1\Sigma_g^+$ and the $B^3\Pi_{0u}$ excited state [164]. This transition is usually called X→B transition. Since this transition is accompanied by a spin flip, it has got only a week transition probability. This leads to a relatively long radiative lifetime of the excited B-state, which is in the order of several microseconds [164]. The dissociation energy is listed in [165] ($E_d = 12434.6$ cm^{-1}) and could be confirmed by [166] ($E_d = 12440.1$ cm^{-1}). Figure 6.2 shows a sketch of the potential energy curves of the X- and B-state as well as of the purely repulsive D-state [164].

The energy is plotted versus the internuclear distance r. For the bound X- and B-states the vibrational states are labeled v″ and v′, respectively. The rotational states, which are not shown in Fig. 6.2, are similarly assigned by double or single prime. The terms T of the different energetic levels of each electronic state can be calculated by the equation 6.1 [165].

$$T(\mathrm{v},\mathrm{J}) = T_e + G(\mathrm{v}) + F_{\mathrm{v}}(\mathrm{J}) \tag{6.1}$$

State	T_e	ω_e	$\omega_e x_e$	B_e
X $^1\Sigma_g^+$	0	214.57	0.6127	0.03735
B $^3\Pi_{ou}^+$	15641.6	128.0	0.834	0.02920

Tab. 6.1: The constants ω_e, x_e and B_v of the X-state and B-state of iodine in wavenumbers (cm^{-1}). The data was taken from [165].

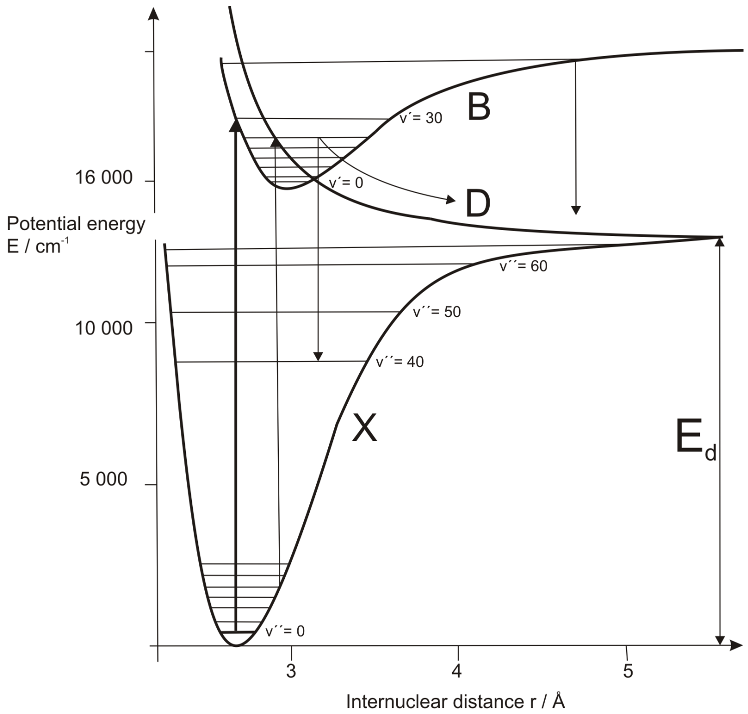

Fig. 6.2: Potential energy curves of the X-, B-, and D-state of diatomic iodine as a function of the internuclear distance (adopted from Ref. [164]).

In this equation, $G(\mathrm{v})$ represents the vibrational and $F_{\mathrm{v}}(\mathrm{J})$ the rotational contribution of the term values. T_e corresponds to the purely electronic transition.

$$G(\mathrm{v}) = \omega_e(\mathrm{v} + \frac{1}{2}) - \omega_e x_e(\mathrm{v} + \frac{1}{2})^2 + ... \tag{6.2}$$

$$F_{\mathrm{v}}(\mathrm{J}) = \mathrm{B_v J(J+1) - D_v J^2 (J+1)^2} + ... \tag{6.3}$$

The constants ω_e, x_e and $\mathrm{B_v}$ of the electronic ground state and the first excited one can be found in [165] and are listed in table 6.1. By means of the equation 6.4 the population of the quantum states can be calculated.

$$N_{\mathrm{i}} \propto g_{\mathrm{i}} \cdot \exp(-\frac{E_{\mathrm{i}}}{k_B T}) \tag{6.4}$$

In this equation N_{i} represents the population of the state, g_{i} the degeneracy of the state and E_{i} its energy. In case of vibrational levels the degeneracy is generally equal to 1 and in case of the rotational states it is equal to $(2\mathrm{J}+1)$ since each state with total angular momentum J splits up into 2J+1 degenerate sublevels. The calculated values of $G(\mathrm{v})$ in the X-state and their relative population at a temperature

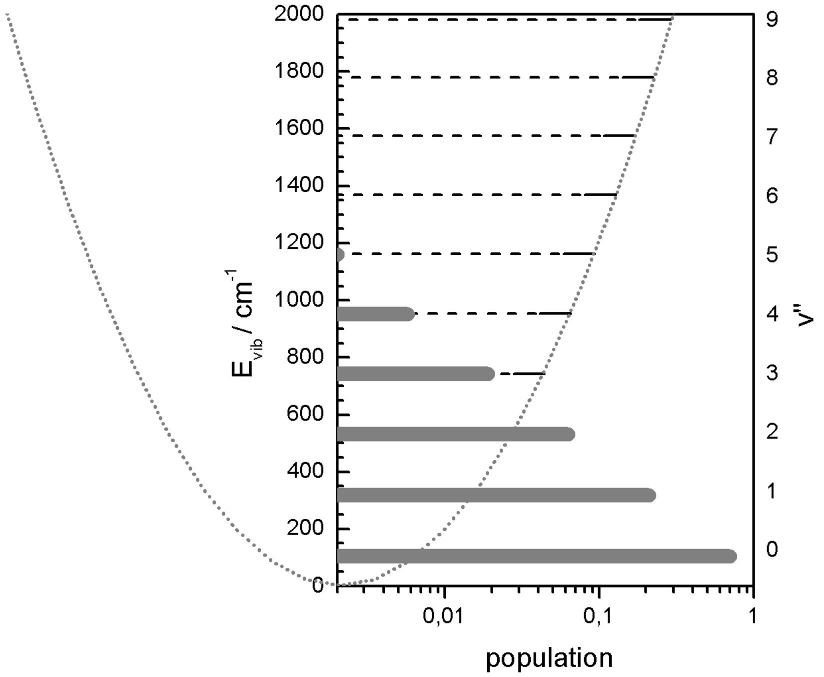

Fig. 6.3: Calculated energies of the vibrational levels in the X-state (left side) versus their population at T = −20°C. The quantum number v″ is shown on the right side.

of T = −20°C are shown in figure 6.3. Beside the ground state, only the first four vibrational states are significantly occupied at this temperature. The population of the remaining vibrational states lies below 1 %. In helium droplets only the ground state v″ = 0 is occupied at a temperature of 0.37 K. Figure 6.4 shows the calculated terms of $F_\mathrm{v}(\mathrm{J}) + G(\mathrm{v})$ in the X-state as well as the Boltzmann factors at T = −20°C and T = 0.37 K. The values at T = 0.37 K were scaled to the maximum at T = −20°C for better visualisation. The maxima for the two temperatures could be found at v = 0 and J″ = 49 as well as J″ = 2, respectively. The difference in the average value of the rotational energy at these temperatures can be calculated with the equation 6.3 and Eq. 6.4. At T = −20°C the rotational energy $< \mathrm{E}_\mathrm{rot} >$ equals 175.7 cm^{-1} and at T = 0.37 K a value of $< \mathrm{E}_\mathrm{rot} > = 0.24\ \mathrm{cm}^{-1}$ can be calculated. That leads to an energy difference of $< \Delta E > = < \mathrm{E}_\mathrm{rot}(253.15\ \mathrm{K}) > - < \mathrm{E}_\mathrm{rot}(0.37\ \mathrm{K}) > \approx 175.5\ \mathrm{cm}^{-1}$. Since

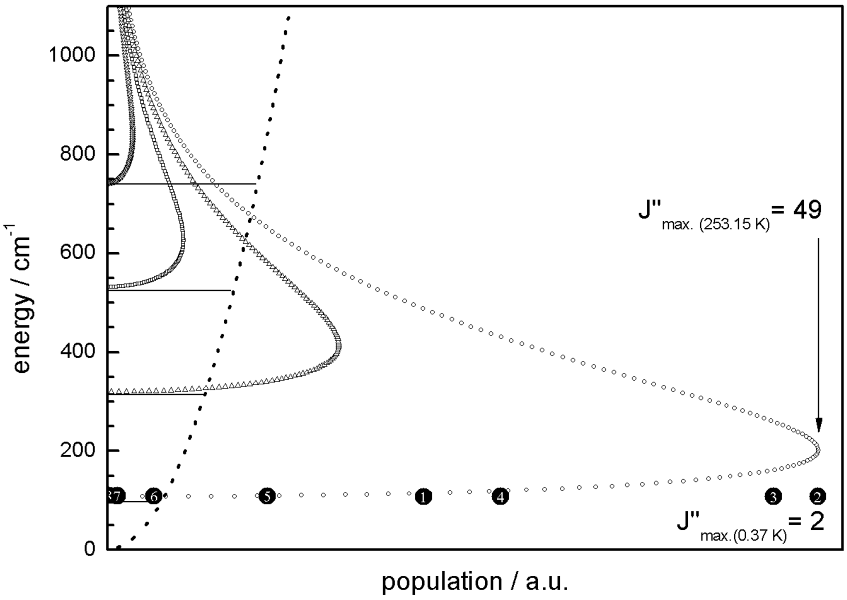

Fig. 6.4: Calculated rotational energies in the X-state for different vibronic levels as well as their relative population at T = −20°C and T = 0.37 K (large circles). The maxima of these curves could be found at J′ = 49 and J′ = 2. For a better visualisation, the population values at T = 0.37 K were scaled to the maximum at T = −20°C.

the rotational constants are small compared to *kT*, this value fits to the classical approximation. The calculation shows that about 175 cm^{-1} of the rotational energy have to be transferred into the droplet due to the pick-up process. After this energy transfer, the rotational energy of iodine inside the helium droplet can be neglected for the estimation of the total helium depletion due to electronic excitation.

Therefore, the electronic excitation of iodine inside a helium droplet starts in the X-state with the quantum numbers v″ = 0 and J″ ≤ 8. With the help of Franck-Condon factors the most probable transition can be determined. Figure 6.5 shows the envelop of Franck-Condon factors from v″ = 0, 1, 2, 3 (top to bottom) in the X-state to vibrational levels in the B-state as indicated by the v′ axis [18]. Due to

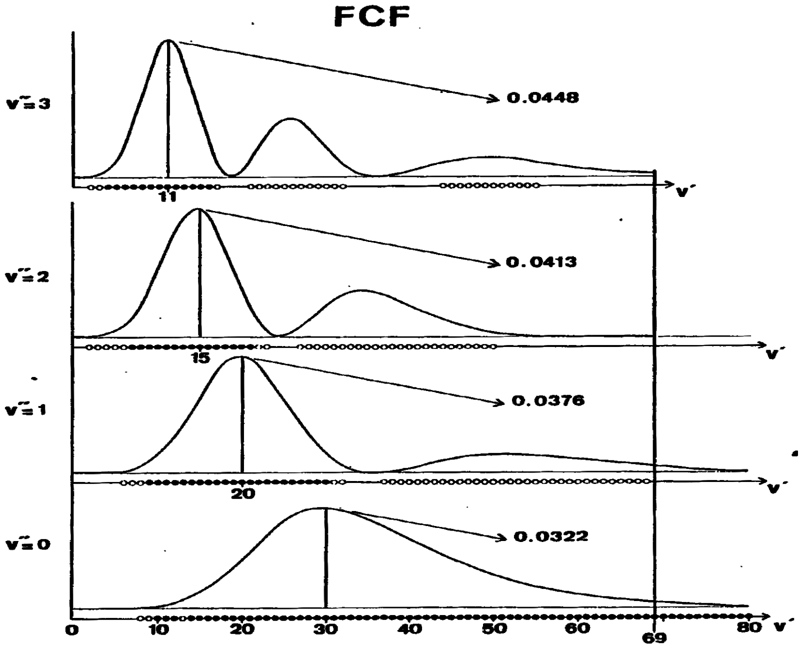

Fig. 6.5: Franck-Condon factors of the (v″,0), (v″,1), (v″,2) and (v″,3) progressions between the X- and B-state of iodine. The picture was taken from [18].

the very low temperature (0.37 K) inside the helium droplets, only the vibrational ground level v″ = 0 needs to be considered. In figure 6.5 it can be seen that the most intense transition can be expected for the transition from v″ = 0 in the X-state to v′ = 30 in the B-state. According to Eqn.s 6.1 to 6.3 and the molecular parameters shown in table 6.1 the corresponding transition energy equals about 18770 cm^{-1} for the isolated molecule. According to numerous examples in literature, the helium solvent shift of purely electronic transitions is in the order of 1 % of the gas phase value either to the blue or to the red. A similar relative shift of the vibrational frequencies can be neglected for this rough estimate. Inside superfluid helium droplets or any alternative dissipative environment the vibrational excess energy dissipates into the environment prior to radiative decay of the electronically excited state. Thus, the emission of iodine originates from B(v′ = 0) instead of from the initially excited vibronic level. By looking at the FCF factors of the (v″,7) ... , (v″,10) progressions shown in figure 6.6 it becomes obvious that the most intense transition shifts from v′ = 4 to v′ = 2. This means that the most intense signal should be

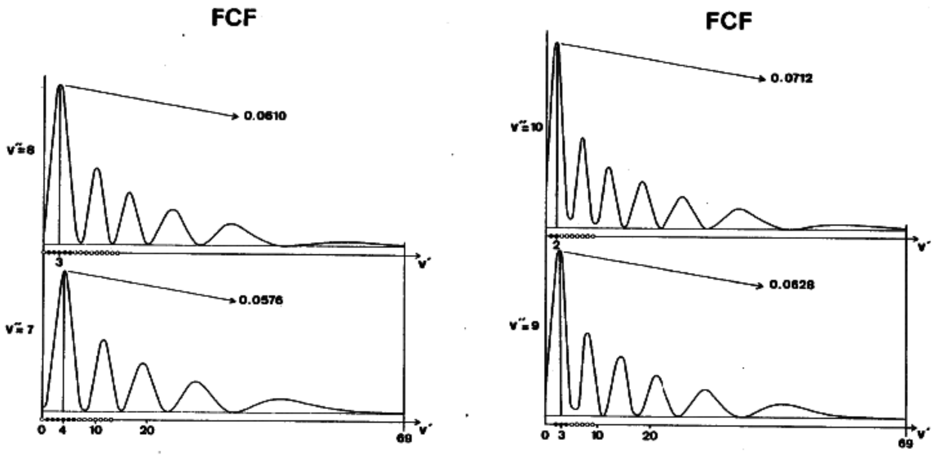

Fig. 6.6: Franck-Condon factors of the (v″,7), (v″,8), (v″,9) and (v″,10) progressions between the X- and B-state of iodine. The picture was taken from [18].

expected for the progression between the v′ = 0 level in the B-state and v″ = 12 level in the X-state. An energy of $\tilde{\nu}$ = 13055 cm^{-1} can be calculated for this transition in the gas phase. The solvation shift is expected to be about ±1%. Thus, choosing the maximum FCF for excitation into the B-state, 30 vibrational quanta of the B-state will dissipate prior to radiative decay and also about 12 vibrational quanta of the X-state post radiative decay. This means 3128 cm^{-1} and 2586 cm^{-1}, respectively. According to these conditions, the most probable X→B transition might be found in the range of 18582 cm^{-1} $\leq \tilde{\nu} \leq$ 18958 cm^{-1}, which leads to an emission signal between 745 nm and 762 nm. This expected red shift is the reason why previous attempts to detect iodine via fluorescence have failed entirely. Although detection at these wavelengths is problematic due to background radiation and reduced efficiency of the photomultiplier, one can profit from the large amount of energy dissipation by using the depletion method for recording the spectra of iodine. This has been accomplished by implementing a bolometer as monitor detector on the droplet beam axis.

As the rotationally and even hyperfinely resolved electronic transition of iodine in the visible range is perfectly documented and understood as exemplified in two spectroscopically highly important monographs, this molecule is the ideal candidate (among simple diatomics) for studying the influence of any host environment and, in the present case, the microsolvation in superfluid helium droplets. The challenge is to find optimized conditions for single molecule doping and afterwards the helium-mediated transitions of iodine.

All these experimental data and the derived results render iodine a perfect test molecule in contrast to other molecular systems. Its spectroscopic data in the gas phase is well known and it exhibits a simple geometric structure as homonuclear diatomic molecule. Thus, it should be easy to extract helium-induced spectroscopic features by comparison to gas phase spectra. Moreover, its easy structure most likely avoids numerous variants of solvation complexes, whereas its low heat capacity allows for the examination from small up to huge helium droplets. Its limited number of atoms is also favorable - it might ensure high level quantum chemical calculations to simulate the conditions of a helium solvation complex. This might lead to new aspects and thus, to a better understanding of the still not fully understood microsolvation inside the superfluid helium droplets.

The iodine used for the purpose of this study was purchased from Sigma Aldrich with a purity of at least 98 %. Thus, a further purification was not needed.

6.3 Experimental Details

6.3.1 Pick-up Conditions

For the spectroscopic analysis of iodine inside superfluid helium droplets the experimental conditions for single molecule doping are required. Since the pick-up process follows Poisson statistics (cf. chapter 2.2.2), the multi-doping of iodine cannot be avoided entirely. Consequently, optimum conditions mean a minimum of clusters at a maximum of monomers of the iodine molecule inside the helium droplets. The experimental parameters for this optimization procedure are the droplet size, tuned by the nozzle temperature, and the helium stagnation pressure as well as the partial

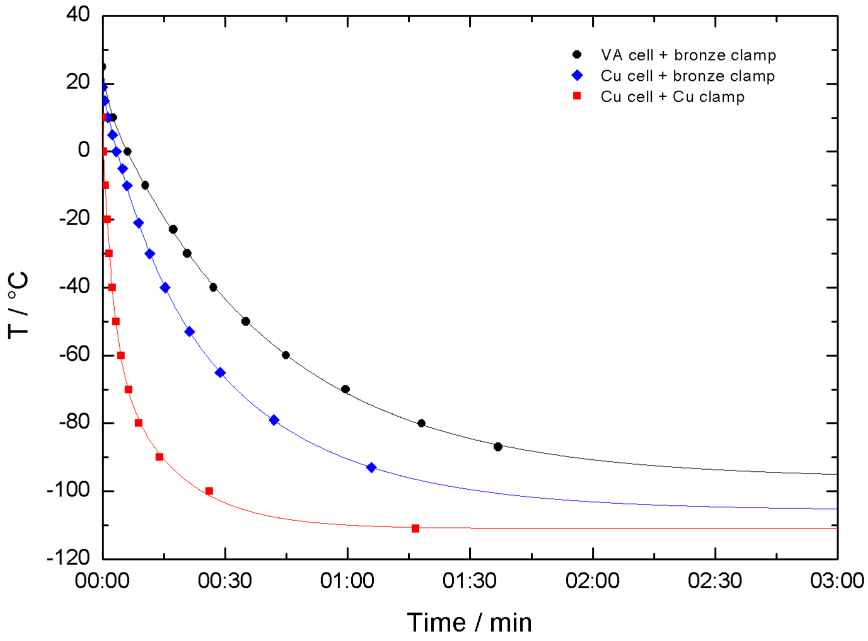

Fig. 6.7: Temperature profile of two different cryo cells in combination with two different connecting clamps.

pressure of iodine, tuned by the temperature of the pick-up cell. These parameters regulate the capture cross section of the I_2-droplet collisions and the particle density in the pick-up cell, which both can be found in the Poisson-distribution (cf. chapter 2.2.2 Eq.2.12). To achieve a single molecule doping, a pressure between 10^{-6} mbar to 10^{-5} mbar has normally to be established in the pick-up cell [4]. Since this pressure cannot be measured directly, it has to be controlled by the temperature of the pick-up cell. In figure 6.1 [155] it can be seen that such a vapor pressure can be found for iodine at a temperature between 200 K and 210 K. Since the temperature sensor might not touch the head of the pick-up cell, the measured cell temperature represents only an upper limit of the actual temperature of the iodine powder. To reach such low temperatures, the pick-up cell was modified as described in 3.1.1. The temperature performance of this setup can be found in figure 6.7. As it can be seen, the cell is enabled to reach minimum temperatures as low as −110°C. To

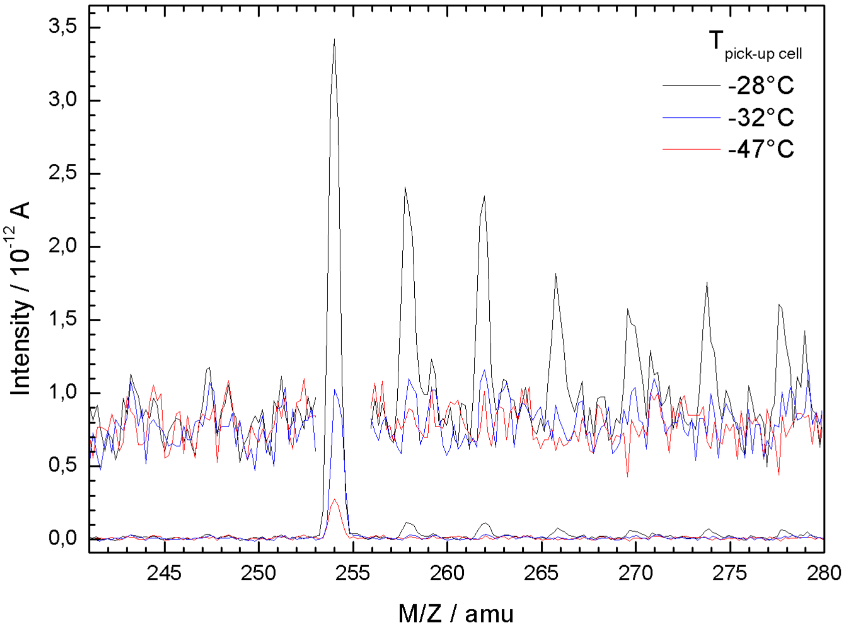

Fig. 6.8: Mass spectra of iodine molecules inside superfluid helium droplets ($\bar{N} \approx 20.000$ helium atoms) at different pick-up temperatures. The mass axis has been corrected by the factor 1.004.

obtain higher temperatures, a heating resistor was connected to the bottom of the pick-up oven.

For the analysis of the doping of the helium droplets the quadrupol mass spectrometer (cf. chapter 3.2.4) has been used. The mass spectrometer allows to record either the mass of the iodine dimer ion (253.8 amu) or the mass of the monomer ion fragment (126.9 amu). Moreover, it is possible to prove whether iodine is captured by the helium droplets due to the iodine-He$_N$ cluster signals at $[253.8+(4\cdot N)]$ amu and $[126.9+(4\cdot N)]$ amu. The ions of these clusters can be generated exclusively from iodine, which was ionized inside the helium droplet. Figure 6.8 shows a mass spectrum of the iodine-doped helium droplet beam showing the peak of bare, charged iodine molecules followed by clusters with an increasing amount of He atoms. Originally, the peak position was detected at 253 amu instead of 254 amu, which is a result of

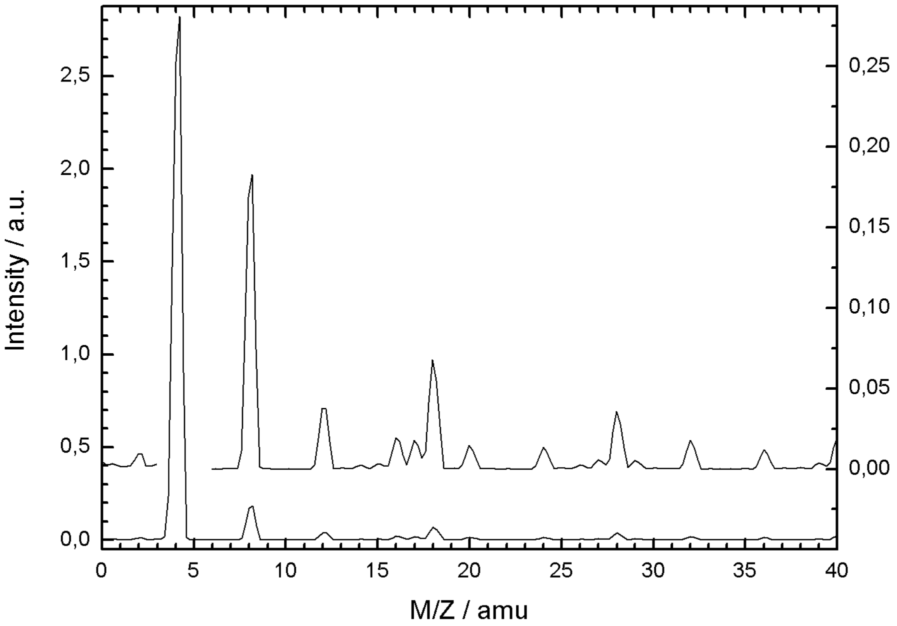

Fig. 6.9: Mass spectra of the pure superfluid helium droplet beam ($\bar{N} \approx 20.000$). Beside the helium$_\mathrm{N}$ cluster signals ($[4 + (4 \cdot \mathrm{N})]$ amu) water, nitrogen as well as helium can be seen.

poor calibration of the quadrupole mass filter in the high mass region. However, the mass scale can be recalibrated using the signals of the He-cluster ions which can be recorded from the pure droplet beam without any dopant species throughout the full mass range of 300 amu. They can also be seen in figure 6.8 with a very low S/N ratio. Figure 6.9 shows the mass spectrum of the undoped helium droplet beam at low masses. The peaks of the helium$_\mathrm{N}$ cluster signals at $[4 + (4 \cdot \mathrm{N})]$ amu can be found at the correct masses. Beside these signals, the peaks of H^+ and He^{2+} (2 amu), He^+ (4 amu), H_2O^+ (18 amu) and $N_2{}^+$ (28 amu) also fit very well to the expected position in the mass spectrum. The peak of the O_2^+ fragment coincides with the He_8 cluster at 32 amu. Figure 6.9 shows that the quadrupol mass filter delivers reliable results at low masses and has to be corrected only at high masses. For this reason the mass axis has been corrected by the factor 1.004. In case of higher masses the correction factor becomes more important than at the mass of He, He_2, H_2O or O_2. Analyzing the relative intensitiy values (shown in figure 6.8) of the different scans in the mass spectrum at 254 amu, values of $2.7 \cdot 10^{-13}$ A(−47°C), $1.0 \cdot 10^{-12}$ A (−32°C) and $3.4 \cdot 10^{-12}$ A (−28°C) can be found. The intensity rises by the factor 3. At the same temperatures the vapor pressure curve plotted in figure 6.1 predicts $2 \cdot 10^{-4}$ mm Hg, $6 \cdot 10^{-4}$ mm Hg and $2 \cdot 10^{-3}$ mm Hg, respectively. These values also show an increase by the factor 3, which is a similar increase as found in the mass spectrum. This indicates that the measured cell temperature represents the actual temperature of the iodine powder quite well. The iodine-He_N cluster signals could only be resolved with a reasonable S/N ratio at the highest cell temperature. At lower temperatures, the S/N ratio is in the order of these cluster signals. Due to the attenuation of the helium droplet beam during its way through the pick-up cell, the pure helium cluster signals at a mass of $[4 + (4 \cdot N)]$ amu only can be resolved with a poor S/N ratio (Fig. 6.8). It has to be mentioned that this effect could also be induced by a directed charge migration towards the iodine since the charge is stabilized at the more electrophile iodine. This could lead to a smaller amount of charged He clusters and thus, to a decrease of the cluster signals in the mass spectrometer.

In the next step, the signals between 115 and 155 amu in the mass spectrum were analyzed. They can be found in figure 6.10. In this mass range the iodine monomer fragment I^+ as well as the doubly charged iodine molecule I_2^{2+} can be detected at a mass of 127 amu. A distinction between these two signals is not possible in the mass spectrum. The signal increases at higher temperatures of the pick-up cell and cannot be found if there is no iodine inside the pick-up cell. The mass signal is followed by the iodine helium cluster peaks I-He_N at $[127 + (4 \cdot N)]$ amu in case of doped molecules. Thus, the iodine has to be solvated before it is detected at the mass spectrometer, which could already be seen at the He_N-I_2 mass peaks. The absolute intensities of the cluster peaks increase with the temperature and their relative intensities exponentially decrease with the mass. They can be resolved down

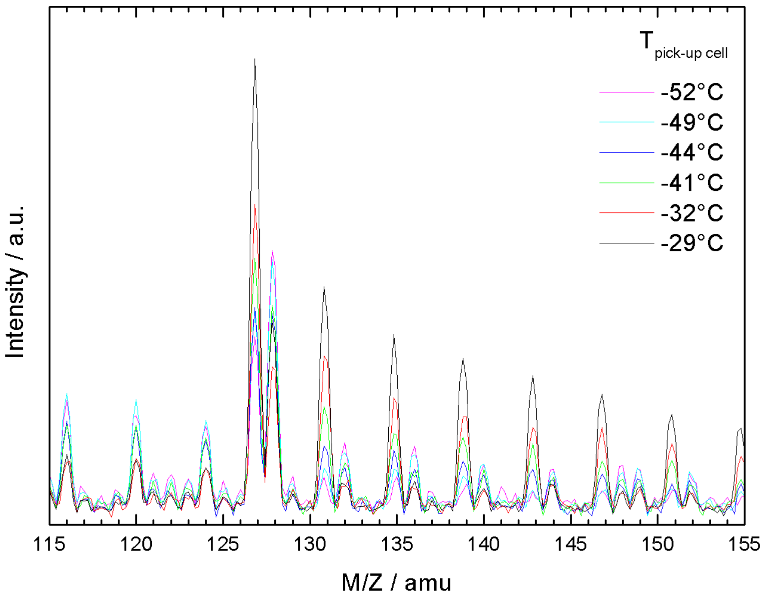

Fig. 6.10: Mass spectra of iodine monomeres as well as double-ionized iodine molecules inside superfluid helium droplets ($\bar{N} \approx 20.000$ helium atoms) at different pick-up cell temperatures. The mass axis has been corrected by the factor 1.004.

to −60°C. At lower temperatures the cluster signals disappear. This might indicate that the vapor pressure of iodine at cell temperatures below −60°C does not suffice for significant iodine doping of the helium droplets. Since the predicted vapor pressure should be reached at temperatures between 200 K and 210 K (−73°C to −63°C), it seems reasonable to assume that there might be a difference between thermal sensor and actual cell temperature although the intensities derived from figure 6.8 fit to figure 6.1. Nevertheless, it cannot be excluded that the I-He_N cluster peaks below −60°C remain hidden below the detection limit of the mass spectrometer. Beside these expected signals, two additional peaks could be found at the mass of the He_{32} cluster (128 amu) and at 149 amu. It is striking that these two signals also vanish in absence of iodine and that both can be detected independently from the droplet beam. Figure 6.11 shows the mass spectrum of iodine, the same mass spectrum

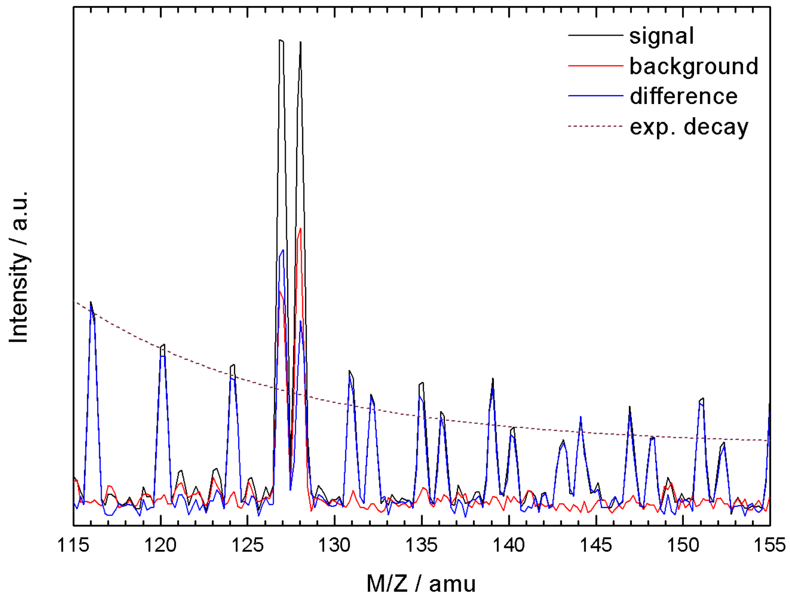

Fig. 6.11: Mass spectrum of iodine (black) inside helium droplets, the background signal (red) as well as the difference between both spectra (blue) at a pick-up temperature $T_{\text{cryo cell}} = -20°C$.

recorded without the helium droplet beam as well as the difference between both. This unequivocally demonstrates that a fraction of the 127 amu peak, most of the signal at 128 amu and the whole signal at 149 amu are all related to iodine molecules from the background gas inside the detection chamber. Most of the remaining fraction of the peak at 128 amu (blue plot fig. 6.11) belongs to the He_{32} cluster. It is not known that the He_{32} fits to a magic number of the helium clusters [38]. The intensity of the whole peak at 128 amu follows the temperature in reversed order similarly like the pure helium_N cluster signals at $[4 + (4 \cdot N)]$ amu, which can be seen at 116 amu, 120 amu and 124 amu in Fig. 6.10 and 6.11. The intensity of the bare helium cluster signals decreases exponentially with the mass. By looking at the intensities of the signals found at $\frac{M}{Z}$ of $[128 + (4 \cdot N)]$ amu in figure 6.11, it becomes evident that they fit well to the exponential decay of the pure helium clusters and thus, they have to be assigned to pure helium cluster signals. The absolute intensity of the He_N signals is maximal for the lowest pick-up temperature (cf. Fig. 6.10), which means a low vapor pressure of iodine inside the cryo cell and thus, a weak attenuation of the helium droplet beam inside the pick-up cell. Apart from that, the directed charge migration towards the iodine after the ionization might lead to a smaller number of charged helium clusters in this case. This could be responsible for the temperature-dependent decrease of the He_N cluster signals.

As the intensity of the 128 amu peak in the difference plot in figure 6.11 is higher than the intensity of the helium cluster signals at 120 amu and 124 amu and as the He_{32} cluster does not belong to the magic numbers, it has to be assumed that there is a small fraction of the 128 amu peak which is related to iodine inside the droplets. This part might be caused by the detection of an iodine monomer which has captured a hydrogen atom from a water molecule inside the droplets. However, the absence of a signal at 146 amu (128 amu + $M(H_2O)$) contradicts this assumption. Nevertheless, the intensity of the peak at 128 amu depends on three different contributions, namely iodine from the background gas, iodine inside the helium droplet and the pure helium cluster signals. All these three contributions show a different temperature dependence. The contribution of the background gas as well as the contribution of iodine inside the droplets both increase at higher pick-up temperatures, whereas the pure helium cluster signal decreases. The helium cluster signals at $[128 + (4 \cdot N)]$ amu from the contribution due to iodine inside the droplets cannot be detected. Since the contribution of iodine to the 128 amu signal inside the droplets seems to be very small, the cluster signals at $[128 + (4 \cdot N)]$ amu might be hidden by the pure helium cluster signals.

Figure 6.12 shows the normalized intensities of the mass peaks of a helium cluster (116 amu), the iodine monomer (127 amu), the peak at 128 amu as well as at the mass of a helium iodine cluster (131 amu). It can be seen that the iodine-related signals at 127 amu and 131 amu do increase with the pick-up temperature, whereas the bare helium droplet signal as well as the signal at 128 amu decrease. It can be

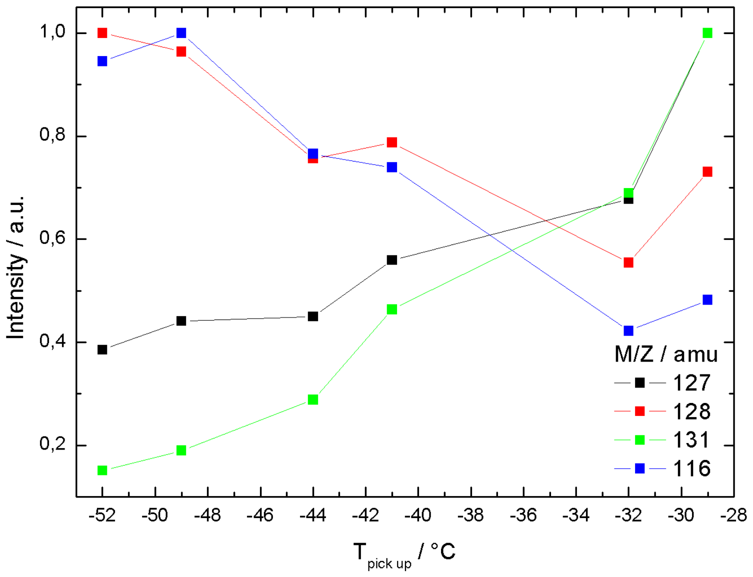

Fig. 6.12: Normalized intensities of the mass peaks of a helium cluster (116 amu), the iodine monomer (127 amu), the peak at 128 amu as well as at the mass of a helium iodine cluster (131 amu).

noted that there is an increase in all signals from -32°C to -28°C. This might be due to a thermal drift in the experimental parameters during operation. It can also be seen that the red curve which is related to the solvated iodine seems to differ most from this trend. This could indicate that the contribution to the 128 amu signal related to iodine inside the helium droplets becomes large enough to be detectable.

If one compares both plots (Fig. 6.8 and Fig. 6.10), it seems justified to analyze the iodine monomer signal as well as its helium cluster signals instead of the dimer peak at 253 amu. Thus, reliable results on the pick-up process of iodine inside the helium droplets can be ensured.

In the next step the influence of the helium droplet size on the pick-up process was investigated by means of varying the nozzle temperature. Figure 6.13 shows

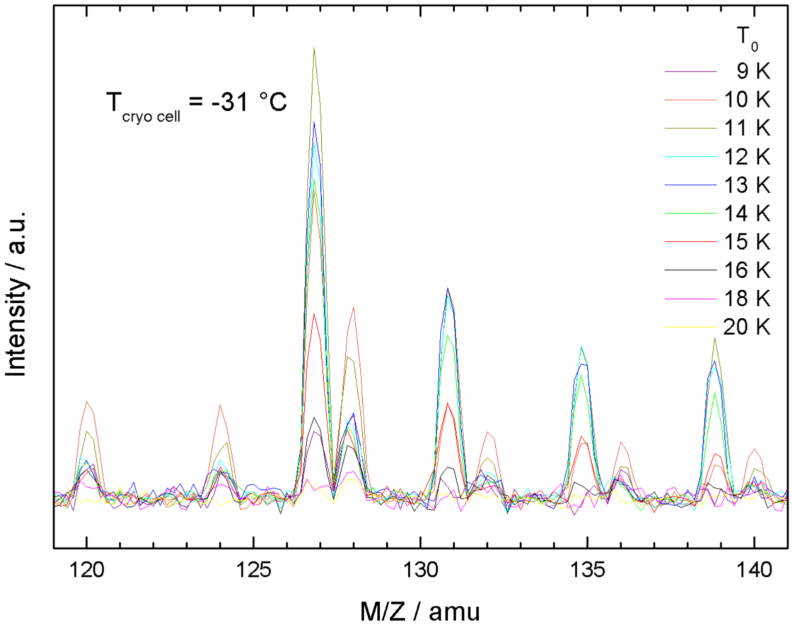

Fig. 6.13: Mass spectra in the range of the I^+ signal of iodine inside helium droplets at a pick-up temperature $T_{\text{cryo cell}} = -31°C$ for different mean droplet sizes $(4 \cdot 10^2 \leq \bar{N} \leq 3 \cdot 10^7)$.

the mass spectra in the range of the iodine monomer signal recorded at a pick-up temperature $T_{\text{cryo cell}} = -31°C$. It can be seen that the nozzle temperature influences the iodine signal at 127 amu, the iodine helium$_N$ clusters as well as the pure He_N cluster signals. The temperature profiles of the pure helium cluster signals are not identical to the temperature profile of the iodine signal (127 amu) and the accompanying I-He_N clusters $[127 + (4 \cdot N)]$ amu. While the first peaks show a maximal intensity at 10 K, the latter ones show maximal intensity at 11 K for bare iodine (127 amu) and between 11 K and 13 K for the I-He_N clusters ($[127 + (4 \cdot N)]$ amu).

These experiments show that both temperatures, T_0 as well as $T_{\text{cryo cell}}$ need to be optimized simultaneously. Therefore, the pick-up efficiency has been examined depending on both temperatures. Here the I-He cluster at 131 amu was chosen because it discriminates against gas phase iodine and originates exclusively from iodine inside helium droplets. Moreover, it is not affected by the pure helium$_N$ cluster peaks. Thus, its intensity has been used as a measure of the pick-up efficiency. Still, although this is an appropiate parameter of the pick-up efficiency, it can only be seen as an approximation of the single molecule doping probability. It is not selective for the nascent cluster size but may carry contributions of I-He ion fragments from any neutral $(I_2)_N$ cluster inside a helium droplet. The nozzle temperature was varied between $7.2\ K \leq T_0 \leq 20\ K$ and the temperature of the cryo cell between $-70°C \leq T_{cryo\ cell} \leq -10°C$. The stagnation pressure of the droplet source was kept fixed at 20 bar. The results of these measurements are summarized as two-dimensional contour plot in Fig. 6.14. This plot shows its maximum at a nozzle temperature around 11 K and a cryo cell temperature around −20°C. The discrepancy between this temperature and the expected temperature of about −70°C (predicted for a vapor pressure between 10^5 mbar and 10^6 mbar for single molecule doping conditions) leads to the conclusion that either the measured pick-up temperature does not match the actual temperature or the I-He cluster peak at 131 amu might be massively fed from higher $(I_2)_N$ clusters. This could lead to an overestimation of the actual temperatures needed for single molecule doping. Due to this result another method was used to obtain more information about the pick-up conditions of iodine inside helium droplets.

For this purpose the attenuation of the helium droplet beam by the iodine vapor pressure was examined. The intensity of the helium droplet beam can be easily observed by monitoring the intensity of the helium dimer signal at the ratio $\frac{M}{Z} = 8$ amu. This signal results from electron bombardment ionization accompanied by fragmentation of the helium droplet. When the pick-up cell is crossed, the intensity of the helium droplet beam decreases with increasing vapor pressure inside the pick-up unit. This effect was already visible in figures 6.10 and 6.12, where the pure helium cluster signals (e.g. $\frac{M}{Z} = 116$ amu) increased upon reduction of the particle density

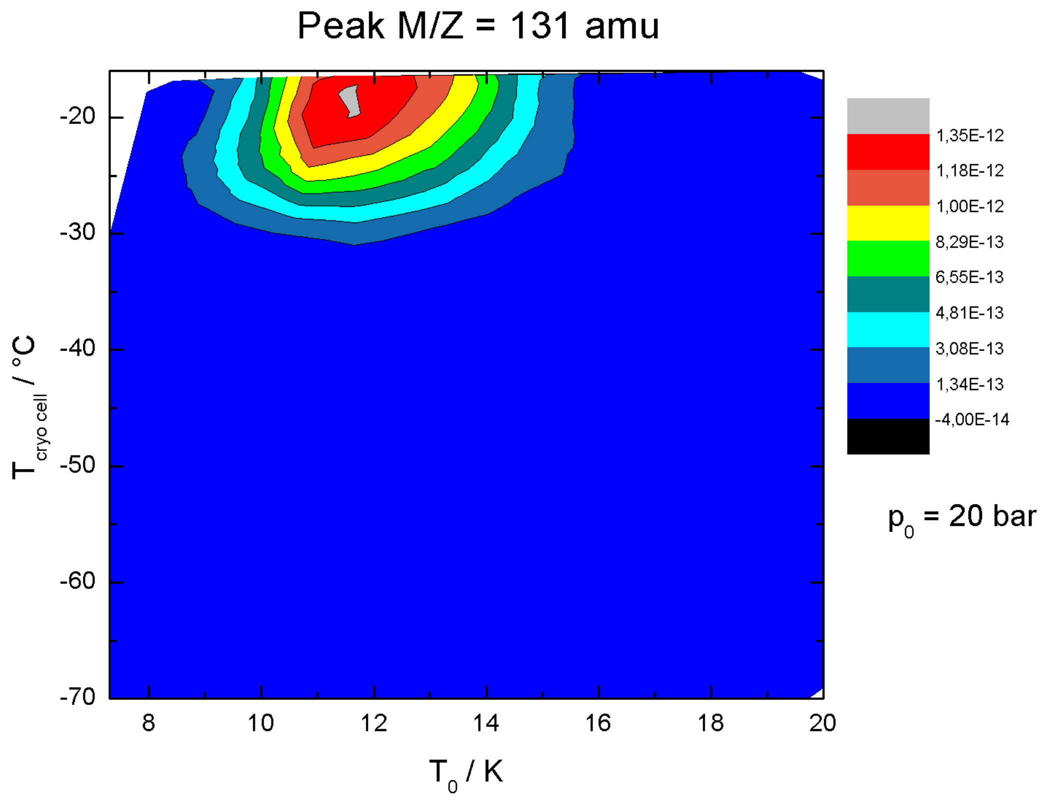

Fig. 6.14: Intensity of the signal at $\frac{M}{Z}$ = 131 amu determined at different nozzle temperatures T_0 and cryo cell temperatures $T_{\text{cryo cell}}$.

in the pick-up unit (by reducing $T_{\text{cryo cell}}$). Thus, the signal of the He dimer ion was monitored for different pick-up temperatures $T_{\text{cryo cell}}$. This method is not affected by multi-doping of the droplets. Figure 6.15 shows the intensity of the signal at $\frac{M}{Z}$ = 8 amu as a function of the temperature of the pick-up cell (blue graph) as well as when successively alternating heating and cooling of the cell. The dashed lines mark different levels of attenuation. As already mentioned above, the intensity of the $\frac{M}{Z}$ = 8 amu signal depends on the vapor pressure of iodine inside the pick-up unit and thus, on the temperature of the cell. As a rule of thumb the pick-up conditions should be close to optimum for single molecule doping if the intensity of the helium droplet beam is reduced to 80 %. Since this is only a rough approximation, it is used as first step which provides reasonable conditions to search for the monomer

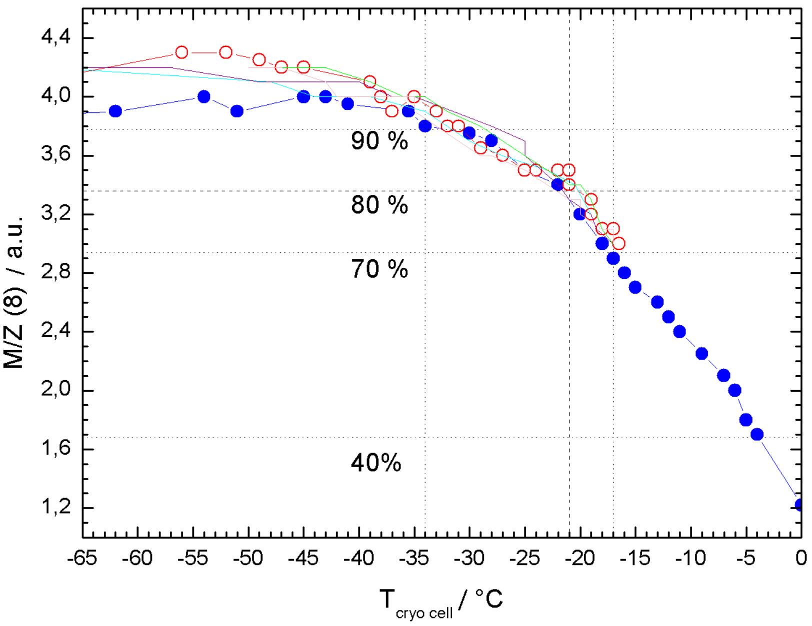

Fig. 6.15: Intensity of the $\frac{\mathrm{M}}{\mathrm{Z}}$ = 8 amu determined at different cryo cell temperatures $\mathrm{T}_{\text{cryo cell}}$. The dashed lines mark different levels of attenuation. An attenuation of about 80 % can be found at a temperature of $\mathrm{T}_{\text{cryo cell}} \approx -21°\mathrm{C}$.

signal of the dopant. This estimation does not include the size of the dopant nor of the helium droplets and the maximal intensity $\mathrm{I}(8)_{\text{max}}$ cannot be determined exactly. Nevertheless, by looking at figure 6.15 it can be noted that the temperature $\mathrm{T}_{\text{cryo cell}} \approx -21°\mathrm{C}$ fulfills an attenuation of the signal down to 80 %.

This value fits to the pick-up cell temperature $\mathrm{T}_{\text{cryo cell}} - 20°\mathrm{C}$, which was found in the contour plot figure 6.14. Thus, both procedures came to the same result. By this fact it seems reasonable to assume that a practical temperature around $\mathrm{T}_{\text{cryo cell}} \approx -20°\mathrm{C}$ should provide adequate conditions for single molecule doping and thus, a good starting point for recording depletion spectra of iodine in helium droplets.

6.3.2 Mean Size of Helium Droplets / Depletion

On account of the unique cooling properties of superfluid helium droplets it has to be stated that the mean size of the droplets will shrink in case of the pick-up of each system that couples to the cryogenic helium transferring energy into the droplet. Thus, the energy that is brought into the system has to be considered. In this regard it has to be taken into account that in case of the spectroscopic examination of iodine its internal energy, namely the vibrational excitation in the B-state and the various vibrational energies which are occupied in the X-state after radiative decay, will dissipate into the helium droplets. The internal energy of the iodine, which dissipated during the pick-up process, can be estimated by the Equipartition theorem. In the thermal equilibrium at the temperature T this theorem predicts that each degree of freedom contributes $E = \frac{1}{2} \cdot k_B \cdot T$ to the average energy [42]. Since iodine is a diatomic linear molecule, there are two rotational, one vibrational[1] degree of freedom plus three different translation coordinates. At T = −20°C about 70 % of the iodine molecules can be found in the vibrational ground state of the X-state (cf. Fig. 6.3). The internal energy due to the occupied vibrational levels can be calculated by the following equation:

$$< E_{vib} >= \sum_{\mathrm{v}=0}^{\mathrm{v}_m} N_v \cdot (E(\mathrm{v}) - E(0)) \tag{6.5}$$

The calculated rotational energy in chapter 6.2.1 matches to the approximation by the Equipartition theorem ($k_B \cdot T = 175.8\ \mathrm{cm}^{-1}$). Thus, the estimated total internal energy leads to a value of about $\frac{5}{2} \cdot k_B \cdot T + < E_{vib} > \hat{=} 530\ \mathrm{cm}^{-1}$. As mentioned in chapter 2.2.1 about 5 cm^{-1} [78, 79] are needed for the evaporation of each helium atom. That means that the mean droplet size decreases by only approx. 100 helium atoms upon the pick-up of a single I_2 molecule provided by a gas phase over a sample kept at −20°C. Thus, iodine can be doped into helium droplets with a mean droplet size of less than 10^3 helium atoms. The mass of the helium droplets is increased by the iodine molecule after the pick-up process. At an estimated velocity of 300 $\frac{m}{s}$

---

[1] The vibrational degree of freedom contributes $k_B T$ (potential as well as kinetic energy).

each iodine molecule increases the kinetic energy of the droplets by a value of about 950 cm^{-1}.

As discussed above (cf. chapter 6.2.1) the electronic excitation of I_2 via the X-B-transition is followed by one radiative and two energy dissipative steps to return to the ground state. By modulating the excitation laser the dissipative steps are detectable by the bolometer. The reduction in the energy flux caused by the dissipation of vibrational energy can be estimated by the following considerations: The rotational energy at T = 0.37 K can be neglected. Each helium atom causes a reduction of the energy flux by the value $\Delta E \approx 15\ \mathrm{cm}^{-1}$, whereas

$$\Delta E = \frac{m}{2} \cdot v^2. \tag{6.6}$$

In equation 6.6 m is equal to the mass of a helium atom ($m = 4.002 \cdot 1.6605 \cdot 10^{-27}$ kg) and v is the velocity of the helium droplets. The velocity of the droplets is about 300 $\frac{m}{s}$ [65]. The number of evaporated helium atoms can be estimated by equation 6.7

$$N = \frac{\Delta E_{vib}}{5\ \mathrm{cm}^{-1}}. \tag{6.7}$$

In this case, ΔE_{vib} is equal to the vibrational energy in the X-state as well as in the B-state, which dissipates into the helium droplets. This value can be approximated by the usage of the gas phase data discussed in chapter 6.2.1 leading to the value of $\Delta E_{vib} \approx 5915\ \mathrm{cm}^{-1}$. That means that each helium droplet should release about N = 1183 helium atoms upon electronic excitation of iodine via the optimum FCF. According to Eqn. 6.6 the 1183 helium atoms correspond to an energy flux of 17800 cm^{-1}. Compared to the energy flux of the doped helium droplet with an average mass of roughly 19900 helium atoms and one iodine molecule which amounts to $3 \cdot 10^5\ \mathrm{cm}^{-1}$, this depletion is about 6 %, which is easily detected. The depletion method used to be applied for recording IR spectra of molecules with dissipation of far less than half the energy released by the iodine molecule [116, 167]. Thus, the conditions appear to be ideal for recording electronic spectra of iodine via depletion by means of a bolometer.

6.4 Results

Doubtlessly, the data presented in this chapter has shown that the helium droplets could be doped with iodine molecules. However, since this was proven by the iodine helium cluster peaks in the mass spectra, it was not possible to selectively detect the iodine monomere. By different experiments pick-up conditions for single molecule doping of the droplets could be estimated. They revealed a higher value for the temperature of the pick-up cell of $T = -20°C$ than estimated by the vapor pressure of iodine at 10^{-5} mbar to 10^{-6} mbar ($T \approx -70°C$). This could be seen as an indication that not only single molecule doping occurred, which cannot be excluded by the analysis of the helium iodine cluster signals in the mass spectra alone. Still, since the attenuation experiments of the helium droplet beam led to identical experimental parameters for single molecule doping as observed from the mass spectrometer, it seems most likely that the temperature read from the thermosensor does not fit exactly to the temperature extracted from the vapor pressure plot given in Fig. 6.1. Since iodine has not been studied yet inside helium droplets, there is no spectroscopic data known. So far, the entire number of molecules investigated by means of electronic spectroscopy have revealed a solvent shift of the pure electronic transition of about ±1 % [4] of the corresponding gas phase value. The solvent shift observed in the electronic transition reflects the difference in the stabilization energy of the two electronic levels involved in the transition. Without exact knowledge one needs to search for molecular transitions over a reasonable frequency range. By means of equation 6.2, the spectral spacing of the band heads can be estimated to be around 80 cm^{-1}. Thus, within the spectral range of 100 cm^{-1} at least one band head of a vibronic transition should be found.

Moreover, it is not known in which way the high vibrationally excited ($v' = 30$) iodine molecules are coupling to the helium droplet. It might affect the lifetime of the excited states and thus, it cannot be excluded that the line width is dramatically affected by the helium environment. Depending on the iodine helium coupling, it is possible that the line width changes in both ways, narrowing or broadening.

Because of this uncertainty also different excitation energies were carried out to address different vibronic transitions of iodine.

excitation energy cm^{-1}	v'	spectral range cm^{-1}	FCF a.u.	$T_{\text{cryo cell}}$ °C
18150	33	+60	0.032	-20
18100	33	+100	0.032	-60 / -50 / -30
18100	33	+140	0.032	-10
18100	33	+85	0.032	-20
18090	32	+90	0.032	-15
17000	22	+160	0.026	-30
16415	17	+140	0.014	-12
16390	17	+140	0.007	-30 / -25
16000	13	+180	0.004	-12

Tab. 6.2: Overview of the experimental conditions of the spectroscopic examination of iodine inside superfluid helium droplets ($\bar{N} \approx 10^4$ helium atoms). The FCF were taken from [18].

Table 6.2 presents an overview of the different examined spectral ranges as well as the different pick-up temperatures. The mean droplet size $\bar{N}$ of the helium droplets was kept fixed at 20000 helium atoms. The spectra were recorded with a resolution of 50 MHz ($\approx 0.0016\,cm^{-1}$). The laser power varied between 300 mW and 700 mW depending on the wavelength. The laser beam was focused by a home-made Keppler telescope into the detection chamber. Within the examined spectral range listed in table 6.2 no signal of iodine could be detected in the bolometer. Only a constant noise was recorded. This result only leaves room for speculations. One explanation could be that the experimental conditions like pick-up temperature or droplet size did not fit to single molecule doping. However, the consistency of two experimental observables clearly speak for appropriate doping conditions for single molecule doping. Another point might be the excitation frequency which did not match a transition of iodine molecules when solvated inside helium droplets. However, because of the high amount of the innumerable rovibronic transitions in the visible spectral range it seems rather unlikely that not even one of these transitions could be detected as a signal in the bolometer. Finally, it cannot be excluded that the highly excited, vibrational modes prevent the iodine from spectroscopic detection while the transitions between lower vibrational modes are suffering from a lack of intense FCF. But this conclusion does not seem reasonable, since many experiments examining rotationally resolved IR spectra of different substances can be found in literature [4]. All these data showed a solvent shift in the order of or less than 1 % of the transition frequency as well as a slight line broadening compared to the corresponding gas phase data.

All indications provide evidence that for the helium droplets generated at a nozzle temperature of 11 K and a stagnation pressure of 20 bar single doping conditions have been found. Nevertheless, some of the spectra have been recorded for particle densities in the pick-up unit significantly reduced or increased compared to the optimum conditions found for single molecule doping. The proper functioning of the bolometer and its signal detection via a lock-in amplifier has been proven by recording the electronic origin of pentacene simultaneously via fluorescence and depletion (chapter 5 Fig. 5.6). It showed that the bolometer should be able to register the loss of only 100 helium atoms from 20.000 helium atoms.

Unfortunately, the very promising conditions of iodine for the detection of rotationally resolved depletion spectra have not been fulfilled. Instead of providing new data for the discussion of a long existing problem of molecular spectroscopy in helium droplets only additional questions arose.

7 Discussion

Since the depletion spectroscopy was an essential precondition for the aim of this study, the apparative modification of the helium droplet machine played a key role. It could be shown in chapter 3.2.3 that the integration of a commercial bolometer into the experimental setup could be achieved successfully. This was demonstrated by the electronic spectrum of pentacene recorded simultaneously via fluorescence excitation and depletion by means of the bolometer. The depletion signal was even superior in the signal-to-noise-ratio than the fluorescence signal.

In the course of this work the microsolvation of superfluid helium droplets was examined by means of high resolution spectroscopy. The experimental results were discussed with respect to the empirical model explaining the microsolvation of molecules in superfluid helium droplets. It proposes a non-superfluid helium solvation layer covering the surface of the dopant molecule. By means of this model any helium-induced substructure resolved in electronic spectra can be empirically explained. Although none of the helium-induced spectral features refute this empirical model, an unambiguous assignment of the induced spectroscopic fine structures is often not possible.

Up to now numerous experimental data on different spectroscopic examinations in superfluid helium droplets is available in literature but in spite of all efforts a quantitative modeling or simulation of spectra is still not possible. That is primarily due to the fact that the theoretical approach to such many-particle systems dissolved in a quantum fluid is a great challenge. To promote such theoretical activities as well as the quantitative understanding of microsolvation in superfluid nano droplets the helium-induced spectral features should be examined for prototypical dopant species. The unique properties of iodine render this molecule special and the effect of the helium solvation complex should be easily understandable due to the simple molecular structure of iodine. Its spectroscopic behavior in the gas phase is well documented and beside the electronic excitation coupling to the helium environment, its rotational degree of freedom should lead to rotationally resolved spectroscopic data. By this, a direct structural analysis of the helium iodine complex can be achieved.

In the beginning of the implementation of molecular spectroscopy to the helium droplet beam technique, attempts to detect iodine via fluorescence have failed entirely [168]. The fluorescence of iodine in helium droplets is expected to occur in the IR region, where the detection is problematic due to background radiation and reduced efficiency of the photomultipliers on hand. For this reason one has to use the large amount of energy dissipating from the electronically excited iodine molecule by using the depletion technique for recording excitation spectra of iodine in helium droplets.

Unfortunately, the spectroscopic examination of iodine conducted in this work did not lead to any depletion signal. The absence of any spectroscopic structure of iodine inside helium droplets forms a contrast to any experience with depletion spectroscopy in helium droplets. A detailed investigation of the conditions for doping helium droplets with iodine molecules clearly reveals the successful doping of the droplet. The investigation provides strong evidence that single iodine doping is favoured at the parameters determined in this project. Since the depletion of the helium droplets due to the excitation of pentacene could be recorded in the range of the ZPL of pentacene by the bolometer, it is ensured that the detection system is sensitive to detect at least a change in the energy flux of only 0.1 %. In case of iodine a depletion of about 6 % of the energy flux is expected, which means that the depletion due to an electronic excitation of iodine should lie far above the detection limit of the bolometer.

Apparently, the unexpected result of no iodine signal in the excitation spectrum reveals unknown features accompanying electronic excitation of iodine molecules in helium droplets. One point might be an extremely short lifetime of the excited state due to an efficient coupling to the helium and thus, the spectroscopic signals remain hidden due to massive line broadening. Anyway, an empirical description of a mechanism that is responsible for the lack of any iodine signal in helium droplets is missing so far. However, the experimental observation underlines the necessity for continuing the work on electronic spectroscopy of molecules in helium droplets. Further experiments, influencing the experimental conditions inside the droplets might be of interest for obtaining any spectroscopic signals of solvated iodine. This could be done by providing iodine and a second dopant, e.g. argon or water to the helium droplets. The pick-up conditions of the second dopant could be optimized in combination with a well-studied chromophore e.g. phthalocyanine. This might influence the dynamic and structure of an iodine helium complex in such a way that the excitation spectrum remains visible.

The examination of phthalocyanine presented in chapter 4 clearly demonstrated that the dynamic process of the helium mediated vibrational predissociation [141] of the van der Waals cluster Pc-Ar_1 inside the droplets does not occur and a revision of the previous interpretation is demanded. This result was accompanied by the observation that phthalocyanine in helium droplets can be excited far off-resonantly to any vibronic transition over a wide spectral range. The analysis of the dispersed emission signals of off-resonantly excited Pc revealed (in addition to the dual emission) new spectral features close to the electronic origin. These sharp signals indicate surprising dynamic processes which can only be explained by the relaxation via a cascade of metastable configurations of the helium solvation complex. These results show a direct observation of additional, metastable configurations of the solvation complex.

While vibrational excess excitation energy clearly drives the relaxation of the helium solvation complex, the direct excitation of the solvation layer via the PW assigned to van der Waals modes of the non-superfluid helium solvation layer did not result in a promotion of the relaxation process. This is in contrast to corresponding investigations for Mg-Pc and the Pc-Ar cluster [104]. Both observations show that in the case of phthalocyanine the assignment of these signals to the phonon wing has to be questioned.

Finally, a direct radiative decay without previous dissipation of the vibrational energy has been observed exclusively for the lowest vibronic excitation. In this case, most of the radiative decay follows the pathway $\Delta \mathrm{v} = -1$ instead of the expected $\Delta \mathrm{v} = 0$ transition. Only few excited molecules decay via dissipation of the vibrational energy prior to radiative decay. A similar observation could only be found for the HF molecule inside helium droplets. In this case, the vibrational energy is too large and thus, it cannot couple to the helium environment [169].

All these spectroscopic observations of phthalocyanine also raise legitimate doubts about the assignment of experimentally observed signals to features predicted by the model of the microsolvation. Even though there are no experimental observations which disprove the empirical model for the solvation in helium droplets, an unambiguous assignment of the induced spectroscopic structures is often not possible. Thus, different explanations can be found for the same experimentally observed phenomena, but by means of simple fluorescence excitation and dispersed emission spectra it is impossible to assign the various helium-induced signals unambiguously. Only by means of pump-probe experiments it should be possible to provide a clear distinction between zero phonon lines and the excitation of van der Waals modes of the helium dopant complex. Moreover, wavelength-selective detected excitation spectra could provide new information on the off-resonantly excited emission signals of Pc in superfluid helium droplets.

Over all, both projects, the spectroscopic examination of iodine and phthalocyanine, showed that the microsolvation inside superfluid helium droplets is still not completely understood. The empirical model of a non-superfluid helium layer around the chromophore can explain most phenomena. But there are still plenty of questions that cannot be answered yet. For example, the assignment of signals must be critically reviewed. Beside the phonon wing, the existence of different solvation complexes has to be taken into account. The typical spectroscopic criteria like saturation behavior, stokes shift in the emission spectra, relaxation probability of the solvation complex etc. do not suffice to distinguish between van der Waals modes of the Pc-He complex and different variants of this solvation complex. Further examinations, theoretical as well as spectroscopical, are needed to understand microsolvation in superfluid helium droplets quantitatively.

Bibliography

[1] S. Goyal, D. L. Shutt, and G. Scoles. Vibrational Spectroscopy of Sulfur Hexafluoride Attached to Helium Clusters. *Physical Review Letters*, 69(6):933–936, 1992.

[2] M. Hartmann, R. E. Miller, J. P. Toennies, and A. F. Vilesov. Rotationally Resolved Spectroscopy of SF_6 in Liquid Helium Clusters: A Molecular Probe of Cluster Temperature. *Physical Review Letters*, 75(8):1566–1569, August 1995.

[3] J. P. Toennies and A. F. Vilesov. Spectroscopy of Atoms and Molecules in Liquid Helium. *Annual Review of Physical Chemistry*, 49:1–41, October 1998.

[4] J. P. Toennies and Andrey F. Vilesov. Superfluid Helium Droplets: A Uniquely Cold Nanomatrix for Molecules and Molecular Complexes. *Angew. Chem. Int. Ed.*, 43:2622–2648, 2004.

[5] Frank Stienkemeier and Kevin K. Lehmann. Spectroscopy and dynamics in helium nanodroplets. *Journal of Physics B*, 39(8):R127–R166, 2006.

[6] Jochen Kuepper and Jeremy M. Merritt. Spectroscopy of free radicals and radical containing entrance-channel complexes in superfluid helium nanodroplets. *International Reviews in Physical Chemistry*, 26(2):249–287, 2007.

[7] Josef Tiggesbäumker and Frank Stienkemeier. Formation and properties of metal clusters isolated in helium droplets. *Physical chemistry chemical physics*, 9(34):4748–70, 2007.

[8] A. Slenczka and J. Peter Toennies. *Low Temperatures and Cold Molecules.* World Scientific, 2008.

[9] Carlo Callegari and Wolfgang E. Ernst. Helium droplets as nanocryostats for molecular spectroscopy - from the vacuum ultraviolet to the microwave regime. *Handbook of High-Resolution Spectroscopy*, 3:1551–1594, 2011.

[10] M. Mudrich and F. Stienkemeier. Photoionisaton of pure and doped helium nanodroplets. *International Reviews in Physical Chemistry*, 33(3):301–339, 2014.

[11] D. M. Brink and S. Stringari. Density of states and evaporation rate of helium clusters. *Zeitschrift für Physik D Atoms, Molecules and Clusters*, 15(3):257–263, September 1990.

[12] Marius Lewerenz. Structure and energetics of small helium clusters: Quantum simulations using a recent perturbational pair potential. *Journal of Chemical Physics*, 106:4596–4630, 1997.

[13] B. Dick and A. Slenczka. Inhomogeneous Line Shape Theory of Electronic Transitions for Molecules Embedded in Superfluid Helium Droplets. *The Journal of Chemical Physics*, 115(22):10206–10213, December 2001.

[14] Yongkyung Kwon and K. Birgitta Whaley. Localization of helium at an aromatic molecule in superfluid helium clusters. *J. Chem. Phys.*, 114(7):3163–3169, February 2001.

[15] H. D. Whitley, P. Huang, Y. Kwon, and K. B. Whaley. Multiple solvation configurations around phthalocyanine in helium droplets. *The Journal of Chemical Physics*, 123(5):054307/1–054307/8, August 2005.

[16] Heather D. Whitley, Jonathan L. DuBois, and K. Birgitta Whaley. Theoretical Analysis of the Anomalous Spectral Splitting of Tetracene in ^{4}He Droplets. *J. Phys. Chem. A*, 115:7220–7233, 2011.

[17] M. Hartmann, A. Lindinger, J. P. Toennies, and A. F. Vilesov. Laser-induced fluorescence spectroscopy of van der Waals complexes of tetracene-Ar_N ($N \leq 5$) and pentacene-Ar within ultracold liquid He droplets. *Chemical Physics*, 239(1-3):139–149, December 1998.

[18] S. Gerstenkorn and P. Luc. *Atlas du Spectre d'Absorption de la Molécule d'Iode 14800-20000 cm^{-1}*. C.N.R.S. Paris, Fr., 1978.

[19] J. D. Simmons and J. T. Hougen. Atlas of the I_2 Spectrum from 19 000 to 18 000 cm^{-1}. *JOURNAL OF RESEARCH of the National Bureau of Standards-A. Physics and Chemistry*, 81A(1):25–80, 1977.

[20] Hajime Kato, Shunji Kasahara, Masatoshi Misono, and Masaaki Baba. *DOPPLER-FREE HIGH RESOLUTION SPECTRAL ATLAS OF IODINE MOLECULE 15.000 TO 19.000 cm^{-1}*. Ohio State University, 2000.

[21] Alvaro Valdes, Rita Prosmiti, Pablo Villarreal, Gerardo Delgado-Barrio, and Hans-Joachim Werner. Ab initio potential energy surface and spectrum of the B(3Π) state of the HeI_2 complex. *J. Cem. Phys.*, 126(20):204301, 2007.

[22] S. Enss, C. und Hunklinger. *Tieftemperaturphysik*. Springer-Verlag Berlin Heidelberg New York, 2000.

[23] E. F. Burton. Viscosity of Helium I and Helium II. *Nature*, 135:265, 1935.

[24] J. O. Wilhelm, A. D. Misener, and A. R. Clark. Viscosity of Liquid Helium. *Proc. Roy. Soc. A*, 151:342–7, 1935.

[25] P. Kapitza. Viscosity of Liquid Helium below the λ-Point. *Nature*, 141(74), 1938.

[26] A.D. Allen, J.F.and Misener. Flow of Liquid Helium II. *Nature*, 141(75), 1938.

[27] W.H. Keesom and A.P. Keesom. New Measurements on the Specific Heat of Liquid Helium. *Physica*, 2:557 – 572, 1935.

[28] J. F. Allen and H. Jones. New Phenomena Connected with Heat Flow in Helium II. *Nature*, 141:243, 1938.

[29] Kamerlingh Onnes. On the Lowest Temperature Yet Obtained. *Comm. Phys. Lab. Univ. Leiden*, (159), 1922.

[30] J.G. Daunt and K. Mendelssohn. Transfer of Helium II on Glass. *Nature*, 141:911, 1938.

[31] B.V. Rollin and F. Simon. On the "Film" Phenomenon of Liquid Helium II. *Physica*, 6(2):219 – 230, 1939.

[32] Tilley D.R. und Tilley J. *Superfluidity and Superconductivity.* Institute of Physics, Bristol, 1990.

[33] James F. Annett. *Supraleitung, Suprafluidität und Kondensate.* Oldenbourg Wissenschaftsverlag GmbH, 2011.

[34] F. London. The λ-Phenomenon of Liquid Helium and the Bose-Einstein Degeneracy. *Nature*, 141(643):643–644, 1938.

[35] R. E. Grisenti, W. Schöllkopf, J. P. Toennies, G. C. Hegerfeldt, T. Köhler, and M. Stoll. Determination of the Bond Length and Binding Energy of the Helium Dimer by Diffraction from a Transmission Grating. *Phys. Rev. Lett.*, 88:2284–2287, 2000.

[36] Laszlo Tisza. Transport Phenomena in Helium II. *Nature*, 141:913, 1938.

[37] Laszlo Tisza. The Theory of Liquid Helium. *Phys. Rev.*, 72:838, 1947.

[38] H. Buchenau, E. L. Knuth, J. Northby, J. P. Toennies, and C. Winkler. Mass spectra and time-of-flight distributions of helium cluster beams. *J. Chem. Phys.*, 92(11):6875–6889, June 1990.

[39] D. R. Allum, P. V. E. McClintock, and A. Phillips. The Breakdown of Superfluidity in Liquid ^{4}He: An Experimental Test of Landau's Theory. *Phil. Trans. R. Soc. Lond. A*, 284(1320):179–224, 1977.

[40] Roger Campargue. *Atomic and Molecular Beams.* Springer, Berlin, 2001. ISBN 3-540-67378-4.

[41] Walther Gerlach and Otto Stern. Das magnetische Moment des Silberatoms. *Zeitschrift für Physik*, 9:353–5, 1922.

[42] Peter W. Atkins. *Physikalische Chemie.* Wiley-VCH, 2001.

[43] Ingo Meusel. *Aufbau einer Molekularstrahlapparatur für oberflächenkinetische Untersuchungen.* PhD thesis, Technische Universität Berlin, 2002.

[44] Andreas M. Wenge, Andreas Schmaunz, Uwe Kensy, and Bernhard Dick. Photodissociation dynamics of *tert*-butylnitrite following excitation to the S_1 and S_2 states. A study by velocity-map ion-imaging and 3D-REMPI spectroscopy. *Physical Chemistry Chemical Physics*, 14(19):7076–7089, 2012.

[45] Lei Song, Gerrit C. Groenenboom, Ad van der Avoird, Chandan Kumar Bishwakarma, Gautam Sarma, David H. Parker, and Arthur G. Suits. Inelastic Scattering of CO with He: Polarization Dependent Differential State-to-state Cross Sections. *Jornal of Physical Chemistry A*, 119:5925, 2015.

[46] Zoran Bjelobrk, Carine Manca Tanner, and Martin Quack. Investigation of the 2 + 2v3 Subband in the Overtone Icosad of $^{13}CH_4$ by Pulsed Supersonic Jet and Diode Laser Cavity Ring-Down Spectroscopy: Partial Rovibrational Analysis and Nuclear Spin Symmetry Conservation. *Zeitschrift für Physikalische Chemie*, 229(10-12):1575–1607, 2015.

[47] B. A. Joyce. Molecular beam epitaxy. *Rep. Prog. Phys.*, 48:1637–1697, 1985.

[48] Michael R. Melloch. Review of the application of molecular beam epitaxy for high efficiency solar cell research. *Solar Cells*, 30(1-4):313–21, 1991.

[49] Siegfried Mantl and Helge L. Bay. New method for epitaxial heterostructure layer growth. *Applied Physics Letters*, 61:267–269, 1992.

[50] Eric Whittle, David A. Dows, and George C. Pimentel. Matrix Isolation Method for the Experimental Study of Unstable Species. *The Journal of Chemical Physics*, 22(11):1943–1943, 1954.

[51] H. Schnöckel and S. Schunck. Matrixisolation: Erzeugung und Nachweis reaktiver Moleküle. *Chemie in unserer Zeit*, 21:73–81, June 1987.

[52] Thomas Bally. *Reactive Intermediate Chemistry.* John Wiley & Sons, Inc., 2004.

[53] Bernhard Dick. Line-narrowing spectroscopy in amorphous solids through polarization detection of spectral holes. I. Principles. *Chemical Physics*, 136:413–428, 1989.

[54] Bernhard Dick. Line-narrowing spectroscopy in amorphous solids through polarization detection of spectral holes. II. Application to tetraphenylporphin in PMMA. *Chemical Physics*, 136:429–442, 1989.

[55] M. Lewerenz, B. Schilling, and J. P. Toennies. Successive capture and coagulation of atoms and molecules to small clusters in large liquid helium clusters. *J. Chem. Phys.*, 102(20):8191–8207, May 1995.

[56] E. Lugovoj, J. P. Toennies, and A. Vilesov. Manipulating and enhancing chemical reactions in helium droplets. *The Journal of Chemical Physics*, 112:8217, 2000.

[57] Slava Grebenev, Matthias Hartmann, Martina Havenith, Boris Sartakov, J. Peter Toennies, and Andrei F. Vilesov. The rotational spectrum of single OCS molecules in liquid ^{4}He droplets. *J. Chem. Phys.*, 112(10):4485–4495, March 2000.

[58] Jian Tang, Yunjie Xu, A. R. W. McKellar, and Wolfgang Jaeger. Quantum Solvation of Carbonyl Sulfide with Helium Atoms. *Science*, 297:2030, 2002.

[59] J. Harms, M. Hartmann, J. P. Toennies, and A. F. Vilesov. Rotational Structure of the IR Spectra of Single SF_6 Molecules in Liquid ^{4}He and ^{3}He Droplets. *Journal of Molecular Spectroscopy*, 185(1):204–206, September 1997.

[60] Grebenev, Slava and Toennies, J. Peter and Vilesov, Andrei F. Superfluidity Within a Small Helium-4 Cluster: The Microscopic Andronikashvili Experiment. *Science*, 279(5359):2083–2086, 1998.

[61] Philippe Sindzingre, Michael L. Klein, and David M. Ceperley. Path-integral Monte Carlo study of low-temperature Helium-4 clusters. *Physical Review Letters*, 63:1601, 1989.

[62] M. Hartmann, F. Mielke, J. P. Toennies, A. F. Vilesov, and G. Benedek. Direct Spectroscopic Observation of Elementary Excitations in Superfluid He Droplets. *Phys. Rev. Lett.*, 76(24):4560–4563, June 1996.

[63] R. A. Cowley and D. B. Woods. Inelastic Scattering of Thermal Neutrons from Liquid Helium. *Canadian Journal of Physics*, 49(2):177–200, 1977.

[64] R.J. Donnelly, J.A. Donnelly, and R.N. Hills. Specific Heat and Dispersion Curve for Helium II. *Journal of Low Temperature Physics*, 44(5-6):471–489, 1981.

[65] Bernhard Schilling. *Molekularstrahlexperimente mit Helium-Clustern.* Dissertation, Max-Planck-Institut für Strömungsforschung, Göttingen, September 1993.

[66] J. Harms, J. P. Toennies, and E. L. Knuth. Droplets formed in helium free-jet expansions from states near the critical point. *J. Chem. Phys.*, 106(8):3348–3357, February 1997.

[67] Jan Harms, J. Peter Toennies, and Franco Dalfovo. Density of superfluid helium droplets. *Phys. Rev. B*, 58(6):3341–3350, August 1998.

[68] M. Lewerenz, B. Schilling, and J. P. Toennies. A new scattering deflection method for determining and selecting the sizes of large liquid clusters of ^{4}He. *Chemical Physics Letters*, 206(1-4):381–387, April 1993.

[69] T. Jiang and J. A. Northby. Fragmentation clusters formed in supercritical expansions of ^{4}He. *Physical Review Letters*, 68(17):2620–2623, April 1992.

[70] E. L. Knuth and U. Henne. Average size and size distribution of large droplets produced in a free-jet expansion of a liquid. *J. Chem. Phys.*, 110(5):2664–2668, February 1999.

[71] M. Fárník, U. Henne, B. Samelin, and J. P. Toennies. Comparison between positive and negative charging of helium droplets. *Zeitschrift für Physik*, 40:93–98, 1997.

[72] O. Kornilov and J.P. Toennies. The determination of the mean sizes of large He droplets by electron impact induced attenuation. *International Journal of Mass Spectrometry*, 280:209, 2009.

[73] Luis F. Gomez, Evgeny Loginov, Russell Sliter, and Andrey F. Vilesov. Sizes of large He droplets. *The Journal of Chemical Physics*, 135(15):154201/1–154201/9, 2011.

[74] Grisenti, Robert E. and Toennies, J. Peter. Cryogenic Microjet Source for Orthotropic Beams of Ultralarge Superfluid Helium Droplets. *Phys. Rev. Lett.*, 90:234501, 2003.

[75] Manuel Barranco, Rafael Guardiola, Susana Hernández, Ricardo Mayol, Jesús Navarro, and Martí Pi. Helium Nanodroplets: An Overview. *Journal of Low Temperature Physics*, 142(1-2):1–81, 2006.

[76] Dominik Pentlehner, Ricarda Riechers, Bernhard Dick, Alkwin Slenczka, Uzi Even, Nachum Lavie, Raviv Brown, and Kfir Luria. Rapidly Pulsed Helium Droplet Source. *Rev. Sci. Instrum.*, 80:043302, 2009.

[77] Dominik Pentlehner. *Perturbations of Electronic Transitions of Organic Molecules in Helium Droplets Generated with a New Pulsed Droplet Source.* PhD thesis, Universität Regensburg, 2010.

[78] S. Stringari and J. Treiner. Systematics of liquid helium clusters. *J. Chem. Phys.*, 87(8):5021–5027, October 1987.

[79] S. A. Chin and E. Krotschek. Systematics of Pure and Doped ^{4}He Clusters. *Physical Review B*, 52(14):10405–10428, October 1995.

[80] T. E. Gough, M. Mengel, P. A. Rowntree, and G. Scoles. Infrared spectroscopy at the surface of clusters: SF_6 on Ar. *The Journal of Chemical Physics*, 83:4958, 1985.

[81] A. Scheidemann. *Das Einbetten von Fremdatomen in Helium-Cluster.* PhD thesis, Max-Planck-Institut für Strömungsforschung, 1989.

[82] Evgeniy Loginov, Andreas Braun, and Marcel Drabbels. A new sensitive detection scheme for helium nanodroplet isolation spectroscopy: application to benzene. *Physical Chemistry Chemical Physics*, 10:6107–6114, 2008.

[83] F. Stienkemeier and A. F. Vilesov. Electronic spectroscopy in He droplets. *The Journal of Chemical Physics*, 115(22):10119–10137, December 2001.

[84] Joshua Jortner. Cluster Size Effects. *Z. Phys. D - Atoms, Molecules and Clusters*, 24(3):247–275, April 1992.

[85] Matthias Hartmann. *Hochauflösende Spektroskopie von Molekülen in* ^{4}*Helium- und* ^{3}*Helium-Clustern.* PhD thesis, Max-Planck-Institut für Strömungsforschung Göttingen, June 1997.

[86] Rudolf Lehnig. *Anregungs- und Emissionsspektroskopie von organischen Molekülen in ^{4}He-Tröpfchen.* PhD thesis, Universität Regensburg, June 2004.

[87] J. Peter Toennies, Andrej F. Vilesov, and K. Birgitta Whaley. Superfluid helium droplets: An ultracold nanolaboratory. *Physics Today*, 54(2):31–37, 2001.

[88] Matthias Hartmann, Albrecht Lindinger, J. Peter Toennies, and Andrej F. Vilesov. The phonon wings in the (S_1←S_0) spectra of tetracene, pentacene, porphin and phthalocyanine in liquid helium droplets. *Physical Chemistry Chemical Physics*, 4:4839–4844, 2002.

[89] A. Lindinger, E. Lugovoj, J. P. Toennies, and A. F. Vilesov. Splitting of the Zero Phonon Lines of Indole, 3-Methyl Indole, Tryptamine and N-Acetyl Tryptophan Amide in Helium Droplets. *Zeitschrift für Physikalische Chemie*, 215(3):401–416, March 2001.

[90] Matthias Hartmann, Albrecht Lindinger, J. Peter Toennies, and Andrej F. Vilesov. Hole-Burning Studies of the Splitting in the Ground and Excited Vibronic States of Tetracene in Helium Droplets. *The Journal of Physical Chemistry A*, 105(26):6369–6377, July 2001.

[91] Albrecht Lindinger, J. Peter Toennies, and Andrej F. Vilesov. Pump-probe study of the reconstruction of helium surrounding a tetracene molecule inside a helium droplet. *Physical Chemistry Chemical Physics*, 3:2581–2587, 2001.

[92] Nikolas Poertner, J. Peter Toennies, Andrey F. Vilesov, and Frank Stienkemeier. Anomalous fine structures of the 0_0^0 band of tetracene in large He droplets and their dependence on droplet size. *Molecular Physics*, 110:1767–1780, 2012.

[93] Rudolf Lehnig, Mikhail Slipchenko, Susumu Kuma, Takamasa Momose, Boris Sartakov, and Andrei Vilesov. Fine Structure of the (S_1← S_0) Band Origins

of Phthalocyanine Molecules in Helium Droplets. *The Journal of Chemical Physics*, 121(19):9396–9405, November 2004.

[94] R. Riechers, D. Pentlehner, and A. Slenczka. Microsolvation in Superfluid Helium Droplets Studied by the Electronic Spectra of Six Porphyrin Derivatives and One Chlorine Compound. *The Journal of Chemical Physics*, 138(24):244303, 2013.

[95] A. Slenczka, B. Dick, M. Hartmann, and J. P. Toennies. Inhomogeneous broadening of the zero phonon line of phthalocyanine in superfluid helium droplets. *The Journal of Chemical Physics*, 115(22):10199–10205, December 2001.

[96] Susumu Kuma, Hiroko Nakahara, Masaaki Tsubouchi, Akira Takahashi, Majd Mustafa, Goeun Sim, Takamasa Momose, and Andrey F. Vilesov. Laser Induced Fluorescence Spectroscopy of Tetracene with Large Ar, Ne, and H_2 Clusters in Superfluid He Nanodroplets. *Journal of Physical Chemistry A*, 115:7392–7399, 2011.

[97] S. Grebenev, M. Hartmann, A. Lindinger, N. Pörtner, B. Sartakov, J. P. Toennies, and A. F. Vilesov. Spectroscopy of molecules in helium droplets. *Physica B: Condensed Matter*, 280(1-4):65–72, May 2000.

[98] D. Pentlehner, Ch. Greil, B. Dick, and A. Slenczka. Line broadening in electronic spectra of anthracene derivatives inside superfluid helium nanodroplets. *The Journal of Chemical Physics*, 133(11):114505/1–114505/9, 2010.

[99] D. Pentlehner, R. Riechers, A. Vdovin, G. M. Pötzl, and A. Slenczka. Electronic Spectroscopy of Molecules in Superfluid Helium Nanodroplets: An Excellent Sensor for Intramolecular Charge Redistribution. *The Journal of Physical Chemistry A*, 115(25):7034–7043, 2011.

[100] T. Premke, E.-M. Wirths, D. Pentlehner, R. Riechers, R. Lehnig, A. Vdovin, and A. Slenczka. Microsolvation of molecules in superfluid helium nanodroplets

revealed by means of electronic spectroscopy. *Frontiers in Chemistry*, 2:1–12, 2014.

[101] D. Pentlehner and A. Slenczka. Helium induced fine structure in the electronic spectra of anthracene derivatives doped into superfluid helium nanodroplets. *The Journal of chemical physics*, 142(1):014311, 2015.

[102] M. Xu and Z. Bačić. Wave Function Delocalization and Large-Amplitude Vibrations of Helium on Corrugated Aromatic Microsurfaces: Tetracene·He and Pentacene·He van der Waals Complexes. *The Journal of Physical Chemistry A*, 111(31):7653–7663, August 2007.

[103] P. Huang, H. D. Whitley, and K. B. Whaley. Structure and Energetics of Helium Adsorption on Nanosurfaces. *Journal of Low Temperature Physics*, 134(1-2):263–268, January 2004.

[104] R. Lehnig and A. Slenczka. Spectroscopic investigation of the solvation of organic molecules in superfluid helium droplets. *The Journal of Chemical Physics*, 122(24):244317/1–244317/9, June 2005.

[105] R. Lehnig and A. Slenczka. Emission spectra of free base phthalocyanine in superfluid helium droplets. *J. Chem. Phys.*, 118(18):8256–8260, 2003.

[106] R. Lehnig and A. Slenczka. Quantum solvation of phthalocyanine in superfluid helium droplets. *The Journal of Chemical Physics*, 120(11):5064–5066, March 2004.

[107] R. Lehnig and A. Slenczka. Microsolvation of Phthalocyanines in Superfluid Helium Droplets. *European Journal of Chemical Physics and Physical Chemistry*, 5(7):1014–1019, July 2004.

[108] R. Fröchtenicht, J. P. Toennies, and A. Vilesov. High-resolution infrared spectroscopy of SF_6 embedded in He clusters. *Chemical Physics Letters*, 229(1-2):1–7, October 1994.

[109] *Manual Bolometer - Infrared Laboratories.*

[110] Physikalisches Praktikum für Fortgeschrittene TU Darmstadt - Thermometrie bei tiefen Temperaturen.

[111] The National Institute of Standards and Technology. NIST Atomic Spectra Database. http://physics.nist.gov/PhysRefData/ASD/lines_form.html, 20.12.2015.

[112] Matthias Hartmann, Roger E. Miller, J. Peter Toennies, and Andrej F. Vilesov. High-Resolution Molecular Spectroscopy of van der Waals Clusters in Liquid Helium Droplets. *Science*, 272(5268):1631–1634, 1996.

[113] K. Nauta and R. E. Miller. Nonequilibrium self-assembly of long chains of polar molecules in superfluid helium. *Science*, 283(5409):1895–1897, March 1999.

[114] K. Nauta and R. E. Miller. The rotational dynamics of N_2-HF and OC-HF in helium nanodroplets. *Journal of Chemical Physics*, 117:4846–4852, 2002.

[115] G. E. Douberly, K. Nauta, and R. E. Miller. The infrared spectrum of acetylene-HF in helium nanodroplets. *Chemical Physics Letters*, 377:384–390, 2003.

[116] Gary E. Douberly and Roger E. Miller. Vibrational dynamics of the linear and bent isomers of HF-N_2O trapped in 0.4 K helium nanodroplets. *Chemical Physics*, 361:118–124, 2009.

[117] G. E. Douberly and R. E. Miller. The isomers of HF-HCN formed in helium nanodroplets: Infrared spectroscopy and ab initio calculations. *Journal of Chemical Physics*, 122:024306/1–024306/8, 2005.

[118] Ricarda Riechers. *Optische Spektroskopie von Molekülen in superflüssigen Heliumtropfen. Untersuchung von Schwingungsmoden im elektronischen*

Grundzustand und in elektronisch angeregten Zuständen. Diplomarbeit, Universität Regensburg, 2007.

[119] Ricarda Riechers. *High-resolution spectroscopy in superfluid helium droplets. Investigation of vibrational fine structures in electronic spectra of phthalocyanine and porphyrin derivatives.* PhD thesis, Universität Regensburg, 2011.

[120] P.G. Seybold and M. Gouterman. Porphyrin XIII: Fluorescence Spectra and Quantum Yields. *J. Mol. Spectrosc.*, 31:1, 1969.

[121] K. G. Saur. Restaurator. *International Journal for the Preservation of Library and Archival Material*, 26:134–150, 2005.

[122] Imran Murtaza and Khasan S. Karimov. Nickel Phthalocyanine-Based Sandwich-Type Photocapacitive Illumination Sensors for Environmental Monitoring. *Arabian Journal for Science and Engineering*, 37:233–237, 2012.

[123] Pavlo I. Stakhira, Georgij L. Pakhomov, Vlad V. Cherpak, Dmitro Volynyuk, Grzegorz Luka, Marek Godlewski, Elżbieta Guziewicz, and Zenon Yu Hotra. Photovoltaic cells based on nickel phthalocyanine and zinc oxide formed by atomic layer deposition. *Central European Journal of Physics*, 8:798–803, 2010.

[124] A. K. Shukla, C. Paliteiro, R. Manoharan, A. Hamnett, and J. B Goodenough. Efficient oxygen reduction in alkaline solution with platinum phthalocyanine on porous carbon. *Journal of Applied Electrochemistry*, 19:105–107, 1989.

[125] Ahmed Galal, Soher A. Darwish, and Rasha A. Ahmed. Hybrid organic/inorganic films of conducting polymers modified with phthalocyanines. I-Film reparation and voltammetric studies. *Journal of Solid State Electrochemistry*, 11:521–530, 2007.

[126] Lakshmana Naik Ramavathu, Kranthi Kumar Maniam, Keerthiga Gopalram, and Raghuram Chetty. Effect of pyrolysis temperature on cobalt phthalocya-

nine supported on carbon nanotubes for oxygen reduction reaction. *Journal of Applied Electrochemistry*, 42:945–951, 2012.

[127] Lei Ding, Qing Xin, Xuejun Zhou, Jinli Qiao, Hui Li, and Haijang Wang. Electrochemical behavior of nanostructured nickel phthalocyanine (NiPc/C) for oxygen reduction reaction in alkaline media. *Journal of Applied Electrochemistry*, 43:43–51, 2013.

[128] Carl A. Barker, Xianshun Zeng, Sylvia Bettington, Andrei S. Batsanov, Martin R. Bryce, and Andrew Beeby. Porphyrin, Phthalocyanine and Porphyrazine Derivatives with Multifluorenyl Substituents as Efficient Deep-Red Emitters. *Chemistry - A European Journal*, 13:6710 – 6717, 2007.

[129] Won Min Yun, Jaeyoung Jang, Sooji Nam, Chan Eon Park, Se Hyun Kim, and Dae Sung Chung. Organic Light-Emitting Diodes with Low Turn-On Voltages and Improved Stability Featuring a PTCDI-C13:CuPc Mixed Hole Injection Layer. *Science of Advanced Materials*, 6(8):1676–1680, 2014.

[130] M. Ramar, Priyanka Tyagi, C. K. Suman, and Ritu Srivastava. Enhanced carrier transport in tris(8-hydroxyquinolinate) aluminum by titanyl phthalocyanine doping. *RSC Advances*, 4:51256–51261, 2014.

[131] Shiliang Qu, Yachen Gao, Chongjun Zhao, Yuxiao Wang, Shiyou Fu, Yinglin Song, Duoyuan Wang, Jianrong Qiu, and Congshan Zhu. Optical limiting properties in phthalocyanines with different substituent groups. *Applied Physics Letters*, 78:1319–1321, 2001.

[132] Danilo Dini, Markus Barthel, and Michael Hanack. Phthalocyanines as Active Materials for Optical Limiting. *European Journal of Organic Chemistry*, 2001:3759–3769, 2001.

[133] R.W. Boyle, C.C. Leznoff, and J.E. van Lier. Biological activities of phthalocyanines - XVI. Tetrahydroxy- and tetraalkylhydroxy zinc phthalocyanines.

Effect of alkyl chain length on *in vitro* and *in vivo* photodynamic activities. *British Journal of Cancer*, 67:1177–1181, 1993.

[134] W.-S. Chan, N. Brasseur, C. La Madeleine, R. Ouellet, and J.E. van Lier. Efficacy and Mechanism of Aluminium Phthalocyanine and its Sulphonated Derivatives Mediated Photodynamic Therapy on Murine Tumours. *European Journal of Cancer*, 33(11):1855–1859, 1997.

[135] Andreas Hirth, Dr. Ulrike Michelsen, and Prof. Dr. Dieter Wöhrle. Photodynamische Tumortherapie. *Chemie in unserer Zeit*, 33:84–94, 1999.

[136] M.R. Detty, S.L. Gibson, and S.J. Wagner. Current clinical and preclinical photosensitizers for use in photodynamic therapy. *Journal of Medicinal Chemistry*, 47(16):3897–3915, 2004.

[137] Mahmut Durmuş and Vefa Ahsen. Water-soluble cationic gallium(III) and indium(III) phthalocyanines for photodynamic therapy. *Journal of Inorganic Biochemistry*, 104:297–309, 2010.

[138] Huichen Guo, Haisheng Qian, Niagara Muhammad Idris, and Yong Zhang. Singlet oxygen-induced apoptosis of cancer cells using upconversion fluorescent nanoparticles as a carrier of photosensitizer. *Nanomedicine: Nanotechnology, Biology and Medicine*, 6:486–495, 2010.

[139] Monica Monica Camerin, Michela Magaraggia, Marina Soncin, Giulio Jori, Miguel Moreno, Isabelle Chambrier, Michael J. Cook, and David A. Russell. The *in vivo* efficacy of phthalocyanine-nanoparticle conjugates for the photodynamic therapy of amelanotic melanoma. *European Journal of Cancer*, 46:1910–1918, 2010.

[140] Shawn Swavey and Matthew Tran. *Porphyrin and Phthalocyanine Photosensitizers as PDT Agents: A New Modality for the Treatment of Melanoma, Recent Advances in the Biology, Therapy and Management of Melanoma.* In-Tech, 2013.

[141] R. Lehnig, J. A. Sebree, and A. Slenczka. Structure and Dynamics of Phthalocyanine-Argon$_n$ (n = 1–4) Complexes Studied in Helium Nanodroplets. *Journal of Physical Chemistry A*, 111(31):7576–7584, May 2007.

[142] S.H. Cho, M.-h. Yoon, and S.K. Kim. Spectroscopy and energy disposal dynamics of phthalocyanine-Ar$_n$ (n=1,2) complexes generated by hyperthermal pulsed nozzle source. *Chemical Physics Letters*, 326:65, 2000.

[143] P.S.H. Fitch, C.A. Haynam, and D.H. Levy. The fluorescence excitation spectrum of free base phthalocyanine cooled in a supersonic free jet. *J. Chem. Phys.*, 73(3):1064, 1980.

[144] E. Breitmaier and G. Jung. *"Organische Chemie"*. Thieme Georg Verlag, 2005.

[145] Hiroko Yamada, Yuko Yamashita, Makoto Kikuchi, Hikaru Watanabe, Tetsuo Okujima, Hidemitsu Uno, Takuji Ogawa, Keishi Ohara, and Noboru Ono. Photochemical Synthesis of Pentacene and its Derivatives. *Chemistry - A European Journal*, 11:6212–6220, 2005.

[146] Chandrani Pramanik and Glen P. Miller. An Improved Synthesis of Pentacene: Rapid Access to a Benchmark Organic Semiconductor. *Molecules*, 17:4625–4633, 2012.

[147] Harmen de Vries and Douwe A. Wiersma. Fluorescence transient and optical free induction decay spectroscopy of pentacene in mixed crystals at 2 K. Determination of intersystem crossing and internal conversion rates. *Journal of Chemical Physics*, 70:5807, 1979.

[148] H. de Vries, P. de Bree, and D.A. Wiersma. Optical free induction and fluorescence decay of pentacene in p-terphenyl following narrow band laser excitation. *Chem. Phys. Lett.*, 52:399, 1977.

[149] T.E. Orlowski and A.H. Zewail. Radiationless relaxation and optical dephasing of molecules excited by wide- and narrow-band lasers. II. Pentacene in low-temperature mixed crystals. *J. Chem. Phys.*, 70:1390, 1979.

[150] A. Armirav, U. Even, and J. Jortner. Butterfly motion of the isolated pentacene molecule in its first-excited singlet state. *Chemical Physical Letters*, 72(1):21–4, 1980.

[151] Anne M. Griffiths and Philip A. Freedman. Out-of-plane Vibrations of Isolated Tetracene and Pentacene Molecules. *J. Chem. Soc., Faraday Trans.*, 2:391–398, 1982.

[152] E. Heinecke, D. Hartmann, R. Müller, and A. Hese. Laser spectroscopy of free pentacene molecules (I): The rotational structure of the vibrationless $S_1 \leftarrow S_0$ transition. *Journal of Chemical Physics*, 109:906, 1998.

[153] G. Hoheisel, E. Heinecke, and A. Hese. Optical-optical double resonance spectroscopy on pentacene molecules in a supersonic jet. *Chemical Physics Letters*, 373:416–421, 2003.

[154] E. Wiedemann, K. Stelzner, and G. Niederschulte. Vapor Pressures of Solid Bodies. *Verh. d. Dtsch. phys. Ges.*, 3:159–62, 1905.

[155] R.E. Honig. *Vapor Pressure Data for the Solid and Liquid Elements.* RCA Review, Volume 23, 1962.

[156] A. F. Holleman, E. Wiberg, and N. Wiberg. *Lehrbuch der Anorganischen Chemie.* Walter de Gruyter, Berlin, New York, 1995.

[157] Otto Oldenberg. Ultraviolette Resonanzspektren des Joddampfes. *Zeitschrift für Physik*, 18:1–11, 1923.

[158] M. Davies. Simple Molecular Spectra Experiments. *J. Chem. Educ.*, 28:474, 1951.

[159] R.D. Verma. Ultraviolet Resonance Spectrum of the Iodine Molecule. *Journal of Chemical Physics*, 32(3):738, 1960.

[160] Fred E. Stafford. Band Spectra and Dissociation Energies. *J. Chem. Educ.*, 39:626–629, 1962.

[161] J.Leland Hollenberg. Energy states of molecules. *J. Chem. Educ.*, 47(1):2–14, 1970.

[162] Joel Tellinghuisen. Laser-Induced Molecular Fluorescence: A physical chemistry experiment. *Journal of Chemical Education*, 58:438–41, 1981.

[163] Joel Tellinghuisen. Laser-Induced Fluorescence in Gaseous I_2 Excited with a Green Laser Pointer. *Journal of Chemical Education*, 82(2):336–341, 2007.

[164] J.C. Lehmann. Iodine, a Test Molecule in Modern Spectroscopy. *Contemp. Phys.*, 19(5):449–468, 1978.

[165] G. Herzberg. *Spectra of Diatomic Molecules*. Van Nostrand, 1970.

[166] Richard F. Barrow and Kim K. Yee. $B^3\Pi_{0_u^+}-X^1\Sigma_g^+$ System of $^{127}I_2$: Rotational Analysis and Long-range Potential in the $B^3\Pi_{0_u^+}$ State. *J. Chem. Soc. Faraday II*, 69:684, 1973.

[167] Seung Jun Lee, Myong Yong Choi, and Roger E. Miller. Vibrational spectroscopy of xanthine in superfluid helium nanodroplets. *Chemical Physics Letters*, 475:24–29, 2009.

[168] A. Slenczka. Private communication, 2015.

[169] K. Nauta and R. E. Miller. Metastable vibrationally excited HF (v=1) in helium nanodroplets. *J. Cem. Phys.*, 113:9466, 2000.

Acknowledgement

I would like to thank all people who actively supported me and my work.

A special thanks goes to my supervisor Prof. Dr. Alkwin Slenczka for his encouragement and his scientific support all the time. Thanks also for motivation, personal support and the possibility to work independently.

I would also like to thank Prof. Dr. Bernhard Dick for the opportunity to work on this project and stimulating discussions.

My thanks also to Dr. Uwe Kensy for always helping with words and deeds when technical problems occurred.

I also wish to thank my colleague Dr. Eva-M. Wirths for the great atmosphere in the lab and always being supportive.

I wish to thank PD Dr. Denis Usvyat for his help on quantum chemical considerations.

I also like to thank Philipp Meier, Dominik Zahnweh, Fabian Spitzer, Eva Brandes, Andreas Seitz and Lars Christiansen for the great work during their scientific internship in our lab.

Thanks to all current members of the institute, namely Dr. Manuel Schneider, Nicole Berner, Fabian Brandl, Uwe Faltermeier, Kathrin Magerl, Ivan Stambolic, Dr. Markus Leitl, Dr. Rafal Czerwienicz, Dr. Thomas Hofbeck, Dr. Larisa Mataranga-Popa, Alexander Schinabeck, Prof. Dr. Hartmut Yersin, Dr. Elizabeth Lupton, Dr. Gerhard Herzog, Madlene v. Sanden, Andrea Nömeier, Klaus Ziereis, Joachim Herman, Birte Höing, and Gabriele Alder, for the pleasant atmosphere and help whenever needed.

Furthermore, my thanks are given to the staff of the mechanical and electronic workshops for technical advice and their realizing my ideas as fast as possible.

I would also like to thank my whole family and friends for the support and the great time outside the lab.

Last but not least my special thanks goes to my wife for her appreciation, empathy and love, supporting me all the time.

Eidesstattliche Erklärung

Ich erkläre hiermit, dass ich die Doktorarbeit selbständig verfasst, noch nicht anderweitig für Prüfungszwecke vorgelegt, keine anderen als die angegebenen Quellen und Hilfsmittel benutzt sowie wörtliche und sinngemäße Zitate als solche gekennzeichnet habe.

Regensburg, den 21. Dezember 2015, ____________________
(Ort) (Datum) (Premke Tobias)